INSTYTUT FIZYKI JĄDROWEJ IM. HENRYKA NIEWODNICZAŃSKIEGO POLSKIEJ AKADEMII NAUK

Spectator-induced electromagnetic effects in ^{40}Ar+^{45}Sc collisions at 40A GeV/c beam momentum

DOCTORAL THESIS

Author:
Mgr. Sneha Bhosale

Promoter:
Prof. dr hab. Andrzej Rybicki

Kraków, 2023

to my parents

Acknowledgements

First and foremost, I wish to express profound gratitude to my supervisor, Prof. Andrzej Rybicki, for his unwavering support, invaluable guidance, and immense patience throughout my PhD studies. His extensive knowledge and expertise, generously shared with me, were pivotal to the successful completion of this research.

I also express gratitude to Prof. Marek Gaździcki, whose extraordinary leadership of the experiment was indeed remarkable. This research would not have been feasible without the continuous assistance and guidance from Dr Antoni Marcinek and Dr Nikolaos Davis, whose dedication and commitment to the analysis were integral to the progress of this work. I am immensely thankful to Prof. Katarzyna Grebieszkow, Dr Vitalii Ozvenchuk, Łukasz Rozpłochowski, Dr Maciej Lewicki, Dr Piotr Podlaski and Andrey Seryakov and other members of NA61/SHINE collaboration, whose collective efforts significantly contributed to the successful completion of this project. I would like to thank Prof. Marek Kowalski for his insightful suggestions and to Dr Iwona Sputowska for her assistance with the study of correlations and fluctuations, which, for clarity, is distinct from the thesis work.

I wish to convey deep gratitude to my dearest friend, Dr Arpan Das, whose wise counsel and unwavering support proved instrumental in my research. I am equally thankful to my friends for their support and encouragement throughout this journey.

I am eternally indebted to my parents and brothers for their limitless patience, unwavering support, and financial assistance, without which this research would not have materialised.

Last but not least, my heartfelt thanks go to Dominik for his constant motivation, love and support, which have been pivotal in maintaining my focus and sanity during the rigorous process of writing this thesis.

The project was partially supported by the National Science Centre, Poland, under grant no. 2014/14/E/ST2/00018.

"There are no facts, only interpretations."
-Nietzsche

Abstract

Spectator-induced electromagnetic effects in ^{40}Ar+^{45}Sc collisions at 40A GeV/c beam momentum

The SPS Heavy Ion and Neutrino Experiment (NA61/SHINE) at CERN is a scientific endeavour aimed at scrutinizing the characteristics of hadron production in hadron-hadron, hadron-nucleus, and nucleus-nucleus collisions.

In this doctoral dissertation, a comprehensive experimental study of spectator-induced electromagnetic (EM) effects in Ar+Sc collisions at 40A GeV/c ($\sqrt{s_{NN}}$ = 8.76 GeV) is presented. The study is carried out by analyzing the modification of charged pion (π^+/π^-) ratios as a function of the Feynman variable x_F, transverse momentum p_T, and collision centrality. The experimental analysis presented herein demonstrates the presence of spectator-induced EM effects in small-scale nuclear collision systems at SPS energies. With increasing peripherality of the collision, the EM distortion of π^+/π^- ratios increases as a function of increasing spectator charge.

The study presented in this dissertation enhances our understanding of the interplay between EM and isospin effects in the collision. Also, it includes a comparative analysis between current Ar+Sc results and earlier results from the NA49 experiment's Pb+Pb data for peripheral collisions at 158A GeV/c ($\sqrt{s_{NN}}$ = 17.3 GeV) obtained at the SPS. This analysis is supplemented by a discussion of the qualitative similarities and quantitative differences in EM effects in Ar+Sc and Pb+Pb collisions. Finally, acknowledging that these effects can shed new light on the space-time evolution of particle production, the study incorporates a dedicated Monte Carlo model simulation to explore this evolution.

Streszczenie

Efekty elektromagnetyczne wywołane przez układy spektatorów w zderzeniach ^{40}Ar+^{45}Sc przy pędzie wiązki 40A GeV/c

Eksperyment NA61/SHINE (SPS Heavy Ion and Neutrino Experiment) w CERN to przedsięwzięcie naukowe, mające na celu zbadanie własności zjawisk produkcji hadronów w zderzeniach hadron-hadron, hadron-jądro i jądro-jądro.

Niniejsza rozprawa doktorska przedstawia studium doświadczalne efektów elektromagnetycznych wywołanych przez "układy spektatorów" w zderzeniach Ar+Sc przy pędzie wiązki równym 40A GeV/c ($\sqrt{s_{NN}}$ = 8.76 GeV). Studium to polega na zbadaniu modyfikacji stosunków emisji naładowanych pionów (π^+/π^-) w funkcji zmiennej Feynmana x_F, pędu poprzecznego p_T i centralności zderzenia. Przedstawiona analiza eksperymentalna udawadnia obecność spowodowanych przez układy spektatorów efektów elektromagnetycznych w systemach zderzających się niewielkich jąder przy energiach akceleratora SPS. Z rosnącą peryferyjnością zderzenia, elektromagnetyczna dystorsja stosunków π^+/π^- zwiększa się, wraz z rosnącym całkowitym ładunkiem układu spektatorów.

Zaprezentowana w rozprawie analiza powiększa naszą wiedzę o nakładaniu się efektów elektromagnetycznych i izospinowych w zderzeniu. Zawiera ona także studium porównawcze pomiędzy zderzeniami Ar+Sc oraz danymi z peryferyjnych zderzeń Pb+Pb przy pędzie wiązki równym 158A GeV/c ($\sqrt{s_{NN}}$ = 17.3 GeV), uzyskanymi przez eksperyment NA49 na akceleratorze SPS. Studium to uzupełnia dyskusja jakościowych podobieństw oraz ilościowych różnic w efektach elektromagnetycznych w zderzeniach Ar+Sc i Pb+Pb. Wreszcie, uwzględniając fakt że wspomniane efekty mogą rzucić nowe światło na czasoprzestrzenną ewolucję procesu produkcji cząstek, rozprawa zawiera również obliczenia modelowe wykonane za pomocą symulacji Monte Carlo i mające na celu analizę tej ewolucji.

Contents

List of Figures

List of Tables

Chapter 1

Introduction

More than a century ago, in 1911, Ernest Rutherford discovered that the atom has a central core called a nucleus. In an experiment, he bombarded a gold plate with alpha rays, and from the resulting observations, he concluded that the scattering could only be explained by assuming that 99% of the mass lies within the atom's core. Since then, physicists have been studying the properties of the atomic nucleus and trying to understand the nature of the *strong force* responsible for its existence. Later, it was discovered that the atomic nucleus contains protons and neutrons. In the following decades, discoveries and breakthroughs led to a new branch of physics.

According to the big bang model of cosmology, the presently observed universe began from a hot and dense state of matter. This hot, dense matter then expanded and cooled down while expanding. After a given time of this initial expansion, physicists believe that the universe cooled sufficiently to allow for the formation of subatomic particles and later atoms.

To investigate the earliest stages of the universe and trace its evolution back to its origin at high temperature and density, it is necessary to recreate the conditions of the early universe in laboratory experiments. This has been achieved through the use of accelerators, which allow for high-energy collisions of atomic nuclei, and thereby enable researchers to "simulate" the conditions of the early universe.

The present chapter describes the motivation for such studies in the context of ion-ion collisions at (ultra-)relativistic energies. In addition, the strategy and main objectives of the present analysis are discussed.

1.1 Standard Model

The nucleus consists of protons and neutrons, collectively called nucleons. Nucleons belong to the general family of *hadrons*. The hadrons are composite particles and are made up of even smaller elementary particles, called quarks. The Standard Model (SM) [1] describes the properties of elementary particles and the interactions between them. We differentiate four interactions: electromagnetic, strong, weak and gravity. The first three forces are included in SM. Gravity, described by General Relativity, is not included in the SM. The elementary particles in the SM are organized into groups as shown in Fig. 1.1. The figure includes fermions: quarks and leptons which are fundamental constituents of matter, and bosons (force carriers). The quarks occur in six flavors: up (u), down (d), charm (c), strange (s), top (t), and bottom (b). Correspondingly, there are six leptons: electron (e), electron neutrino (ν_e), muon (μ), muon neutrino (μ_ν), tau (τ), and tau neutrino (ν_τ). The gauge bosons mediate interactions between the particles. Gluons are carriers of the strong force. The weak force is mediated by W^+, W^-, and Z^0 bosons. The electromagnetic force is carried by photons (γ). There are also antiparticles corresponding to particles listed in Fig. 1.1 (anti-quarks and anti-leptons). The Higgs boson, a particle connected to the mechanism that imparts mass

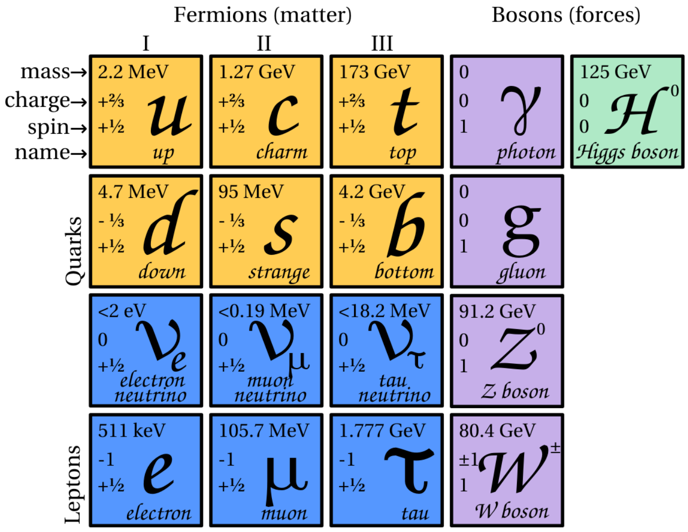

FIGURE 1.1: Standard Model of elementary particles. Picture taken from the Ref. [2].

to other particles, was postulated by the SM. Its existence was experimentally confirmed in 2012 at the Large Hadron Collider (LHC) through two distinctive experiments: the Compact Muon Solenoid (CMS) [3] and A Toroidal LHC ApparatuS (ATLAS) [4].

1.2 Quantum Chromodynamics

Quantum chromodynamics (QCD) is the theory of strong interactions. It describes the strong force between quarks and gluons. Quarks interact with each other by exchanging gluons. Gluons carry the charge of the strong interaction, called color. They carry one color (red, green and blue) and one anticolor (anti-red, anti-green and anti-blue) charge simultaneously, whereas quarks carry one of the three color charges (and anti-quarks carry anti-colors). It should be mentioned that a gluon can couple to other gluons. The strong force between quarks makes them inseparable at scales larger than the size of nucleons and keeps them confined within hadrons. Consequently, quarks and gluons cannot exist as free particles; this is known as QCD confinement.

In order to understand how hadrons are bound together and what is the nature of their interactions, we collide hadrons or atomic nuclei. There are two ways to carry out such collisions: $collider$ experiments, where two beams are forced to collide and $fixed - target$ experiments, where a beam collides with a stationary target in the laboratory frame and a large number of secondary particles are produced in the forward direction.

1.3 Nucleus-nucleus collisions

Exploring collisions between atomic nuclei has proven indispensable for enhancing our comprehension of the underlying principles that determine the properties of matter. These high-energy reactions offer valuable information about the intricate aspects of QCD, the powerful forces within the nucleus, and the attributes of quark-gluon plasma.

A non-central nucleus-nucleus collision is shown schematically in Fig. 1.2. The distance between the centers of colliding nuclei in the transverse direction is known as impact parameter b. The shape of the moving nuclei is subject to Lorentz contraction, as apparent in the figure. Nucleons that do

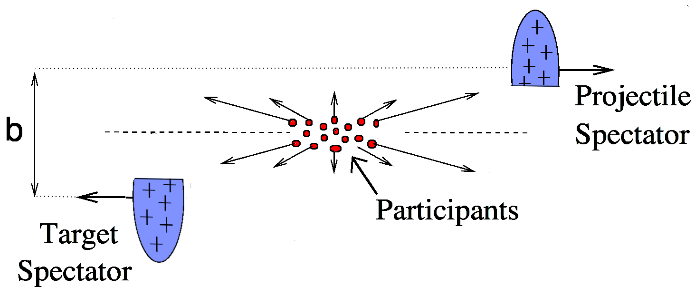

FIGURE 1.2: Schematic view of a nucleus-nucleus collision. The impact parameter (b) is shown. The red coloured circles represent participants while the blue areas correspond to spectator systems.

take part in the collision are called participants [1]. Nucleons which do not take part in the collision are called spectators.

In the fixed-target scenario, the beam nuclei are frequently referred to as projectiles. The number of spectators associated with the projectile is particularly important. It can be estimated with the measurements from a hadron calorimeter. Often this is used to estimate the collision centrality, as is also the case in this thesis.

1.4 Evolution of the collision

To understand the evolution of the collision, let us consider a head-on collision between two nuclei A and B in the center-of-mass (c.m.s.) frame [2]. In the discussion below τ will be the proper time corresponding to a given $c.m.$ system moving at a given rapidity and τ_0 is the time needed to achieve the equilibrium phase.

In the initial stage when two nuclei collide ($\tau \sim 0$ fm$/c$) (1 fm = 10^{-15}m), one of two scenarios can take place as shown in Fig. 1.3. At high energy when two Lorentz contracted atomic nuclei collide, this allows the nucleons to overlap, creating a high energy density region. At this point, the quarks and gluons interact with each other. The momentum of the colliding nuclei dictates the further evolution of the system. At low beam momentum,

---

[1] In this thesis we will also use the term "wounded nucleons" following the nomenclature introduced by the Wounded Nucleon Model (WNM) [5]. A wounded nucleon is a nucleon that underwent at least one inelastic collision.

[2] The description made in this section is largly based on Refs. [2, 6, 7].

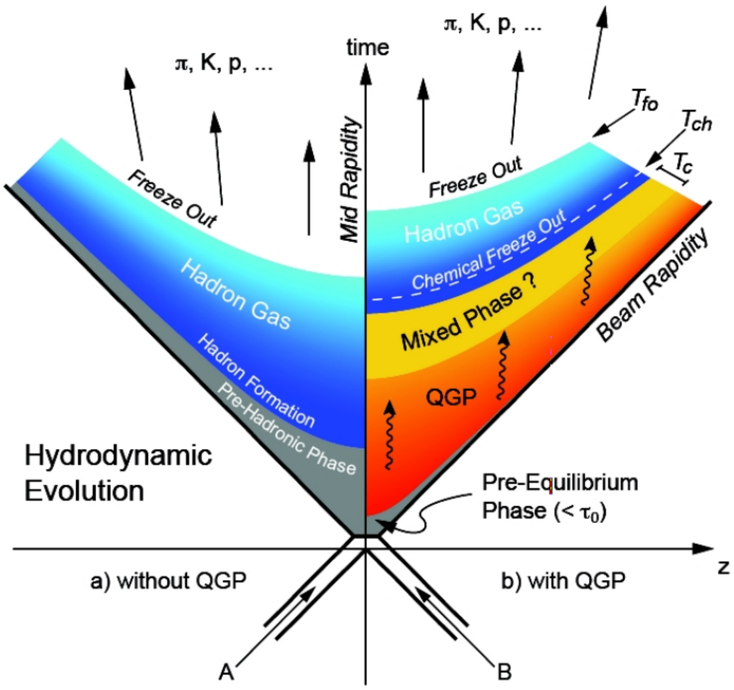

FIGURE 1.3: Two different scenarios of collision of two relativistic nuclei 'A' and 'B'. The direct formation of hadrons in a series of strong interactions is shown on the left side. The creation of the quark-gluon plasma phase, subsequent phase transition and chemical freeze-out is shown on the right side. The figure is taken from Ref. [8].

baryons can be stopped completely which leads to the creation of a hot nuclear matter with a high baryon content. At high beam momentum, colliding nucleons traverse each other and create a high energy density system with low baryon density. If the early stage of fireball reaches a sufficiently high temperature, the hadrons dissolve. The liberated quarks and gluons interact with each other leading to the creation of the Quark Gluon Plasma (QGP).

When the QGP expands, the temperature falls and hadronization begins. This is called the *mixed phase* as shown in the right part of Fig. 1.3. The matter further expands and is converted into hadron gas. Once the inelastic interaction between particles stops and hadron composition establishes, this is known as a "chemical freeze-out". The hadrons in the gas can interact elastically until it reaches the kinetic freeze-out. After kinetic freeze-out, the momentum (p) of the produced particle no longer changes by the strong interaction and freeze-out particles move away from the interaction point.

It is important to underline that even after the kinetic freeze-out, charged particles will be subjected to electromagnetic (EM) interactions. This issue, which in fact touches the central point of this thesis, will be discussed in more detail below.

1.5 Present status of ideas on the system created at SPS energies

In this section, the main present ideas on the system created in the nucleus-nucleus as well as p+p collisions in the energy range available to the CERN SPS [3] will be summarized.

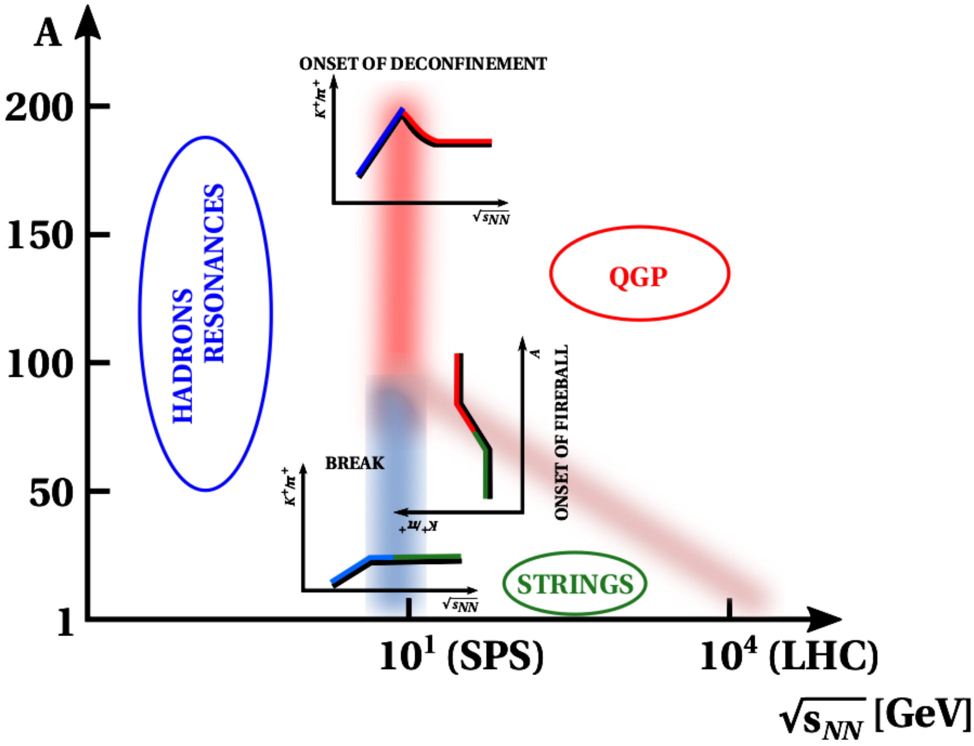

FIGURE 1.4: The summary of the ideas on the system created in high energy collisions as a function of system size and collision energy. The figure is taken from Ref. [9]. The three inserted plots illustrate the three patterns of evolution of the K^+/π^+ ratio corresponding to the three transitions described in the text.

---

[3] The Super Proton Synchrotron (SPS) located at the European Laboratory for Particle Physics (CERN).

Fig 1.4 shows, as a function of the collision center of mass energy and system size, the overall picture of an intermediate system of strongly interacting matter formed in high energy proton-proton and nucleus-nucleus collisions as it is postulated in Ref. [9]. This picture represents the amalgamate of existing ideas: the onset of fireball, the onset of deconfinement, and the resonance to string transition. In heavy-ion collisions, the NA49 experiment at SPS reported the observation of the onset of deconfinement [10], that is, the beginning of QGP state creation as a function of collision energy [11]. The transition between hadronic confined and deconfined phases can be explained by the Statistical Model of Early Stage (SMES) [12].

As shown in Fig. 1.4 up to $\sqrt{s_{NN}} = 10$ GeV independent from system size the hadron resonances (that is short-lived, excited states) would be formed. Later these resonances would decay into final state particles via the strong force.

At a lower size of the colliding system but higher energy ($\sqrt{s_{NN}} > 10$ GeV), resonances would be substituted by strings. Generally, string formation can be understood in the following, simplified way. When the two quarks from the target and projectile nucleons exchange a gluon, then the two initial nucleons will not be color neutral anymore. Then two new color-neutral objects ("color singlets") will each consist of two quarks from the original nucleon and one quark from the other nucleon. These color-neutral objects will elongate and propagate longitudinally, therefore are known as "strings". These strings decay via the creation of $q\overline{q}$ pairs [13] and consequently give mesons (and also baryons). The strings are confined in a small area in the transverse plane.

As the energy increases ($\sqrt{s_{NN}} \approx 100$ GeV), the larger length of strings produces a larger number of mesons ($q\overline{q}$), but the K^+/π^+ ratio stays constant. As one increases the size of the system, the large number of strings can overlap and form a "cluster" in which these strings interact with each other [14]. Later the strings collapse and create a large color-neutral object; this is called the "onset of fireball". In this state the degrees of freedom are not hadrons but quarks; this system is a QGP.

One of the major goals of the NA61/SHINE experiment is to detect the critical point (CP) of strongly interacting matter. It is defined as the location in the temperature-baryochemical potential phase diagram where the character of the phase transition changes from 1st order (at high baryochemical potential); to a cross-over (at low baryochemical potential). An enhancement of fluctuations of multiplicity and transverse momentum is expected to occur at the CP. As a function of $\sqrt{s_{NN}}$ and system size, collision conditions should exist where the freeze-out of the system should occur exactly at the CP or in very close proximity to it [15]. In principle, NA61/SHINE observations show no indication of the CP up to now. An intermittency signal was reported, which could possibly indicate the presence of the critical point in Ar+Sc reactions at 150A GeV/c [16]; however, a later analysis performed by a different methodology does not confirm this result [17]. As such, the situation remains inconclusive even if work continues [18].

1.6 This work

The work presented in this thesis largely consisted in the analysis of experimental data from the NA61/SHINE (SPS Heavy Ion and Neutrino Experiment) detector. NA61/SHINE is located in the North Area of CERN in Geneva, Switzerland. This is a fixed target experiment designed to study hadron production in hadron-proton, hadron-nucleus, and nucleus-nucleus collisions at CERN SPS energies. The experiment has two main goals :

1. To study the properties of the onset of deconfinement and search for the critical point of strongly interacting matter [19].
2. Precise measurements of hadron production, made in order to improve modelling of cosmic-ray air-showers and to improve calculations of the initial neutrino beam flux [20].

In the framework of the first program (1.), the NA61/SHINE experiment has collected data for reactions such as p+p, Be+Be, Ar+Sc, Xe+La, and Pb+Pb at beam momenta from 13A GeV/c to 150A GeV/c (up to 158 GeV/c for p+p reactions). The data for Ar+Sc collisions has been collected for six different beam momenta 13, 19, 30, 40, 75, and 150A GeV/c. The studies of Ar+Sc collisions provided an improved understanding of the change in the hadron production from small (p+p) to large (Pb+Pb) colliding systems.

In recent years the physics program of the NA61/SHINE experiment has been enhanced with studies of electromagnetic (EM) effects, induced on spectra of emitted charged particles by the charged spectator systems. The spectator systems are the residue of nuclei, parts of the nuclei which do not take a direct part in the collision (see also section 1.3). Their presence results in a distortion of the trajectories of emitted π^+ and π^- mesons, as well as other charged particles [21]. It is known that spectator-induced electromagnetic effects are sensitive to the space-time evolution of the non-perturbative process of particle production [22]. In this context, the first preliminary data on Ar+Sc reactions at 150A GeV/c ($\sqrt{s_{NN}} = 16.8$ GeV) for central and intermediate collisions have already been released [23]. This thesis presents new data on spectator-induced EM effects in Ar+Sc collisions at 40A GeV/c ($\sqrt{s_{NN}} = 8.76$ GeV), for the first time in the full range of centrality, ranging from central up to peripheral collisions. Consequently, it is the first measurement of spectator-induced EM effects in peripheral small systems at the CERN SPS [4]. The results presented in this thesis have been released as preliminary data of the NA61/SHINE collaboration. They have also been presented by the author at two scientific conferences MESON 2021 and EPS-HEP 2021 [25]. Furthermore, they were presented by fellow members of the collaboration at several other conferences including in particular the NA61/SHINE invited plenary talk at Quark Matter 2022 [24]. Additional aspects of the analysis, such as evaluations of systematic uncertainties and estimates of quantities relevant for collision centrality, have been carried out specifically for this thesis. The same applies to all the phenomenological investigations featured in Chapter 4.

The first model description of spectator-induced EM effects in heavy-ion collisions at SPS energies appeared in Ref. [22], for the case of peripheral Pb+Pb reactions at $\sqrt{s_{NN}} = 17.27$ GeV. As shown therein (see also Ref. [26]), the EM distortion of spectra and corresponding ratios of emitted π^+ and π^- mesons provides information on the distance between the pion formation zone and the spectator system (d_E). Later it has been established that d_E can be used to estimate the time of pion emission at mid-rapidity [26]. In the paper [27], the first-ever realistic, fully quantitative description of spectator-induced EM effects at SPS energies appeared. The study done in this paper brought independent information on the time scale for the creation of fast pions, which appeared significantly shorter than for the slow pions produced at mid-rapidity. Spectator-induced electromagnetic effects are also known to provide information on the interplay between the space-time evolution of

---

[4] In the text above we use the terminology applied in Ref. [24]. The Ar+Sc system is about five times smaller than in heavy-ion (Pb+Pb, Au+Au) collisions.

pion production and that of the spectator system [28, 29].

In this context, several opportunities provided by our analysis become evident, at the moment when a new set of experimental information (a new measurement of EM effects in a small system in the full range from very central to peripheral collisions) becomes available for the first time at the CERN SPS [25]. From the phenomenological point of view, this is the first experimental data that can serve to elucidate the centrality dependence of the space-time evolution of pion production for fast pions in a small colliding system at the SPS, and to understand its interplay with the space-time evolution of the (small) spectator system itself.

A separate issue concerns the understanding of the interplay between electromagnetic (EM) and isospin effects, as derived from the current study. In the specific context of this thesis, isospin effects refer to the manner in which the original isospin structure (proton/neutron content) of the nucleus reflects in the distribution of π^+/π^- ratios over phase space in nucleus-nucleus collisions. This analysis facilitates a comprehensive examination of the role played by isospin effects with respect to that played by the space-time evolution of pion production as a function of centrality. This is different from what was the case in the earlier study of peripheral Pb+Pb collisions [30], as in the latter case, the isospin effect was overshadowed by the dominant EM effect, resulting in partial "loss of information" on the isospin effect. In contrast, Ar+Sc reactions exhibit a smaller spectator system, leading to a more comparable magnitude of both effects. Moreover, full control over centrality (size of the spectator system, strength of EM effect) is available, which was not the case in Pb+Pb collisions.

What emerged from this is the important possibility to verify the existing models aimed to describe the interplay of EM, isospin, and other effects [22, 26, 30, 29, 27], and to investigate whether these relatively simple approaches would also work for Ar+Sc reactions. As the analysis results later will show, this will not be the case at least for the approach described in Refs. [30, 29], these models are too simplified.

Independently of the above, some remarks should be made in the context of the particular position of Ar+Sc data at $40A$ GeV/c ($\sqrt{s_{NN}} = 8.76$, $A = 40$ and 45) on the system-size/energy plane shown in Fig. 1.4. It is clear that EM effects do not provide any "explicit" information on postulated nature of the system as is the case e.g. for K^+/π^+ ratios. On the other hand, it is clear that they provide an *independent* information on the space-time evolution which then can be used to improve the understanding of the properties of the system, once it is known to which of three regimes (resonances, strings, QGP) this system belongs. An example of the latter, this is on the basis of the inspiration resulting from studies of EM effects [26] that it was established that in the entire "above-resonance" region (for p+p and Pb+Pb reactions at 40-158 A GeV/c), the longitudinal space-time evolution of the system is altogether rather "simple" and can be described by the Fire Streak (FS) approach, that is, by energy-momentum conservation [31, 32] [5]. In principle, the same can be done in future for Ar+Sc with its very interesting position with respect to the "critical structures" [6]. Thus in the end, it is hoped that the analysis presented in this thesis will contribute to a better understanding of the intermediate system of strongly interacting matter created in elementary and nuclear collisions in the energy range of the CERN SPS.

1.7 Definition of kinematical variables and physical quantities

For the sake of clarity, this section introduces the most important physical quantities and variables used in the analysis presented in this thesis.

1.7.1 Total, longitudinal and transverse momentum

The quadratic sum of all components of the momentum vector is defined as the total momentum.

$$p = \sqrt{p_x^2 + p_y^2 + p_z^2} \tag{1.1}$$

The longitudinal momentum $p_L = p_z$ shown in Fig. 1.5 is the particle momentum component parallel to the beam axis (z). The transverse momentum (p_T)

---

[5] Studies of spectator-induced EM effects summarized in Ref. [26] provided information on the decrease of the distance d_E between the pion formation zone and the spectator system as a function of pion rapidity, which served as the basis for the phenomenology introduced in papers [31, 32]. The term "Fire Streak" underlines the partial similarity to earlier models [33, 34, 35, 36, 37, 38].

[6] Expression proposed by Marek Gazdzicki, marking the transitions between the different areas of the diagram shown in Fig. 1.4.

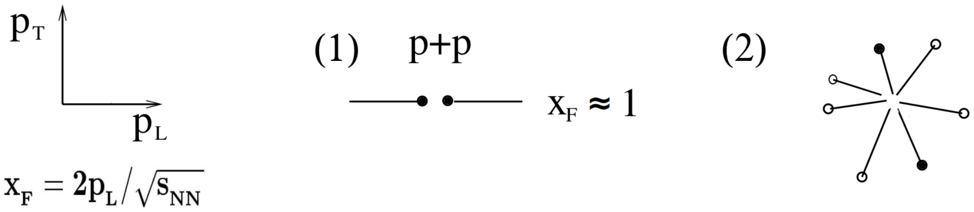

FIGURE 1.5: Definition of the longitudinal momentum p_L, the Feynman variable x_F, and the transverse momentum p_T, drawn with respect to the initial and final state of the inelastic p+p collision, (1) and (2) respectively. The incoming protons (1) have initial x_F close to ±1 whereas the final state particles (2) have extended distributions in x_F and p_T. The black circles define baryons before and after the collision. The white dots denote mesons. The figure is adapted from Ref. [29].

also shown in Fig. 1.5, is defined as follows;

$$p_T = \sqrt{p_x^2 + p_y^2} \tag{1.2}$$

where p_x and p_y are particle momentum components perpendicular to beam axis (z).

1.7.2 Rapidity (y)

Rapidity can be understood as a generalized relativistic velocity of the particle which is characterized by its longitudinal momentum p_L and total energy E. It is defined as:

$$y = \frac{1}{2} ln \left[\frac{E + p_L}{E - p_L}\right] = ln \left[\frac{E + p_L}{m_T}\right], \tag{1.3}$$

where $m_T = \sqrt{m^2 + p_T^2}$, m is the particle mass. The major advantage of using rapidity is that under Lorentz boost, it transforms additively.

1.7.3 Collision energy

In a high-energy collision of two particles with masses m_{beam} and m_{target}, the total center of mass energy can be defined as :

$$\sqrt{s} = \sqrt{(E_{beam} + E_{target})^2 - (\vec{p}_{beam} + \vec{p}_{target})^2} \tag{1.4}$$

In a relativistic nucleus-nucleus collision, the center-of-mass energy per nucleon pair, $\sqrt{s_{NN}}$ is used.

1.7.4 Feynman x (x_F)

The variable was introduced by Richard Feynman, it is a scaling variable used for studying the distributions of the longitudinal momentum of the produced particle. The original idea was to compare the behaviour of particle production at different collision energies. In the framework of this thesis, this variable will be used to investigate the electromagnetic distortion of charged pion ratios in a way similar to that from Refs. [22, 30, 39] and will be taken exclusively in the c.m.s. system. It is defined as follows;

$$x_F = \frac{2p_L}{\sqrt{s_{NN}}} \tag{1.5}$$

1.7.5 Centrality/Forward energy (E_F)

The degree of overlap of two colliding nuclei defined e.g. in terms of the impact parameter or the number of participant nucleons cannot be directly determined experimentally. In this thesis, impact parameters and other centrality estimates are deduced from the measurement of the forward energy deposited by the spectator system. This will be explained in detail in Chapter 3.

1.7.6 The π^+/π^- ratio

The main physical observable used in this thesis is the ratio of double differential densities of the produced π^+ over the produced π^- mesons:

$$\pi^+/\pi^- = \frac{\frac{d^2n}{dx_F dp_T}(\pi^+)}{\frac{d^2n}{dx_F dp_T}(\pi^-)} \tag{1.6}$$

studied as a function of pion x_F and p_T in the collision c.m.s. As spectator-induced EM effects correspond to repulsion (attraction) of positively (negatively) charged pions by the positively charged spectator systems, the distribution of this quantity over phase space is an observable very well suitable for experimental and phenomenological studies of such effects, as it was demonstrated in Refs. [40, 41].

1.8 Outline of this thesis

The remainder of this thesis is organized as follows.
Chapter 2 presents the NA61/SHINE facility and detectors.
Chapter 3 contains a discussion of the analysis methodology and systematic uncertainties.
Chapter 4 presents the results of the experimental data analysis of electromagnetic effects induced by the spectator systems in Ar+Sc collisions at 40A GeV/c beam momentum. Moreover, a comparison between the experimental data obtained and dedicated Monte Carlo model simulations will be discussed.
Chapter 5 summarizes the thesis and presents the conclusions.

Chapter 2

Experiment

This chapter describes the facility and detector setup of the NA61/SHINE experiment, focusing on features relevant for the analysis presented in this thesis. The description made in this chapter is largely based on Refs. [42, 43, 6, 7] where further and more detailed information about the NA61/SHINE detector can also be found. The schematic layout of the NA61/SHINE detector is shown in Fig. 2.1. In this chapter, the main experimental instrumentation will be described in detail, focusing on the features most relevant for this study.

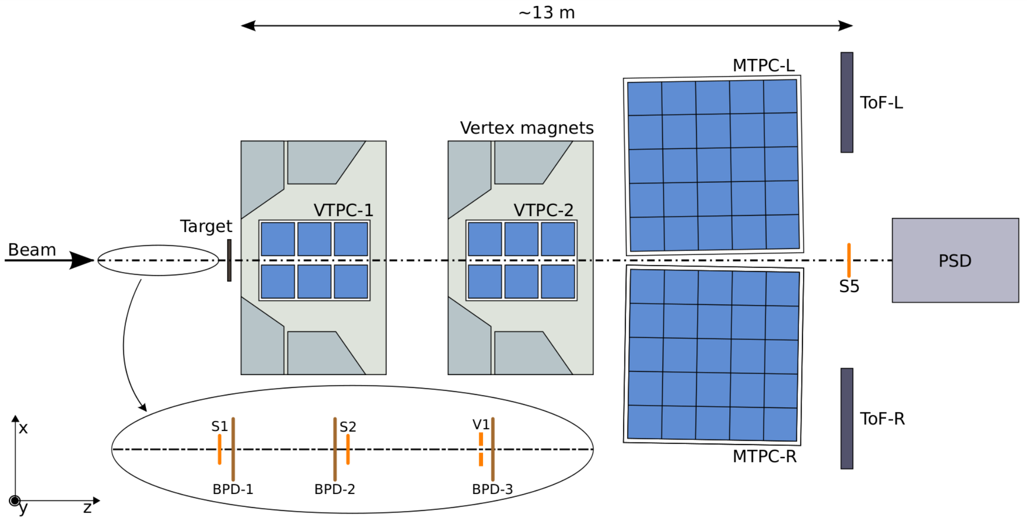

FIGURE 2.1: Schematic layout of the NA61/SHINE experiment at CERN SPS during Ar+Sc data taking. The right-handed coordinate system is chosen as shown in the plot. Figure taken from Ref. [44].

The detector system of NA61/SHINE [1] consists of a set of four Time Projection Chambers (TPCs). The TPCs are the main tracking and particle identification detectors. Due to its large acceptance, the NA61/SHINE TPC system allows for precise measurement of charged particles produced in the forward c.m.s. hemisphere of the collision. Two TPCs are positioned inside the superconducting magnets (VTPC-1 and VTPC-2) to bend the charged particle trajectories in the x-z plane, providing momentum measurement. Two other large TPCs, MTPC-L and MTPC-R, provide charged particle identification. The set of two Time-of-Flight detectors (ToF) is stationed downstream from the TPC. The high-resolution modular forward calorimeter, the Projectile Spectator Detector (PSD) measures forward energy (E_f) allowing centrality selection.

Particle identification plays a key role in the bulk of measurements performed by NA61/SHINE, including the one made in the present thesis. Generally, NA61/SHINE allows two different methods of particle identification:

- Charged particles, i.e. $p, \bar{p}, K^{\pm}$ and $\pi^{\pm}$ passing through the active volume of TPCs can be identified via measurements of their specific energy loss (dE/dx) in the TPC gas. This can be performed in a wide range of longitudinal and transverse momentum, typically with no lower p_T cutoff i.e. starting from $p_T = 0$ (sharp).

- ToF measurements can be combined with dE/dx measurements which then allows a better separation of charged particles in a relatively narrow acceptance range.

In this thesis, for particle identification, only the specific energy loss (dE/dx) has been used. The ToFs were not used for the present analysis. This is because this thesis is concerned with spectator-induced EM effects. These effects are characteristic mostly for fast pions at reasonably large longitudinal lab momentum. Moreover, they extend over a wide range of the latter.

The different elements of the NA61/SHINE beam and detector setup will be presented in more detail below.

---

[1] It is worthwhile to underline that the description made in this chapter summarizes the setup of the NA61/SHINE detector during Ar+Sc data taking, and before its very significant upgrade completed in 2022. Among others, the upgrade supplemented this setup with a new vertex detector, new electronics of Time Projection Chambers readout, a geometry reference chamber, and many others [45].

2.1 The coordinate system of NA61/SHINE

The coordinate system used in NA61/SHINE is shown in Fig. 2.1. The origin of the coordinate system (0,0,0) is located in the center of the vertex magnet-2 (VTPC-2 chamber), on the beamline. All coordinates and angles are defined in the lab reference frame. The coordinate axes are defined as follows. The z axis is horizontal and aligned with the beamline. The x axis is horizontal and perpendicular to the latter. The y axis is vertical. The azimuthal angle ϕ, also often used to describe the particles produced in the interaction, is defined in the $x - y$ plane. It is the angle between the transverse momentum vector ($\vec{p_T}$) and the x axis:

$$\phi = \text{atan}\left[\frac{p_y}{p_x}\right] \tag{2.1}$$

The ϕ angle ranges from 0 to 2π.

2.2 Beams

The NA61/SHINE experiment benefits from the availability of both primary and secondary beams, which allows data taking with protons as well as nuclear projectiles up to lead. Before getting delivered to the NA61/SHINE target, the primary beam passes through the CERN acceleration chain, as shown in Fig. 2.2.

In the case of primary *proton* beams, the acceleration chain is shown in Fig. 2.2 in blue colour. The proton beam is extracted from the hydrogen gas by a duoplasmatron ion source [46]. The beam is then accelerated to 750 keV/c in the Radio-Frequency Quadrupole known as RFQ2 (not shown in the Figure) [47]. In the next stage, the LINAC2 is used which accelerates protons up to 50 MeV/c. Subsequently, the beam is distributed in four rings of the Proton Synchrotron Booster (PSB), where it reaches a momentum up to 1.4 GeV/c. In the further stage, the Proton Synchrotron (PS) accelerator increases the beam momentum up to 14 GeV/c and then delivers it to SPS which then accelerates the beam up to maximally 400 GeV/c. From SPS the beam is finally transferred to the North Area.

For the primary *ion* beam, the acceleration chain is shown in Fig. 2.2 in green colour. The process begins with the ionization of atoms in an electron

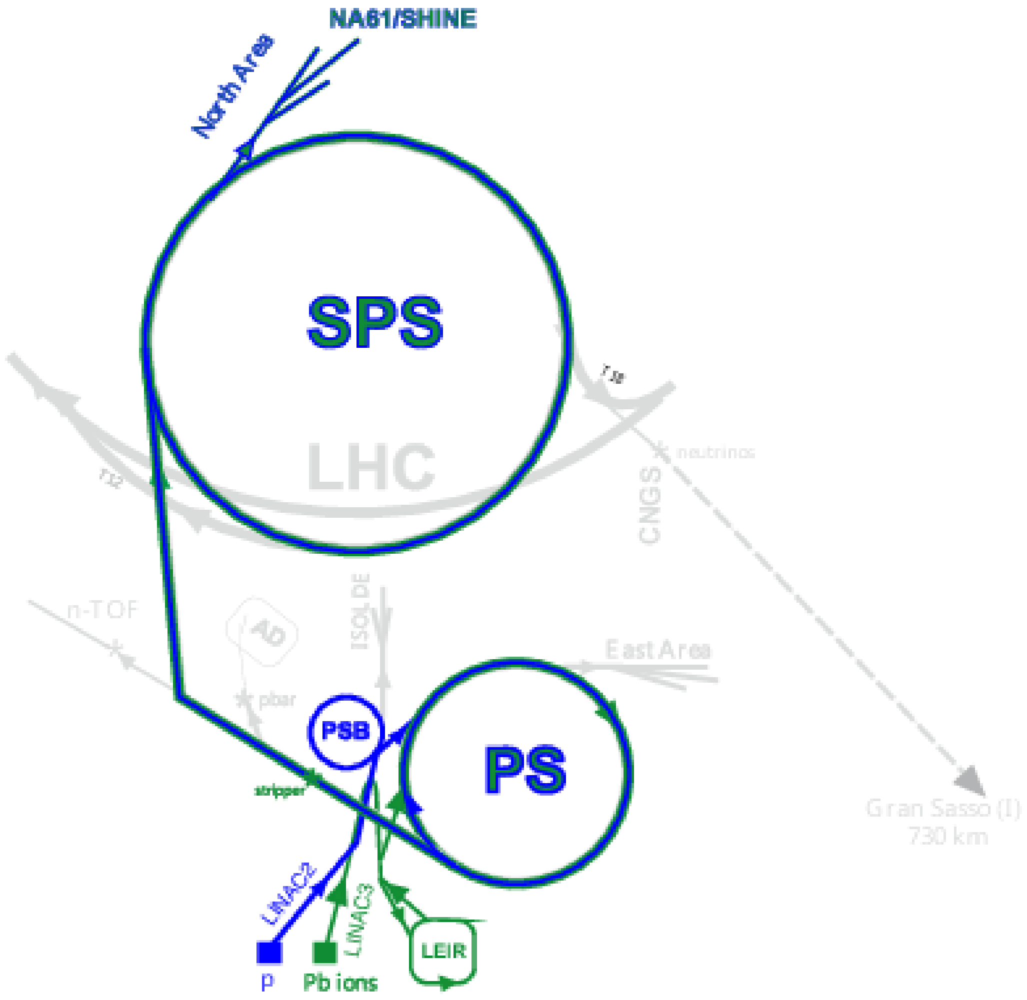

FIGURE 2.2: Schematic of CERN accelerator complex up to the SPS. Figure taken from Ref. [42].

cyclotron resonance (ECR). The ions are extracted with the momenta of 2.5A keV/c into the separator. In the next stage, the Radio-Frequency Quadrupole raises the momentum of the beam to 250A keV/c. Later LINAC3 is used where the beam accelerates to the momentum of 4.2A MeV/c. Then the beam enters into the Low Energy Ion Ring (LEIR), where it reaches the momentum of 72A MeV/c and then it is transferred to the PS where it is accelerated to 5.9A GeV/c. Afterwards, the beam goes through the stripping stage where the electrons get stripped off and leave a fully ionised ion beam. This fully ionized beam enters the SPS where it reaches the momentum up to 158A GeV/c and then it is extracted to the North Area.

In the case of *secondary* beams (p, k, π and Be), the extracted primary beam from the SPS is guided to hit the Primary Target (PT). A set of dipole magnets helps to optimize and modify the incident angle of the primary beam on PT. The PT hosts beryllium (Be) plates of different lengths. The beams of NA61/SHINE are produced using a target length of 100 or 180 mm [42]. A specific target plate is chosen for the best optimization of the requested secondary particle (or ion) momentum and type.

After reaching the desired momenta in the SPS, both primary and secondary beams are extracted through the H2 beamline. The H2 beamline can provide a wide range of beam momenta from 13A GeV/c up to 158A GeV/c to the Experimental Hall North 1 (EHN1). The PT is 535 m away from the "production" target shown in Fig. 2.1. The H2 beamline includes two large magnetic spectrometers and multiple collimators to select the desired mean momenta of both primary and secondary beams for the final collision with the production target of NA61/SHINE. Apart from the magnetic spectrometer, the beamline is facilitated with several apparatuses such as bending and focusing (quadrupole) magnets, collimators and beam position detectors to provide information on precise timing reference, along with position and charge measurement of the beam at different locations.

In this thesis, Ar+Sc data obtained with the primary Argon beam are discussed. Altogether these Ar+Sc data were collected at six beam momenta (13, 19, 30, 40, 75 and 150A GeV/c). The analysis made here focuses on the intermediate momentum of 40A GeV/c.

2.3 Beam detectors and trigger system

The trigger system of NA61/SHINE is designed to handle and select a variety of reactions using different beams. The configuration is schematically shown in the following Fig. 2.3. A set of scintillators (S1, S2, S5, V1) and beam position detectors (BPDs) placed on the beamline provide precise information on the time reference and position of incoming beam particles. Minimising the total detector material in the beamline is an important concern, especially for ion beams; this is why plastic scintillator counters are used. The S1 (6×6 cm^2) is located upstream of BPD1 and S2 (4×4 cm^2) downstream of BPD2 as shown in the Fig. 2.3. BPD counters are proportional chambers operated with an Ar+CO$_2$ (85 + 15) gas mixture. The V1 (10×10 cm^2) with a hole in the middle, is used in veto mode for triggering on the incoming beam particles. The S5 is the interaction counter that corresponds to the beam interacting with the target (it is put in veto mode, meaning that the interaction trigger corresponds to no beam particle passing through S5).

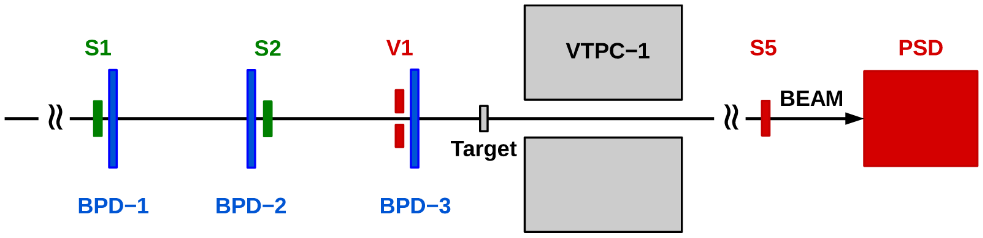

FIGURE 2.3: Schematic layout of beam and trigger configuration during the Ar+Sc run. The figure is taken from Ref. [6].

The trigger logic for Ar+Sc collisions is shown in Table 2.1. It is based on two major blocks: the *beam* logic and *interaction* logic. The logic involves signals from scintillator counters S1, S2, as well as S5 and V1 in veto mode. Additionally, the signal from the PSD calorimeter is used in order to trigger on central Ar+Sc events: if the signal is below a given threshold, the event will be recorded as a central interaction (this implies that for triggering on central collisions, the PSD signal is also used in veto mode). The T1 is "pure beam logic", it represents the positive signal from S1 and S2 which ensures the beam alignment is decent and a veto in the V1 counter to eliminate the beam halo. The T2 and T4 are interaction triggers: the signal from S5 informs whether the beam particle interacted with the target or not, and the signal from PSD ensures that the interaction was central. Additionally, the T3 trigger also corresponds to the beam but includes the halo. The data is collected simultaneously by all four triggers with different proportions. Most of the data is collected with the T2 trigger corresponding to central Ar+Sc collisions. However, what is of principal interest for the present thesis is the minimum bias interaction trigger T4.

Name	Definition	Description
T1	$\mathrm{S1} \cdot \mathrm{S2} \cdot \overline{V1}$	beam
T2	$\mathrm{S1} \cdot \mathrm{S2} \cdot \overline{V1} \cdot \overline{S5} \cdot \overline{PSD}$	PSD central interaction
T3	$\mathrm{S1} \cdot \mathrm{S2}$	beam halo
T4	$\mathrm{S1} \cdot \mathrm{S2} \cdot \overline{V1} \cdot \overline{S5}$	min. bias interaction

TABLE 2.1: A list of trigger logic definitions used during the Ar+Sc run. Information is taken from Ref. [6].

2.4 Targets

The targets used by the NA61/SHINE experiment are stationed upstream of the VTPC-1. So far NA61/SHINE has collected data using targets made of liquid hydrogen, Be, C, Al, Sc, La and Pb. Usually, the solid targets have a thickness of 0.5 mm to 2 cm. Most of the targets are placed in an aluminium container, filled with helium gas at atmospheric pressure. The helium gas helps to reduce the background off-target collisions in the proximity of the target and also reduces the oxidation of the target. The target can be removed from the beamline with the help of a pneumatic piston. This allows the collection of data without the target ("target out" data) to measure the background interactions.

A Scandium target is achieved by using an isotopically pure (99.99%) stack of six plates of ^{45}Sc (2.5 × 2.5 cm^2) with a thickness of 1mm stationed at 80 cm upstream of VTPC-1. The ^{45}Sc target samples were checked for possible contamination using the Wavelength Dispersive X-Ray Fluorescence (WDXRF) method. The measured mass concentration impurity level was 0.37%. The impurities in the target result in a small increase in overall pion multiplicity due to the presence of heavier elements such as Ti, Ta, Al, Cu, and Fe. This increase was estimated to be less than 0.2% [48].

2.5 Time Projection Chambers (TPCs)

This set of detectors is the most important for this analysis; therefore its operation will be explained in more detail. The track in TPC is reconstructed in three dimensions. The pad plane provides x and z coordinates while the y position is derived from the drift time Δt.

2.5.1 Layout and basic characteristics of NA61/SHINE TPCs

The tracking system of the NA61/SHINE experiment consists of four TPCs [2]. These provide a complete measurement of charged particle trajectories in three dimensions and of the corresponding ionization energy deposits in the chambers.

---

[2] As mentioned at the beginning of this chapter, the description made here addresses the status of the experiment during Ar+Sc data taking.

Two of the TPCs, VTPC-1 and VTPC-2, are located inside two superconducting dipole magnets, VTX-1 and VTX-2, providing magnetic fields up to 1.5 T and 1.1 T, respectively. The latter values are used for the highest beam momenta (150A GeV/c). The superconducting magnets have a maximum bending power of 9 Tm. At lower beam momenta, the magnetic field in VTPCs is reduced proportionally to the beam momentum in order to provide a similar acceptance at different collision energies. Each VTPC has a readout surface at the top of 2.5 $\times$ 2.0 m^2 and a height of about 1 m. It is filled with a gas mixture of Ar/CO$_2$ in the proportion of 90/10. The two large TPCs, MTPC-L and MTPC-R are positioned downstream of the magnets, symmetrically with respect to the beamline. Each MTPC has a readout surface at the top of 3.9 $\times$ 3.9 m^2 and a height of about 1.8 m. It is filled with a gas mixture of Ar/CO$_2$ in the proportion of 95/5. The lower CO$_2$ content in the MTPCs is required to obtain the higher drift velocity necessary to read out the longer drift length. The synopsis of the important parameters of the four TPCs is given in Table 2.2.

	VTPC-1	VTPC-2	MTPC-L/R
Size(L× W× H)[cm]	250× 200× 98	250× 200× 98	390× 390× 180
No. of pads/TPC	26 886	27 648	63 360
Pad size[mm]	3.5× 28(16)	3.5× 28	3.6× 40,5.5× 40
Drift length[cm]	66.60	66.60	111.74
Drift velocity[cm/μs]	1.4	1.4	2.3
Drift field[V/cm]	195	195	170
Drift voltage[kV]	13	13	19
Gas mixture	Ar/CO2 (90/10)	Ar/CO2 (90/10)	Ar/CO2 (95/5)
No. of sectors	2× 3	2× 3	5× 5
No. of padrows	72	72	90
No. of pads/padrow	192	192	192,128

TABLE 2.2: Parameters and dimensions of the NA61/SHINE Time Projection Chambers [2, 42].

2.5.2 Construction and working principle of TPC

The NA61/SHINE TPC is made of two main elements, a drift chamber and a Multi-Wire Proportional Chamber (MWPC). The drift chamber provides the active detection volume and MWPC provides the readout. Fig. 2.4 shows a simplified scheme of detection of a charged particle by the TPC.

Drift Chamber

The TPC drift chamber is a cage filled with a mixture of a noble gas (Ar) and a small amount of quenching gas (CO_2). The noble gas is prone to ionization whereas the quenching gas suppresses the uncontrolled growth of the electron avalanche. Field-shaping electrodes are used to generate a uniform electric field, called a drift field, in the active volume of the TPC.

When a charged particle passes through this active volume, it ionises the gas atoms, producing electrons and positive ions as shown in Fig. 2.4. The electrons drift under the influence of the electric field towards the readout plane with a given drift velocity v_D.

Gating grid

The MWPC is separated from the drift volume by a wire plane, known as the gating grid. The gating grid isolates the readout from drifting charges in between the triggered events. The drifting electrons pass through the gating grid and arrive to readout chamber.

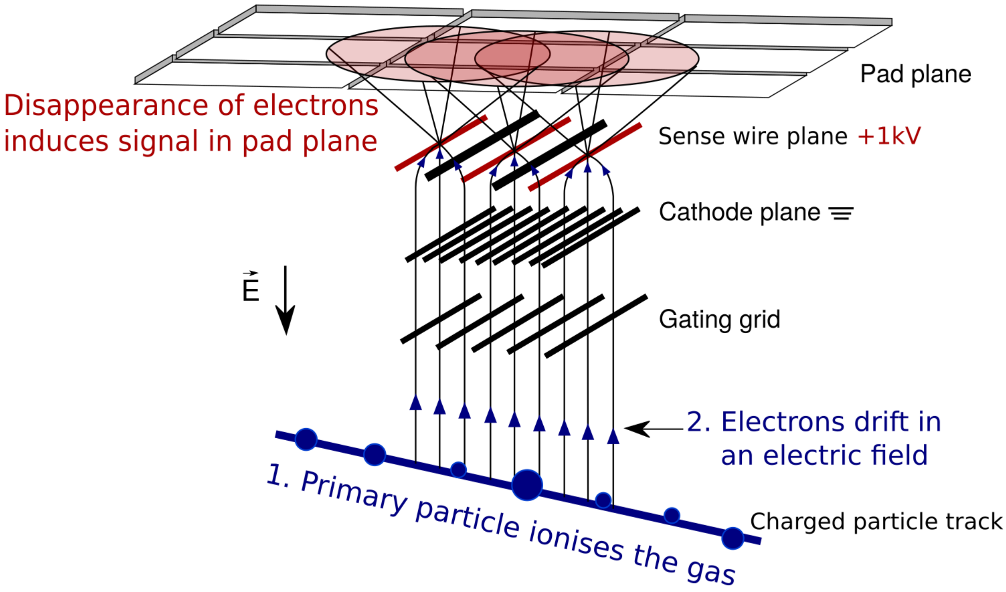

FIGURE 2.4: Schematic layout of TPC with MWPC readout. The figure is taken from Ref. [43].

MWPC

The electrons produced in ionization are relatively too small in number to be directly detected by the electronics readout (of the order of several tens per centimetre). The readout and the corresponding amplification are realised on the basis of the technique described in Ref. [49]; this will be explained below.

The MWPC is made of two parallel cathode planes surrounding the anode sense-wire plane. The first cathode plane, closer to the gating grid, is made of wires in order to provide a uniform electric field inside the active volume of the TPC, whereas the second one is a solid plane subdivided into pads.

The anode sense wires generate a high-gradient electric field, which leads the drifting electrons to accelerate and repeatedly collide with the gas atoms causing the secondary ionization to create an avalanche of electrons. This is collected by the sense wires, inducing an electric signal on the pad plane. The obtained electric signal has a 2D structure (i.e. it provides the information on the x and z coordinates). Account taken of the fact that the y coordinate is provided by the time of the drift, this gives the reconstruction of the track in the entire xyz space.

2.5.3 Particle identification via ionization energy loss

As it is apparent from the description made in section 2.5.2 above, from the point of view of the data analysis it can be said that the charged particle passing through the TPC leaves a stream of ionization *clusters* along its trajectory (a cluster is not a physical object, it is built from signals on a given pad row).

The charge of the cluster is proportional to the energy deposited in the gas by the incident charged particle; from this charge, the energy loss per unit length (dE/dx) can be calculated. The energy loss measurement performed in the NA61/SHINE TPCs is based on the "truncated mean" calculation from the charge distribution of all the clusters along the particle track. This consists in selecting 50% of the lowest dE/dx deposits and calculating the truncated mean on their basis. This method significantly reduces the very sizable fluctuations induced by the Landau distribution inherent to the ionization process.

The average ionization energy loss per unit length is a function of the velocity of the particle, as described by the Bethe-Bloch formula [50]. When the truncated mean dE/dx is plotted as a function of the particle's laboratory momentum, this gives a typical 2D distribution as shown in Fig. 2.5. The energy loss functions describing the truncated mean dE/dx as a function of momentum, commonly known as the "Bethe-Bloch functions", are also included in the plot. As apparent in Fig. 2.5, the separation of the different particle types as a function of their laboratory momentum, combined with the knowledge of their energy loss functions, allows for the isolation of clean samples of charged pions (and protons) in a relatively large range of momenta. This separation will serve as a basis for the particle identification techniques used in this thesis.

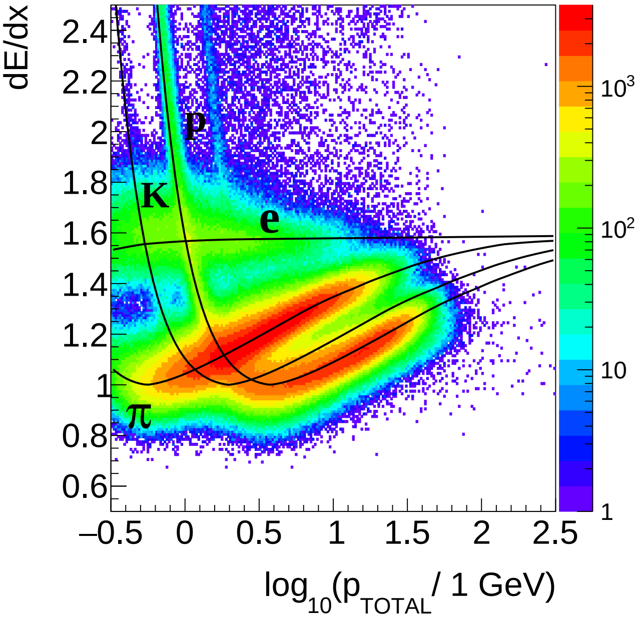

FIGURE 2.5: The distribution of truncated mean dE/dx as a function of total lab momentum for positively charged particles produced in Ar+Sc collisions at 40A GeV/c. Black curves represent the energy loss functions ("Bethe-Bloch functions") for the different particle types: protons (p), kaons (K), pions (π) and positrons (e).

2.6 Time of Flight (ToF)

Although this set of detectors was not used in the analysis presented in this thesis (see the introduction to this Chapter), it is included in the present description of the NA61/SHINE experiment for completeness. Additional and independent particle identification can be performed by two time-of-flight detectors: left ToF-L and right ToF-R. The basic component of each of these detectors is an array of scintillators. Both ToF-L and ToF-R consist of 891 individual rectangularly shaped scintillators with a photomultiplier glued on their short side.

The ToF detectors measure the time taken by the particle to move between the production point and the detector, called tof. By combining the information from the particle's time of flight (tof) with the track length (l) and momentum (p) measured in the TPCs, the particle's squared mass can be extracted on the basis of equation 2.2 with a given resolution specific to the detector (see Ref. [7, 6] for more details).

$$m^2 = p^2 \left[\frac{c^2 tof^2}{l^2} - 1 \right]. \tag{2.2}$$

The usage of ToF detectors (combined with dE/dx measured in TPCs) is particularly useful for identifying kaons but remains limited to a relatively narrow range of acceptance at lower momenta. The present analysis of pions was performed in a large acceptance corresponding to a wide range of pion longitudinal momentum up to and beyond beam rapidity as it will be apparent in Chapters 3 and 4, which is the main reason for constraining it to dE/dx identification alone. Such a "dE/dx-only" analysis is, in fact, a continuation of the approach taken in numerous earlier papers [51, 52, 53, 54], as well as several doctoral theses (see, e.g., [55]).

2.7 Projectile Spectator Detector

The Projectile Spectator Detector (PSD) is a zero-degree hadronic calorimeter; it is shown in Fig. 2.6 (c). It measures the energy emitted in the forward direction in a nucleus+nucleus collision. This forward energy E_F is used to select the centrality of the collision both at the trigger level (section 2.3) and at the level of data analysis (as it is the case in this thesis). The PSD calorimeter

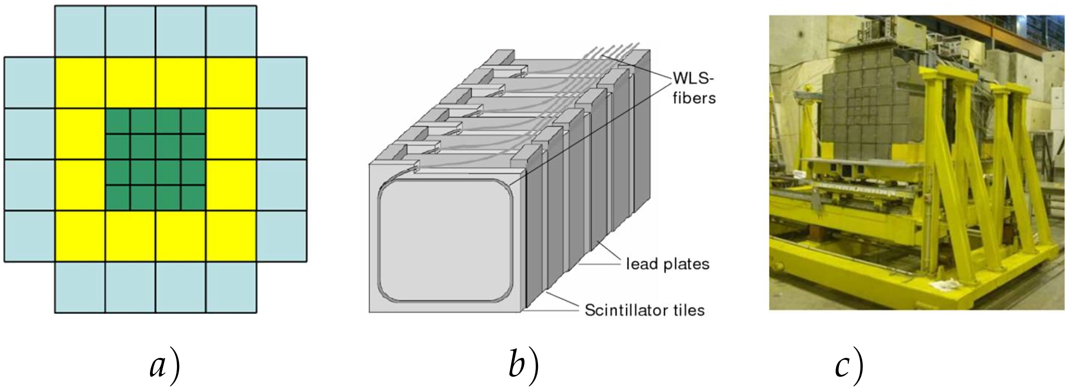

FIGURE 2.6: Schematic front view of PSD modules (a), schematic view of single module (b) and fully assembled PSD detector (c). The figure is taken from Ref. [42].

consists of 44 modules which cover a total transverse area of 120 × 120 cm^2 as shown in Fig. 2.6 (a). The central part of the PSD consists of 16 small modules with transverse dimensions of 10×10 cm^2 which weigh 120 kg each. The outer part of the PSD consists of 28 large (20 × 20 cm^2) modules which weigh 500 kg each. Every module consists of 60 pairs of alternating lead plates and scintillator tiles with 16 mm and 4 mm thickness, respectively, see Fig. 2.6 (b). The light readout is provided by Wavelength Shifting (WLS) optical fibres embedded in scintillator plates. It is used to achieve high detection efficiency.

As the incident particle hits the given PSD module, it produces a particle cascade. This cascade has electromagnetic and hadronic components. The cascade deposits energy over the module in the detector material, which can be sampled by the scintillator plates [56].

The construction and operation of the NA61/SHINE experiment and most of all the operation of the beam counters, the trigger, the TPC system and the PSD define the specific experimental analysis described in this thesis. The details of this experimental analysis will be explained in the next chapter.

Chapter 3

Analysis

This chapter outlines the procedure of experimental analysis. Prior to a comprehensive discussion of the latter, the basic terminology is introduced below.

An interaction of an Ar ion with the Sc target is regarded as a single *event*, while the trajectory of a charged particle generated during the collision and detected by the NA61/SHINE TPC system is referred to as a *track*. Each recorded event contains information pertaining to the incoming beam, the interaction point, and the particle tracks.

The data of good quality is subjected to further analysis in view of the physics of interest, starting with the implementation of a series of different *cuts* applied to both events and tracks. These cuts, the extraction of experimental results, and the corresponding experimental uncertainties are explained in a step-by-step manner within this chapter.

3.1 The data

The initial assessment of the data entails evaluating its time stability, the quality of the measured raw signal, and the performance of the sub-detectors. The unprocessed data obtained directly from the data acquisition system is commonly known as *raw data*. The raw data subsequently undergoes a first step of analysis, which encompasses event reconstruction and calibration. During the reconstruction process, the raw quantities registered by the detector are transformed into particle trajectories and related parameters, such as particle charge and momentum. At the same time, the calibration process involves rectifying inaccuracies induced by the raw detector response and present in the measured data. Following these procedures, analysts then apply selection criteria, or cuts, based on the specific physics of interest.

The Ar+Sc collision data at $40A$ GeV$/c$ was analyzed in this study. Data were collected for both target IN and target OUT. The target OUT data (with the target removed) was collected to estimate the magnitude of background events resulting from the interaction of beam particles with the gas and other material surrounding the target, commonly known as off-target events.

3.2 Event selection

The present analysis includes the entire range of centrality of Ar+Sc collisions (with the only exception of a small portion of very peripheral events as explained below). The data selected for this study was obtained through the minimum bias trigger (T4) as defined in Table 2.1.

BPD status

The acceptance of an event into the analysis is contingent upon the precise measurement of the trajectory of the beam particles by the BPD-1, BPD-2, and BPD-3 detectors (see Fig. 2.3). These detectors provide measurements in both x and y directions. The BPD status cut ensures a high-quality trajectory. Moreover, the presence of a signal from BPD-3 provides information that the beam particle did not interact *upstream*, that is before colliding with the target.

Cuts on off-time particles

There is a possibility that two, or more beam particles arrive within a short time interval and therefore enter a single triggered event. In order to eliminate such events, two distinct cuts were established. The first cut utilizes the signal from the beam counter (S1) and eliminates events where any additional beam particle appeared within ± 4 μs from the trigger beam particle. The second cut involves the trigger signal (T4) and discards any event in which an off-time particle interacted within ± 25 μs from the trigger particle. This time window of 25 μs was set up in order to match the duration of the TPC data collection period.

Quality of the main vertex

The presence of the primary interaction vertex is imperative since the current analysis is based on the tracks emanating from the primary vertex. In this study, the vertex quality flag is requested to be "ePerfect". This selection criterion guarantees that the reconstruction of the primary vertex was accurately accomplished, with high fitting quality.

Position of the main vertex

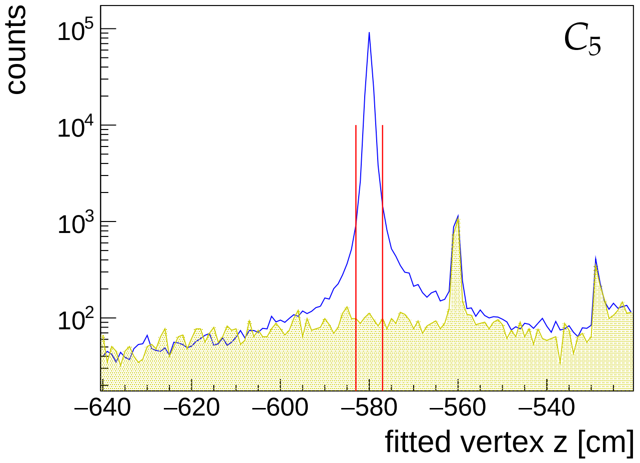

FIGURE 3.1: Primary vertex position distribution along the beam axis for peripheral Ar+Sc collisions at 40A GeV/c. The solid blue line represents the target IN data. The shaded area represents scaled target OUT data. The vertical red lines correspond to the cut ± 3 cm used in this analysis.

The x and y positions of the main interaction vertex are taken from BPD measurement, and the z position is fitted with TPC tracks coming out. Fig. 3.1 presents the distribution of the z coordinate of the main vertex for target IN and target OUT data. The target OUT distribution is marked with yellow colour whereas the target IN distribution is marked with blue colour. The target OUT distribution is normalized with respect to target IN data in a way to be consistent with the target IN from the range -630 to -600 cm as shown in Fig 3.1. The normalisation factor is then calculated by division of these two histogram entries, it is 2.66. The fitted vertex position peaked at z = -580 cm, which is the nominal position of the target. In order to minimize the contribution of background events from off-target interactions, only events with a primary vertex position z within (red vertical lines) ± 3 cm around the target are accepted. The resulting contribution of off-target interactions in the data analysis sample remains below 0.3% for the worst case of peripheral collisions presented in Fig. 3.1.

Cuts on forward energy and event centrality selection

In the present analysis, collision centrality is determined by the energy that has been deposited in the PSD calorimeter. This measure, known as forward energy (E_F), has been defined based on prior studies performed by experts of the NA61/SHINE collaboration. It represents the sum of the total energy deposited in 28 modules that are visually highlighted in green and yellow in Fig. 2.6.

In general terms, the energy deposit in the PSD originates from both the non-interacting nucleons (spectators) and the produced particles. In peripheral events, the spectators carry a higher total energy, which results in a greater energy deposition in the calorimeter, while in central collisions, the deposited energy is comparatively lower.

The above selection of 28 modules results from the analysis of the correlation between the energy deposited in each module of the PSD and the total track multiplicity of the produced particles. The track multiplicity refers to the number of tracks fitted to the main vertex and will be referred to as $nTracks$ from now on. A positive correlation between $nTracks$ and the energy deposit in a given module indicates that the latter is predominantly due to the produced particles, whereas an anti-correlation signifies that the module is occupied primarily by the spectators. Thus, only the modules that exhibit an anti-correlation are selected for the calculation of the forward energy E_F [57]. This anti-correlation will be further addressed below in this section.

The distribution of forward energy is presented in Fig. 3.2. Only events with $E_F < 1400$ GeV are accepted in this analysis. This eliminates very peripheral Ar+Sc events which are expected to be most sensitive to a possible charge-dependent T4 trigger bias, potentially problematic for the measurement of π^+/π^- ratios which is the aim of this study. As it will appear in Chapter 4, the latter does not constitute a serious limitation of this analysis in view of the slow centrality dependence of EM effects in the peripheral sector.

The vertical black lines in Fig. 3.2 indicate the different forward energy (centrality) classes selected for the present study and will be further discussed below.

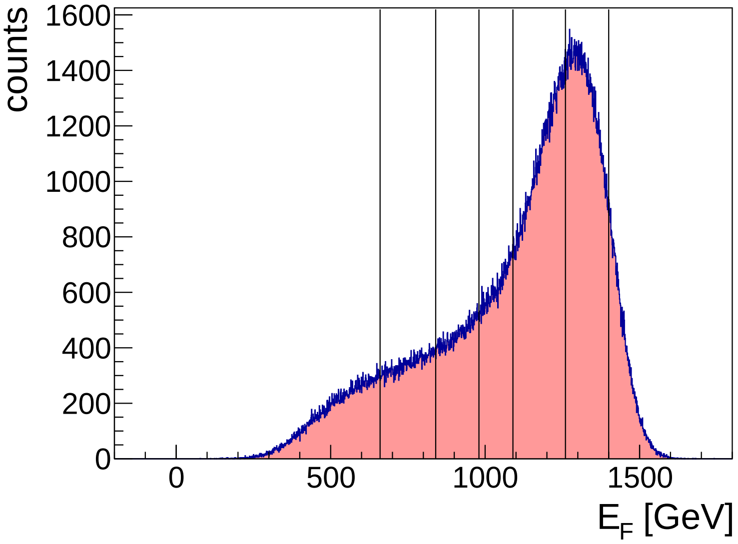

FIGURE 3.2: Distribution of forward energy E_F measured by PSD and used in this analysis. The distribution is obtained after all the event selection cuts except geometric and *nTracks* (discussed in the text below). The vertical black lines indicate the centrality classes selected for this study. Only events with $E_F <$ 1400 GeV are used in the analysis.

The "geometric" cut

In the study discussed here, we examine in detail the anti-correlation between E_F and track multiplicity. The plots in Fig. 3.3 display the distribution of *nTracks* as a function of E_F. The rectangle in Fig. 3.3 (a) depicts a cluster of events, which does not conform to the anti-correlation. Such events, with relatively low multiplicity, are clearly problematic in view of the centrality selection by forward energy as discussed above and consequently must be removed from the analysis [1]. Consequently, a simple cut, labelled as a "geometric cut" from now on has been devised based on the track multiplicity

---

[1] Such events can be caused by energy leaks in PSD modules or nuclear fragment re-interaction in the target [42, 58].

and the forward energy:

$$nTracks > (-0.13534 \cdot E_F) + 152.9323 \tag{3.1}$$

In the equation 3.1 above, E_F is given in GeV.

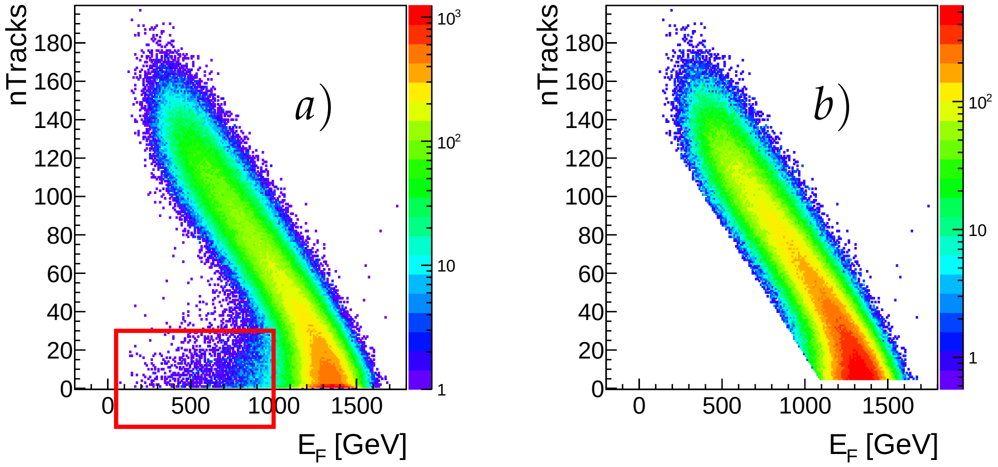

FIGURE 3.3: The distribution of track multiplicity as a function of forward energy (a) the distribution before geometric and $nTracks$ > 4 cuts and (b) after the cuts. The red rectangle in a) shows the events which do not obey the expected anti-correlation.

$nTracks > 4$ cut

Events with a very low multiplicity of charged tracks are expected to be potentially problematic for the measurement of π^+/π^- ratios. On one hand, such events will suffer from higher vertex losses and from a higher off-target background due to the worsening of the vertex reconstruction resolution with decreasing $nTracks$. On the other hand, indications for delta-electron events, with very low multiplicities, have also been found in the course of the present study.

Consequently, an additional cut on the total number of charged tracks has been applied in this analysis in order to remove such events. An event is accepted only if it has $nTracks$ greater than 4. The effect of the cut is apparent in Fig. 3.3 (b). This cut eliminates low multiplicity events from the two most peripheral collision samples from Fig. 3.3, which has been judged to be of minor importance for this specific analysis in view of the known slow dependence of electromagnetically-distorted π^+/π^- ratios on event multiplicity, or centrality [2]. The study of a remaining, potential bias on π^+/π^- measurement introduced by this cut, and the corresponding systematic uncertainty will be discussed in section 3.5. Its influence on the average characteristics of a given event sample, such as the mean impact parameter or spectator charge will be addressed below in this section.

S5 cut

The signal from S5 is crucial to define the minimum bias trigger logic as explained in section 2.3. The fact that the S5 signal is below that of beam ions is associated with the beam interacting with the target. In previous studies, this cut was set to 170 ADC units as it is described in Refs. [7] and [6], however, these analyses were done on central collisions (T2 trigger). Optimization of the cut on S5 in the present analysis is important on one hand to eradicate possible remaining events where the beam particles would pass through the target without interaction or interacting elastically (the beam peak), and on the other hand to extend the centrality range of this study.

Fig. 3.4 (a) shows the distributions of the S5 signal in T1 and T4 triggers for both target IN and target OUT data. In order to see the full S5 spectrum and the beam peak, the T1 trigger is studied. The target OUT distributions are also presented for quality assurance of the cut and for completeness. The distributions of T4 are normalised to T1 (the same normalization procedure is used as it was explained above). One can see the beam peak in the range between 350 to 450 ADC. The plateau from 0 to 330 ADC corresponds to inelastic interactions.

After a detailed study, it has been brought to light that the previously applied cut S5 < 170 ADC was unnecessarily eliminating some peripheral events. Consequently, the S5 cut has been changed to S5 < 330 ADC. As such it includes the continuous plateau of the S5 signal as shown in Fig. 3.4 (a). The distributions of the S5 signal after geometrical and $nTracks > 4$ cuts are shown in Fig. 3.4 (b). It is to be noted that as expected, no beam peak is visible in panel (b).

---

[2] The latter fact was well established experimentally in Pb+Pb collisions, where centrality selection was performed directly by multiplicity cuts [59, 29, 60]. The slow dependence on centrality is again confirmed and discussed for Ar+Sc reactions in Chapter 4.

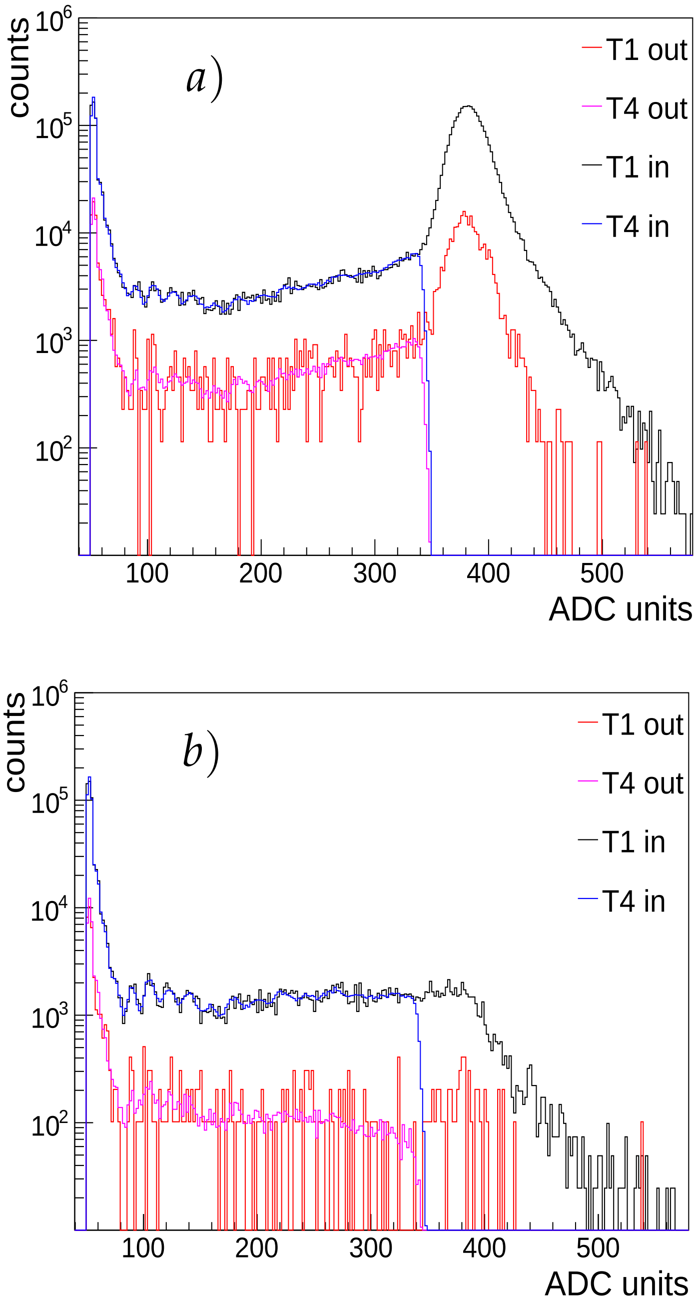

FIGURE 3.4: The distribution of S5 signal before (a) and after (b) geometrical and $nTracks > 4$ cuts. The red distribution represents the data without the target for the T1 trigger. The magenta distribution represents data without the target for the T4 trigger. The black colour represents data with the target for the T1 trigger. The distribution in blue represents data with the target for the T4 trigger.

Event statistics after cuts

Table 3.1 summarizes the event statistics in the data sample of Ar+Sc collisions at $40A$ GeV/c. The data were analyzed for two centrality selections, which we label as *thin* and *wide*. The main *thin* selection subdivided the total event sample into six sub-samples with total statistics varying from 61 to 171 thousand events; in the peripheral region, larger numbers of events were taken to make up for the lower pion multiplicity per event with respect to more central collisions. The six samples in this *thin* selection are labeled C_0, C_1, C_2, C_3, C_4 and C_5 (following the convention used earlier in Ref. [61]). Additionally, the same data was also processed and π^+/π^- ratios were obtained in a wider centrality selection in order to decrease the corresponding statistical errors. The three samples in this *wide* selection are labeled C_{0+1}, C_{2+3}, and C_{4+5}. For each selected sample, Table 3.1 includes its corresponding selection of forward energy, put together with the range of percentiles of the total inelastic Ar+Sc cross-section which corresponds to this specific E_F selection. The latter percentile ranges were obtained from an independent analysis of target IN data with target OUT subtraction [57, 62]. As evident from Table 3.1 the present analysis of spectator-induced EM effects on π^+/π^- ratios covers nearly the entire range of collision centrality in inelastic Ar+Sc reactions, with the exclusion of very peripheral events as it was mentioned above.

Class	E_F selection	Centrality percentiles (%)	Total events
C_0	$0 < E_F < 660$	0-9.5	61k
C_1	$660 < E_F < 840$	9.5-19	61k
C_2	$840 < E_F < 980$	19-28.5	60k
C_3	$980 < E_F < 1090$	28.5-39	65k
C_4	$1090 < E_F < 1260$	39-67	171k
C_5	$1260 < E_F < 1400$	67-93.5	144k
C_{0+1}	$0 < E_F < 840$	0-19	121k
C_{2+3}	$840 < E_F < 1090$	19-39	126k
C_{4+5}	$1090 < E_F < 1400$	39-93	314k

TABLE 3.1: Event statistics after cuts for the two selections in centrality (upper: *thin*, lower: *wide*). The E_F is given in GeV. Obtained centrality percentiles are rounded to 0.5%. The total number of events is rounded to full thousand.

Class	<b> [fm]	<N_W>	<QsAr>
C_0	1.94±0.18	61.9±1.7	4.2±0.4
C_1	3.32±0.06	46.5±0.6	7.6±0.1
C_2	4.23±0.10	35.0±0.6	10.2±0.1
C_3	5.04±0.17	25.2±0.9	12.4±0.2
C_4	6.34±0.26	12.9±0.8	15.2±0.2
C_5	7.78±0.44	4.9±0.1	17.0±0.5
C_{0+1}	2.62±0.12	54.4±1.1	5.8±0.2
C_{2+3}	4.65±0.15	29.9±0.8	11.4±0.2
C_{4+5}	6.91±0.33	9.8±1.4	15.9±0.3

TABLE 3.2: Estimates of the mean impact parameter <b>, average total number of wounded nucleons <N_W>, and mean Ar spectator charge <QsAr> for each centrality class.

Table 3.2 presents our tentative estimates for the average values of the impact parameter, the total number of wounded nucleons, and the Ar spectator charge. The most important parameters for the current analysis are the impact parameter and spectator charge, as these determine the strength of spectator-induced EM effects and will be used in the phenomenological studies presented in Chapter 4. The aforementioned estimates and their uncertainties have been obtained using three models:

1. A dedicated, simple geometrical "Glauber" simulation of the Ar+Sc collision with an elementary nucleon-nucleon cross section of 30.6 mb, and selection of centrality samples by the number of Ar spectator nucleons following the percentiles given in Table 3.1;
2. The event generator EPOS 1.99 (version CRMC 1.5.3) [63, 64, 65] with its implementation of the Wounded Nucleon Model [5], and selection of centrality samples by the number of Ar spectator nucleons;
3. The same version of the EPOS event generator, with centrality selection by the forward energy E_F as coming from a GEANT 4 [66] simulation of the PSD detector.

The influence of the most relevant event selection cuts used in this analysis (described earlier in this section), was approximately estimated by introducing similar cuts in the simulation. In order to approximate the cut on the low value of *nTracks*, a cut on a low number of wounded nucleons ($N_W > 2$) has been introduced for all three models. In order to evaluate the influence of the "geometrical" cut, a similar simple cut was implemented on the N_W versus E_F plane for models 2 and 3.

The values of <b>, <N_W> and <QsAr> originate from the simplest model no. 1, while the associated uncertainties are given by the differences between the three models, plus additionally, pessimistic uncertainties attributed to the simple approximation of experimental cuts addressed above. These uncertainties were estimated independently for each centrality sample in the *thin* and *wide* selections.

The approach described above ensures that the estimates of <b>, <N_W>, <QsAr> and their error bars presented in Table 3.2 are secure with respect to model dependence, conceptual uncertainties, and also the known imperfections in the present version of the PSD simulation. Generally, uncertainties in all three quantities appear larger for central and peripheral and smaller for intermediate centrality collisions. It should be underlined that these uncertainties are, in fact, moderate with respect to the needs of the simple phenomenological studies performed in the next chapter.

3.3 Track selection

This section will describe the track selection procedure on the reconstructed particle tracks.

Track topology

The tracks are classified into two categories: Right Side Tracks (RST) and Wrong Side Tracks (WST). The RST satisfies the following equation:

$$q \cdot p_x > 0 \tag{3.2}$$

where q is the electric charge and p_x is the x component of the momentum vector. For the WST the product in equation 3.2 is negative. Since the magnetic field is anti-parallel to the y-axis, the RSTs are bent in the direction of p_x, thus away from the beamline. The readout pads of TPCs are tilted with respect to the beamline to minimise the angle between the RST trajectory and the TPC pad direction in the horizontal plane $x - z$. This optimisation reduces the width of the cluster on the padrow and reduces the influence of fluctuations of ionization along the trajectory of the particle. Therefore only the RSTs are selected for the analysis.

Track status

All the particle tracks are examined for their status. From all the registered particle tracks, only those which are successfully fitted to the main vertex are selected for further analysis.

Impact point

The selection of impact point ($\vec{b} = (b_x, b_y)$) criteria applies to the distance in $x - y$ plane between the track extrapolated to the target z-plane (b_x, b_y) and the main vertex. The tracks are accepted if $|b_x| < 4$ cm and $|b_y| < 2$ cm. This condition reduces the contribution of particles originating from weak decays of neutral hadrons and increases the probability that the track was produced in the primary interaction.

Azimuthal angle (ϕ)

From Fig. 2.1, it is apparent that the NA61/SHINE detector does not possess complete azimuthal acceptance. Consequently, apart from selecting only RSTs, an additional cut on the azimuthal angle is made. The tracks with azimuthal angle ϕ within $\pm 75^\circ$ with respect to the horizontal plane are accepted in the analysis. Such a relatively wide cut (see Ref. [6] for comparison) appeared necessary in view of the limited event and track statistics available to the present study (it should be noted that the extraction of π^+/π^- ratios, section 3.4, was performed in a double differential way as a function of x_F and p_T).

Total number of measured clusters

The total number of reconstructed points (clusters) on the track should be greater than 30 to ensure a sufficient resolution of the energy loss (dE/dx) measurement.

Number of clusters measured in VTPCs

15 points in VTPC1 and VTPC2 combined are required as the minimal number of clusters. This ensures that the momentum of the track is well reconstructed since VTPC1 and VTPC2 are placed inside the magnetic field.

Particle identification (PID)

Charged pions were identified via measurement of their specific energy loss within the active volume of NA61/SHINE Time Projection Chambers.

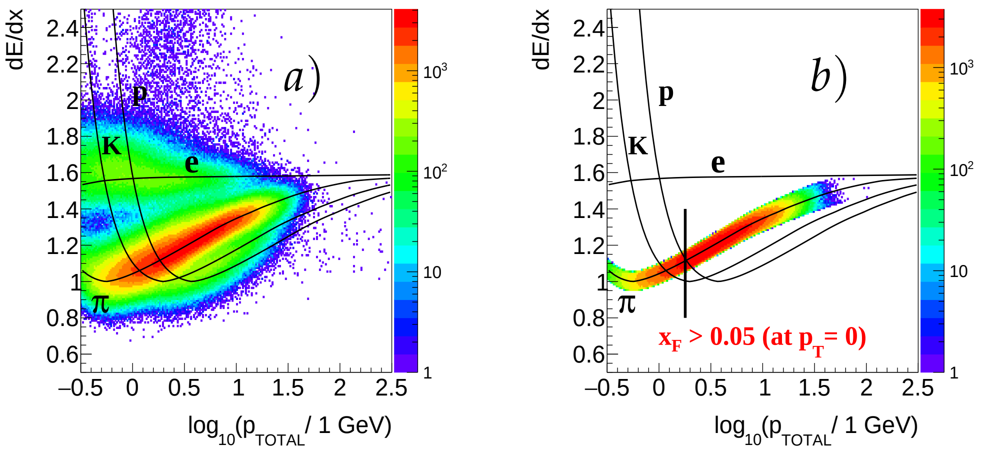

FIGURE 3.5: The distribution of truncated mean ionisation loss dE/dx as a function of total momentum for negatively charged tracks, for (a) all negative particles (b) pion candidates.

Fig. 3.5 shows the truncated mean dE/dx of charged particles as a function of their total momentum. The Fig. 3.5 (a) shows all the negative particles whereas the plot in Fig. 3.5 (b) shows the π^- candidates, selected by making a ±5% cut around the pion Bethe-Bloch function. At this beam energy, the low x_F and low p_T of the pion in the collision c.m.s. corresponds to a low laboratory momentum, close to the region of the crossing of Bethe-Bloch functions for different particles. Therefore, we anticipate a high level of contamination of selected pion candidates. As a precautionary measure, we have restricted the pion x_F range to ensure a safe range of laboratory momentum. Pion candidates were accepted for the analysis only above this value of $x_F \geq 0.05$, as depicted by the vertical black line in Fig. 3.5 (b).

3.4 Extraction of π^+/π^- ratios

In this analysis, the ratios of positive over negative pion density (π^+/π^- ratios) are obtained in centrality-selected Ar+Sc collisions as a function of pion x_F and p_T (we remind that both quantities are given in the c.m.s. of the collision). To achieve this, two-dimensional histograms of positively and negatively charged dE/dx-selected pion candidate tracks are constructed in the bins of x_F and p_T [3]. These two-dimensional histograms are subsequently sliced and divided to obtain the π^+/π^- ratio as a function of x_F for the selected p_T value.

Although other analyses performed in NA61/SHINE have typically presented results as a function of rapidity, here x_F is chosen as a longitudinal variable. This choice is imposed by a better visualization of the electromagnetic distortion of π^+/π^- ratios in x_F with respect to rapidity, in particular for fast pions were spectator-induced effects are most apparent. The second reason for this choice is that previous studies of the spectator-induced EM effects also employed x_F (see, e.g., Ref. [30]), thus it allows direct comparisons as it will be shown in Chapter 4.

3.5 Systematic uncertainties

This section discusses the various sources of systematic uncertainty inherent to this analysis. The formulation of the discussion is, to a certain degree, based on that made in earlier studies of Ar+Sc collisions [6, 7, 67]. Nonetheless, the complete evaluation of systematic errors has been tailored to the current study of π^+/π^- ratios, and thus, the description places the main emphasis on factors that are important to this analysis.

A remark should be made here. While in numerous NA61/SHINE analyses, the discussion of systematic error is made in terms of its relative value with respect to a given quantity ("in %"), here it is always discussed in absolute values. It has been decided that the latter brings better clarity for the specific case of experimentally measured π^+/π^- ratios which remain in the range 0.43-1.01 as it will become apparent in section 3.5.5.

---

[3] The overall binning scheme will be explained in section 3.5.5.

3.5.1 Event selection criteria

This section discusses the uncertainties related to possible biases induced on π^+/π^- ratios by event selection criteria.

Off-time particles ($\sigma_{off-timeparticles}$)

The level of uncertainty induced by the removal of events with off-time particles was estimated using a methodology identical to that described in Ref. [6]. Specifically, the exclusion time window was adjusted by ± 2 μs relative to its nominal value of 4 μs. The analysis revealed that the resulting uncertainties in the π^+/π^- ratio were very moderate. An upper limit of 0.01 was assumed independently on the pion x_F and p_T, and event centrality.

Trigger+*nTracks* cut bias ($\sigma_{trigger+cut}$)

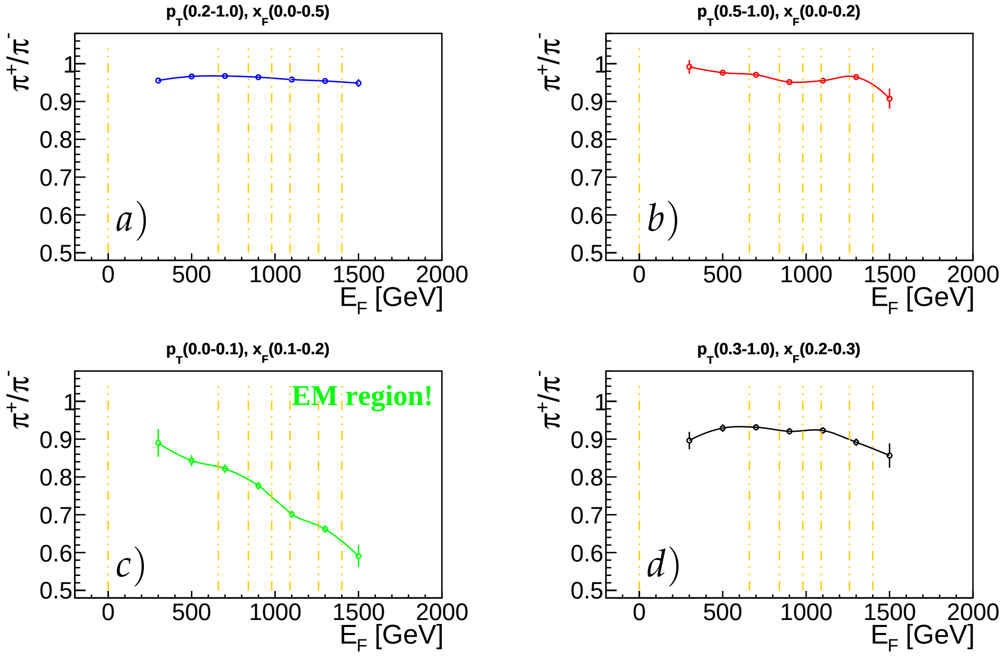

FIGURE 3.6: The π^+/π^- ratio as a function of centrality (forward energy) for four different phase space regions of x_F and p_T. The phase space regions are marked on the top of each plot. The different centrality classes are marked with vertical dotted yellow lines. The E_F range of the present analysis is 0-1400 GeV as explained in section 3.2.

The T4 trigger has been presented in section 2.3, and the event selection has been delineated in section 3.2. This particular segment of the discussion will address the uncertainties induced by both the presence of the T4 trigger and the cut on low multiplicity events, $nTracks > 4$.

The T4 minimum bias trigger is, in general, sensitive to charged particles. At the level of knowledge established in this analysis (the first in NA61/SHINE based on this trigger for Ar+Sc reactions) it can not be excluded that this sensitivity would introduce a bias on the measured π^+/π^- ratios in the most peripheral data sample.

Furthermore, the trigger event selection is reinforced by the cut on low multiplicity events $nTracks > 4$. This cut, sensitive to the number of measured charged and not neutral particles, could also in principle select specific event configurations and therefore could also result in a systematic bias with respect to an unbiased event selection.

To estimate the potential uncertainty resulting from these two issues, a relatively straightforward, data-based analysis was conducted on four distinct phase space regions as illustrated in Fig. 3.6. Three of these correspond to areas of the phase space that are not affected by the EM distortion of the π^+/π^- ratio which is studied in this thesis. Fig. 3.6 (a) corresponds to the broadest region of phase space, which encompasses the bulk of pions in the forward hemisphere with the exclusion of the low p_T region. The plot shown in Fig. 3.6 (b) corresponds to the higher p_T region, close to central rapidity, whereas the plot in Fig. 3.6 (d) corresponds to the higher x_F and higher p_T region of phase space. The region in Fig. 3.6 (c) is explicitly defined as to be sensitive to the spectator-induced EM effect. The potential uncertainty that arises from the two sources discussed above was estimated (pessimistically) on the basis of deviations from an expected roughly constant behaviour as a function of centrality, in all three areas of phase space with the absence of the spectator-induced EM effect. On this basis, it was found that the corresponding potential bias was negligible in central, but not in peripheral event samples. The corresponding uncertainty on the measured π^+/π^- ratio reaches a maximum value of 0.035 at high x_F in most peripheral Ar+Sc collisions. This decreases with decreasing x_F and increasing centrality and remains typically in the range 0-0.01.

Vertex position (σ_{vertex})

The uncertainty induced by the vertex selection has been estimated, in a way similar to Ref. [6], by varying the vertex selection along the beam direction between ±3 and ±10 cm. Consequently, the potential uncertainties have been assessed as a function of x_F, p_T, and centrality. The width of the vertex z distribution, largely defined by the charged track multiplicity, strongly depends on centrality as apparent in Fig. 3.7. Consequently, it has been determined that the uncertainties are negligible for the first three central bins of the thin selection. For the fourth bin, the uncertainty is estimated to be of the order of 0.01, whereas, for the fifth and sixth bins, it is of the order of 0.015 and 0.025, respectively.

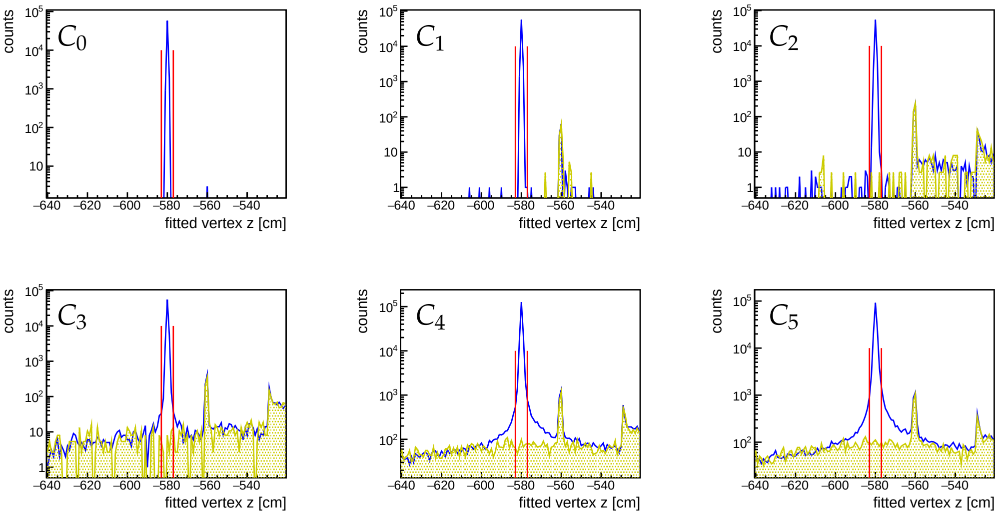

FIGURE 3.7: Primary vertex position distribution along the beam axis for six different centrality samples. The solid blue line represents target IN data and the shaded area represents scaled target OUT data. The vertical red lines correspond to the cut ± 3 cm.

3.5.2 Track selection criteria

The estimation of systematic uncertainty's contribution resulting from track selection criteria was conducted in the following manner.

The number of clusters ($\sigma_{clusters}$)

The uncertainties induced by cuts on the number of clusters were estimated in a way similar to Ref. [6]. The nominal value of 30 clusters was used as a baseline, and the minimum total number of clusters was adjusted by ±5 points. Similarly, the nominal value of 15 was used as a baseline for the minimum number of clusters in VTPCs, which was also varied by ±5 points.

The alterations in the total number of clusters observed were found insignificant for π^+/π^- ratios, except for two areas: the area with the lowest p_T at $x_F = 0.0625$, and the region with the highest p_T (500 MeV/c). In both regions, a conservative estimate of 0.01 was adopted as resulting uncertainty. The criteria applied to the number of clusters in the VTPCs appeared to have a negligible impact on the π^+/π^- ratio throughout most of the phase space. However, an important exception to the above was the region of highest x_F and lowest p_T. Here deviations of the π^+/π^- ratio appeared bigger, resulting in an estimated value of 0.03 for the corresponding uncertainty.

Azimuthal angle (σ_ϕ)

The stability of the results on the choice of azimuthal angle was tested by comparing the outcomes obtained for two different ranges (±75° and ±50°). This study has shown that the overall impact on the π^+/π^- ratio was close to negligible.

Particle identification ($\sigma_{dE/dx}$)

The particle identification method used in this thesis and explained in section 3.3 introduces uncertainties in the measured π^+/π^- ratios. There are two primary sources of these uncertainties, as outlined below.

1. The pion candidate sample, selected by the criterion of ±5% around the pion energy loss (Bethe-Bloch) function, can appear contaminated by other charged particles.

2. A possible deviation of the nominal position of the Bethe-Bloch obtained after TPC calibration from the true value of the average (truncated) energy loss would result in a different number of pion candidates entering the ±5% dE/dx cut. In the very specific case where this effect would be noticeably different for π^+ and π^- (the corresponding RSTs enter two different MTPCs), it would not cancel out in the π^+/π^- ratio and could introduce a systematic bias.

In order to estimate the potential uncertainties introduced by our particle identification method, a comparison of its results to another method was used [68]. The latter is known as the identity method; it is generally based on fitting dE/dx spectra as described in Ref. [6], thus it should be insensitive to the two specific problems enumerated above. This comparison was conducted for Ar+Sc data at 150A GeV/c and then applied, using pessimistic assumptions to 40A GeV/c. The resulting (pessimistically estimated) systematic error was found to be approximately 0.02 in most of the phase space, except for two regions: the region of high x_F and also the entire region of low p_T, where it remained between 0.03 and 0.04.

3.5.3 Reconstruction efficiency ($\sigma_{efficiency}$)

Generally, reconstruction efficiency is defined as the ratio of the number of particles reconstructed in the detector to the real number of particles emerging from the collision [4]. Efficiency can significantly depend on x_F and p_T. The lack of efficiency correction as is the case of the present analysis could in principle induce a bias in the obtained measurements.

In order to estimate this potential bias, an *a posteriori* calculation of reconstruction efficiency has been performed. Efficiency was calculated for central and peripheral Ar+Sc collisions. The process of generating particles in inelastic Ar+Sc collisions was modelled through the use of the EPOS 1.99 generator [64] while the transport of these particles through the NA61/SHINE detector was simulated using GEANT 3.21 [69]. The obtained values of efficiency were typically in the range of 80-90%. For the π^+/π^- ratio, this analysis revealed no significant influence of efficiency: this is because the computed efficiency losses for π^+ and π^- appeared very similar and therefore they cancel out in the ratio. The remaining small differences of the order of typically 0.02 have been assumed as the systematic uncertainty originating from this source. This uncertainty has a moderate dependence on x_F and p_T, reaching up a maximum value of about 0.05 at $x_F = 0.3$ and $p_T = 25$ MeV/c. Also, it has only a weak dependence on collision centrality.

3.5.4 Feed-down from weak decays ($\sigma_{feed-down}$)

A significant source of uncertainty in the π^+/π^- ratio obtained in this analysis comes from the contamination of charged pion spectra by products of weak decays. The weak days under consideration are $K^0_s \to \pi^+\pi^-$, $\Lambda \to p\pi^-$, $\bar{\Lambda} \to \bar{p}\pi^+$, $\Sigma^+ \to n\pi^+$, $\bar{\Sigma}^- \to \bar{n}\pi^-$, $\Sigma^- \to n\pi^-$, and $\bar{\Sigma}^+ \to \bar{n}\pi^+$. The

---

[4] This definition does not include particles originating from weak decays discussed in section 3.5.4.

situation is schematically explained in Fig. 3.8 where the weak decay of the Λ baryon results in the production of a p and a π^-, and the π^- is (wrongly) reconstructed to the primary interaction vertex. Generally, the contribution of such wrongly reconstructed weak decay products to measured particle yields strongly depends on x_F and p_T. This issue is of importance for the

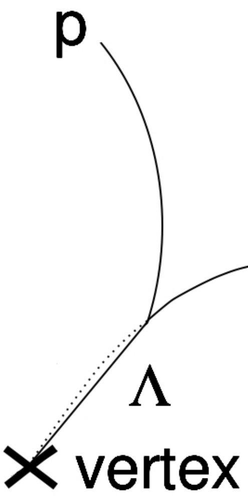

FIGURE 3.8: Example of hyperon feed-down to measured pion spectra. The picture is adapted from Ref. [55].

π^+/π^- ratios mostly because the Λ yield in Ar+Sc collisions is expected to be significantly higher than the $\bar{\Lambda}$ yield. Thus, the Λ and $\bar{\Lambda}$ contributions will not cancel out in the π^+/π^- ratio. This situation will be better for the $K^0_s \rightarrow \pi^+\pi^-$ decay as its contribution to the π^+/π^- ratio is expected to cancel out in a large part. For the present analysis, no measured yields of the weakly decaying particles were available at the moment of the analysis [5]. For that reason, no model-independent correction for weak decays could be performed and the induced uncertainty had to be carefully estimated as a function of x_F, p_T and centrality. This was made in the following way. An independent analysis [6] served to provide a basic estimate of weak decay contributions to π^+ and π^- yields in central Ar+Sc collisions. This was made on the general basis of the EPOS 1.99 model and GEANT 3.21 simulation of the NA61/SHINE detector, put together with assumptions for K^0_s and hyperon yields as deduced on the basis of experimental data on charged kaon production in Ar+Sc collisions. More details on this analysis can be

---

[5] The first result on K^0_s production in central Ar+Sc reactions emerged at the late stages of writing this thesis [70].

found in the cited reference. This was then adapted to the present analysis in order to (1) match the assumed K_s^0 yield to be consistent with the very recent data [70], and (2) take account of the variation of the contribution of strange particle decays into pions as a function of centrality. A pessimistic estimate of the change of the strangeness production as a function of centrality was assumed, with the smallest strangeness suppression factor of 0.885 assumed for most peripheral Ar+Sc collisions with respect to the most central collisions. The corresponding contributions to π^+ and π^- were then translated into π^+/π^- ratios, and the resulting total uncertainty induced by weak decays has been calculated. This uncertainty appeared to be strongly dependent on x_F, p_T and weaker on centrality. This strong dependence on x_F and p_T is mostly imposed by the contribution of Λ baryon and its decay into π^-. The estimated uncertainty takes a maximum value of 0.13 for the lowest x_F and the lowest p_T for central Ar+Sc collisions. It somewhat decreases when going to peripheral collisions, and goes down to about 0.01 for high x_F and higher values of p_T.

3.5.5 Total systematic errors and numerical data

The total systematic errors from the different sources have been added up in quadrature:

$$\sigma_{total} = (\sigma^2_{off-time} + \sigma^2_{trigger+cut} + \sigma^2_{vertex} + \sigma^2_{nClusters} + \sigma^2_{\phi} + \\ \sigma^2_{dE/dx} + \sigma^2_{efficiency} + \sigma^2_{feed-down})^{1/2} \quad (3.3)$$

The resulting error is, in general, asymmetric. This is imposed by the uncertainty related to feed-down from weak decays, which in turn results mostly from the contribution of the $\Lambda \rightarrow p\pi^-$ decay to the measured π^+/π^- ratios.

Numerical values of the π^+/π^- ratios obtained for the different centrality samples of Ar+Sc collisions as a function of pion x_F and p_T in the collision c.m.s. are presented in Tables 3.3 to 3.11, together with corresponding statistical and systematic errors.

Phase space binning scheme

The values of pion x_F and p_T given in Tables 3.3 - 3.11 correspond to the center of the bin. The specified range for p_T delineates between 25 and 500

MeV/c. The x_F varied from 0.0625 to 0.3, with the exception of the highest p_T value of 500 MeV/c where it varied between 0.05 and 0.3. The bin width was generally equal to 0.05 for all x_F values, albeit with a unique deviation at 0.0625 where it was reduced to 0.025. In terms of p_T, the bin width was set at 50 MeV/c, except for the 500 MeV/c point, where it was expanded to 100 MeV/c.

p_T [MeV/c]	x_F	π^+/π^-	±stat	+sys	-sys
25	0.0625	0.760	±0.019	+0.135	-0.042
	0.1000	0.764	±0.020	+0.115	-0.035
	0.1500	0.812	±0.033	+0.071	-0.035
	0.2000	0.900	±0.053	+0.053	-0.045
	0.2500	0.901	±0.070	+0.045	-0.044
	0.3000	0.979	±0.101	+0.059	-0.058
75	0.0625	0.817	±0.012	+0.107	-0.028
	0.1000	0.808	±0.013	+0.078	-0.026
	0.1500	0.834	±0.019	+0.055	-0.026
	0.2000	0.921	±0.030	+0.038	-0.033
	0.2500	0.961	±0.043	+0.027	-0.027
	0.3000	0.856	±0.050	+0.036	-0.036
125	0.0625	0.858	±0.011	+0.069	-0.026
	0.1000	0.857	±0.011	+0.049	-0.024
	0.1500	0.918	±0.018	+0.038	-0.024
	0.2000	0.906	±0.024	+0.027	-0.027
	0.2500	0.950	±0.033	+0.027	-0.027
	0.3000	0.954	±0.043	+0.037	-0.037
175	0.0625	0.890	±0.013	+0.040	-0.026
	0.1000	0.902	±0.011	+0.035	-0.024
	0.1500	0.882	±0.015	+0.029	-0.024
	0.2000	0.903	±0.021	+0.024	-0.024
	0.2500	0.950	±0.031	+0.032	-0.031
	0.3000	0.930	±0.038	+0.037	-0.037
225	0.0625	0.926	±0.014	+0.037	-0.031
	0.1000	0.914	±0.012	+0.027	-0.024
	0.1500	0.935	±0.016	+0.025	-0.024
	0.2000	0.926	±0.022	+0.024	-0.024
	0.2500	0.916	±0.028	+0.027	-0.027
	0.3000	0.957	±0.038	+0.033	-0.033
500	0.0500	1.004	±0.015	+0.032	-0.032
	0.1000	0.985	±0.016	+0.038	-0.038
	0.1500	0.945	±0.018	+0.031	-0.031
	0.2000	0.943	±0.022	+0.026	-0.026
	0.2500	0.902	±0.025	+0.028	-0.028
	0.3000	0.933	±0.030	+0.034	-0.034

TABLE 3.3: The numerical values of π^+/π^- ratios in Ar+Sc collisions at 40A GeV/c together with their statistical and systematic errors. The results are shown for the centrality sample C_0, which corresponds to the range $0 < E_F < 660$ GeV.

p_T [MeV/c]	x_F	π^+/π^-	±stat	+sys	-sys
25	0.0625	0.747	±0.021	+0.129	-0.042
	0.1000	0.815	±0.024	+0.126	-0.035
	0.1500	0.651	±0.029	+0.054	-0.035
	0.2000	0.804	±0.049	+0.050	-0.045
	0.2500	0.978	±0.078	+0.050	-0.047
	0.3000	1.006	±0.107	+0.062	-0.061
75	0.0625	0.830	±0.014	+0.107	-0.028
	0.1000	0.827	±0.014	+0.080	-0.026
	0.1500	0.826	±0.021	+0.054	-0.026
	0.2000	0.860	±0.030	+0.036	-0.033
	0.2500	0.874	±0.041	+0.027	-0.027
	0.3000	0.817	±0.050	+0.036	-0.036
125	0.0625	0.853	±0.013	+0.067	-0.026
	0.1000	0.875	±0.012	+0.05	-0.024
	0.1500	0.833	±0.017	+0.033	-0.024
	0.2000	0.892	±0.025	+0.027	-0.027
	0.2500	0.875	±0.033	+0.027	-0.027
	0.3000	1.002	±0.049	+0.037	-0.037
175	0.0625	0.913	±0.015	+0.042	-0.027
	0.1000	0.893	±0.012	+0.034	-0.024
	0.1500	0.866	±0.017	+0.029	-0.024
	0.2000	0.900	±0.023	+0.024	-0.024
	0.2500	0.848	±0.029	+0.029	-0.029
	0.3000	0.901	±0.039	+0.036	-0.036
225	0.0625	0.924	±0.016	+0.038	-0.032
	0.1000	0.905	±0.013	+0.026	-0.024
	0.1500	0.986	±0.019	+0.026	-0.024
	0.2000	0.903	±0.023	+0.024	-0.024
	0.2500	0.911	±0.030	+0.027	-0.027
	0.3000	0.894	±0.038	+0.033	-0.033
500	0.0500	0.975	±0.017	+0.031	-0.030
	0.1000	0.960	±0.018	+0.038	-0.038
	0.1500	0.926	±0.020	+0.030	-0.030
	0.2000	0.907	±0.023	+0.026	-0.026
	0.2500	0.915	±0.028	+0.028	-0.028
	0.3000	0.931	±0.034	+0.034	-0.034

TABLE 3.4: The numerical values of π^+/π^- ratios in Ar+Sc collisions at 40A GeV/c together with their statistical and systematic errors. The results are shown for the centrality sample C_1, which corresponds to the range $660 < E_F < 840$ GeV.

p_T [MeV/c]	x_F	π^+/π^-	±stat	+sys	-sys
25	0.0625	0.764	±0.024	+0.129	-0.042
	0.1000	0.741	±0.024	+0.106	-0.035
	0.1500	0.608	±0.029	+0.050	-0.035
	0.2000	0.717	±0.050	+0.048	-0.045
	0.2500	0.805	±0.070	+0.046	-0.045
	0.3000	0.902	±0.099	+0.060	-0.060
75	0.0625	0.806	±0.015	+0.099	-0.028
	0.1000	0.848	±0.016	+0.082	-0.026
	0.1500	0.791	±0.022	+0.05	-0.026
	0.2000	0.822	±0.031	+0.035	-0.033
	0.2500	0.924	±0.046	+0.028	-0.028
	0.3000	0.944	±0.060	+0.037	-0.037
125	0.0625	0.876	±0.015	+0.069	-0.027
	0.1000	0.886	±0.014	+0.050	-0.024
	0.1500	0.854	±0.019	+0.034	-0.024
	0.2000	0.895	±0.027	+0.027	-0.027
	0.2500	0.890	±0.035	+0.028	-0.028
	0.3000	0.900	±0.047	+0.036	-0.036
175	0.0625	0.878	±0.016	+0.039	-0.027
	0.1000	0.878	±0.013	+0.033	-0.024
	0.1500	0.864	±0.018	+0.028	-0.024
	0.2000	0.882	±0.025	+0.024	-0.024
	0.2500	0.852	±0.031	+0.027	-0.027
	0.3000	0.914	±0.043	+0.035	-0.035
225	0.0625	0.976	±0.019	+0.041	-0.034
	0.1000	0.899	±0.015	+0.026	-0.024
	0.1500	0.914	±0.019	+0.025	-0.024
	0.2000	0.896	±0.025	+0.024	-0.024
	0.2500	0.926	±0.034	+0.027	-0.027
	0.3000	0.848	±0.041	+0.033	-0.033
500	0.0500	0.995	±0.019	+0.030	-0.029
	0.1000	0.968	±0.021	+0.038	-0.038
	0.1500	0.920	±0.023	+0.029	-0.029
	0.2000	0.902	±0.026	+0.026	-0.026
	0.2500	0.922	±0.032	+0.028	-0.028
	0.3000	0.881	±0.036	+0.034	-0.034

TABLE 3.5: The numerical values of π^+/π^- ratios in Ar+Sc collisions at 40A GeV/c together with their statistical and systematic errors. The results are shown for the centrality sample C_2, which corresponds to the range $840 < E_F < 980$ GeV.

p_T [MeV/c]	x_F	π^+/π^-	±stat	+sys	-sys
25	0.0625	0.745	±0.027	+0.122	-0.043
	0.1000	0.695	±0.025	+0.096	-0.037
	0.1500	0.472	±0.026	+0.041	-0.037
	0.2000	0.632	±0.048	+0.048	-0.047
	0.2500	0.804	±0.075	+0.049	-0.048
	0.3000	0.835	±0.097	+0.061	-0.060
75	0.0625	0.812	±0.017	+0.099	-0.03
	0.1000	0.777	±0.016	+0.070	-0.029
	0.1500	0.755	±0.023	+0.047	-0.028
	0.2000	0.809	±0.033	+0.037	-0.035
	0.2500	0.887	±0.047	+0.031	-0.031
	0.3000	0.812	±0.057	+0.037	-0.037
125	0.0625	0.857	±0.017	+0.066	-0.030
	0.1000	0.864	±0.015	+0.048	-0.026
	0.1500	0.851	±0.021	+0.035	-0.026
	0.2000	0.885	±0.029	+0.029	-0.029
	0.2500	0.872	±0.037	+0.031	-0.031
	0.3000	0.855	±0.048	+0.038	-0.038
175	0.0625	0.915	±0.019	+0.043	-0.031
	0.1000	0.913	±0.016	+0.036	-0.027
	0.1500	0.858	±0.020	+0.030	-0.026
	0.2000	0.825	±0.025	+0.026	-0.026
	0.2500	0.864	±0.034	+0.029	-0.029
	0.3000	0.872	±0.045	+0.036	-0.036
225	0.0625	0.935	±0.020	+0.041	-0.036
	0.1000	0.934	±0.017	+0.029	-0.027
	0.1500	0.924	±0.022	+0.027	-0.027
	0.2000	0.886	±0.028	+0.027	-0.027
	0.2500	0.821	±0.033	+0.029	-0.029
	0.3000	0.890	±0.046	+0.035	-0.035
500	0.0500	0.972	±0.021	+0.030	-0.030
	0.1000	0.968	±0.023	+0.040	-0.040
	0.1500	0.951	±0.027	+0.030	-0.030
	0.2000	0.886	±0.029	+0.028	-0.028
	0.2500	0.949	±0.036	+0.031	-0.031
	0.3000	0.879	±0.040	+0.036	-0.036

TABLE 3.6: The numerical values of π^+/π^- ratios in Ar+Sc collisions at 40A GeV/c together with their statistical and systematic errors. The results are shown for the centrality sample C_3, which corresponds to the range $980 < E_F < 1090$ GeV.

p_T [MeV/c]	x_F	π^+/π^-	±stat	+sys	-sys
25	0.0625	0.784	±0.023	+0.129	-0.046
	0.1000	0.740	±0.021	+0.102	-0.040
	0.1500	0.463	±0.021	+0.043	-0.039
	0.2000	0.538	±0.032	+0.050	-0.050
	0.2500	0.638	±0.047	+0.049	-0.049
	0.3000	0.683	±0.062	+0.060	-0.060
75	0.0625	0.856	±0.015	+0.106	-0.034
	0.1000	0.793	±0.013	+0.072	-0.032
	0.1500	0.711	±0.017	+0.046	-0.032
	0.2000	0.759	±0.024	+0.040	-0.039
	0.2500	0.774	±0.032	+0.036	-0.036
	0.3000	0.726	±0.038	+0.041	-0.041
125	0.0625	0.853	±0.013	+0.066	-0.034
	0.1000	0.858	±0.012	+0.049	-0.030
	0.1500	0.834	±0.016	+0.037	-0.030
	0.2000	0.804	±0.020	+0.034	-0.034
	0.2500	0.812	±0.027	+0.036	-0.036
	0.3000	0.824	±0.035	+0.041	-0.041
175	0.0625	0.917	±0.015	+0.046	-0.035
	0.1000	0.908	±0.012	+0.038	-0.030
	0.1500	0.878	±0.016	+0.034	-0.030
	0.2000	0.860	±0.021	+0.032	-0.032
	0.2500	0.831	±0.025	+0.034	-0.034
	0.3000	0.801	±0.033	+0.039	-0.039
225	0.0625	0.929	±0.016	+0.044	-0.040
	0.1000	0.914	±0.014	+0.032	-0.030
	0.1500	0.886	±0.017	+0.030	-0.030
	0.2000	0.918	±0.023	+0.032	-0.032
	0.2500	0.872	±0.028	+0.034	-0.034
	0.3000	0.947	±0.039	+0.039	-0.039
500	0.0500	0.981	±0.018	+0.033	-0.033
	0.1000	0.946	±0.018	+0.042	-0.042
	0.1500	0.928	±0.021	+0.032	-0.032
	0.2000	0.915	±0.024	+0.034	-0.034
	0.2500	0.923	±0.029	+0.036	-0.036
	0.3000	0.953	±0.035	+0.040	-0.040

TABLE 3.7: The numerical values of π^+/π^- ratios in Ar+Sc collisions at 40A GeV/c together with their statistical and systematic errors. The results are shown for the centrality sample C_4, which corresponds to the range $1090 < E_F < 1260$ GeV.

p_T [MeV/c]	x_F	π^+/π^-	±stat	+sys	-sys
25	0.0625	0.790	±0.033	+0.129	-0.051
	0.1000	0.691	±0.029	+0.094	-0.046
	0.1500	0.426	±0.027	+0.047	-0.045
	0.2000	0.486	±0.041	+0.062	-0.062
	0.2500	0.598	±0.058	+0.062	-0.062
	0.3000	0.706	±0.086	+0.072	-0.072
75	0.0625	0.824	±0.021	+0.099	-0.041
	0.1000	0.773	±0.018	+0.072	-0.039
	0.1500	0.714	±0.024	+0.051	-0.039
	0.2000	0.690	±0.030	+0.054	-0.054
	0.2500	0.871	±0.047	+0.053	-0.053
	0.3000	0.721	±0.050	+0.055	-0.055
125	0.0625	0.911	±0.021	+0.076	-0.042
	0.1000	0.886	±0.018	+0.055	-0.038
	0.1500	0.815	±0.022	+0.042	-0.038
	0.2000	0.810	±0.028	+0.050	-0.050
	0.2500	0.859	±0.038	+0.053	-0.053
	0.3000	0.878	±0.048	+0.056	-0.056
175	0.0625	0.890	±0.021	+0.05	-0.042
	0.1000	0.880	±0.017	+0.043	-0.038
	0.1500	0.899	±0.024	+0.041	-0.038
	0.2000	0.857	±0.028	+0.049	-0.049
	0.2500	0.853	±0.037	+0.051	-0.051
	0.3000	0.933	±0.050	+0.054	-0.054
225	0.0625	0.974	±0.025	+0.052	-0.048
	0.1000	0.929	±0.020	+0.039	-0.038
	0.1500	0.908	±0.025	+0.038	-0.038
	0.2000	0.912	±0.032	+0.049	-0.049
	0.2500	0.835	±0.038	+0.050	-0.050
	0.3000	0.958	±0.055	+0.054	-0.054
500	0.0500	0.932	±0.024	+0.039	-0.039
	0.1000	0.967	±0.027	+0.048	-0.048
	0.1500	1.007	±0.033	+0.039	-0.039
	0.2000	0.873	±0.034	+0.050	-0.050
	0.2500	0.914	±0.041	+0.052	-0.052
	0.3000	0.918	±0.048	+0.055	-0.055

TABLE 3.8: The numerical values of π^+/π^- ratios in Ar+Sc collisions at 40A GeV/c together with their statistical and systematic errors. The results are shown for the centrality sample C_5, which corresponds to the range $1260 < E_F < 1400$ GeV.

p_T [MeV/c]	x_F	π^+/π^-	±stat	+sys	-sys
25	0.0625	0.754	±0.014	+0.132	-0.042
	0.1000	0.787	±0.015	+0.120	-0.035
	0.1500	0.733	±0.022	+0.063	-0.035
	0.2000	0.852	±0.036	+0.052	-0.045
	0.2500	0.937	±0.052	+0.047	-0.045
	0.3000	0.992	±0.073	+0.060	-0.059
75	0.0625	0.823	±0.009	+0.107	-0.028
	0.1000	0.817	±0.009	+0.079	-0.026
	0.1500	0.830	±0.014	+0.054	-0.026
	0.2000	0.892	±0.021	+0.037	-0.033
	0.2500	0.918	±0.030	+0.027	-0.027
	0.3000	0.837	±0.036	+0.036	-0.036
125	0.0625	0.856	±0.009	+0.068	-0.026
	0.1000	0.865	±0.008	+0.049	-0.024
	0.1500	0.877	±0.012	+0.036	-0.024
	0.2000	0.899	±0.017	+0.027	-0.027
	0.2500	0.915	±0.023	+0.027	-0.027
	0.3000	0.977	±0.032	+0.037	-0.037
175	0.0625	0.900	±0.010	+0.041	-0.026
	0.1000	0.898	±0.008	+0.034	-0.024
	0.1500	0.875	±0.011	+0.029	-0.024
	0.2000	0.902	±0.016	+0.024	-0.024
	0.2500	0.900	±0.021	+0.030	-0.030
	0.3000	0.917	±0.027	+0.036	-0.036
225	0.0625	0.925	±0.011	+0.037	-0.031
	0.1000	0.910	±0.009	+0.027	-0.024
	0.1500	0.957	±0.012	+0.026	-0.024
	0.2000	0.916	±0.016	+0.024	-0.024
	0.2500	0.914	±0.021	+0.027	-0.027
	0.3000	0.927	±0.027	+0.033	-0.033
500	0.0500	0.991	±0.011	+0.031	-0.031
	0.1000	0.974	±0.012	+0.038	-0.038
	0.1500	0.937	±0.014	+0.030	-0.030
	0.2000	0.927	±0.016	+0.026	-0.026
	0.2500	0.908	±0.019	+0.028	-0.028
	0.3000	0.932	±0.023	+0.034	-0.034

TABLE 3.9: The numerical values of π^+/π^- ratios in Ar+Sc collisions at 40A GeV/c together with their statistical and systematic errors. The results are shown for the centrality sample C_{0+1}, which corresponds to the range $0 < E_F < 840$ GeV.

p_T [MeV/c]	x_F	π^+/π^-	±stat	+sys	-sys
25	0.0625	0.756	±0.018	+0.126	-0.042
	0.1000	0.720	±0.017	+0.101	-0.036
	0.1500	0.544	±0.020	+0.045	-0.035
	0.2000	0.677	±0.035	+0.048	-0.046
	0.2500	0.804	±0.051	+0.047	-0.046
	0.3000	0.870	±0.069	+0.060	-0.060
75	0.0625	0.809	±0.012	+0.099	-0.029
	0.1000	0.816	±0.011	+0.075	-0.027
	0.1500	0.774	±0.016	+0.048	-0.027
	0.2000	0.816	±0.023	+0.036	-0.033
	0.2500	0.907	±0.033	+0.029	-0.029
	0.3000	0.881	±0.042	+0.037	-0.037
125	0.0625	0.867	±0.011	+0.067	-0.028
	0.1000	0.876	±0.010	+0.049	-0.025
	0.1500	0.852	±0.014	+0.034	-0.025
	0.2000	0.891	±0.020	+0.027	-0.027
	0.2500	0.881	±0.026	+0.029	-0.029
	0.3000	0.878	±0.033	+0.037	-0.037
175	0.0625	0.894	±0.012	+0.041	-0.028
	0.1000	0.894	±0.010	+0.034	-0.025
	0.1500	0.861	±0.013	+0.029	-0.025
	0.2000	0.855	±0.018	+0.025	-0.025
	0.2500	0.858	±0.023	+0.027	-0.027
	0.3000	0.895	±0.031	+0.035	-0.035
225	0.0625	0.958	±0.014	+0.041	-0.035
	0.1000	0.914	±0.011	+0.027	-0.025
	0.1500	0.919	±0.015	+0.025	-0.025
	0.2000	0.892	±0.019	+0.025	-0.025
	0.2500	0.877	±0.024	+0.027	-0.027
	0.3000	0.867	±0.031	+0.033	-0.033
500	0.0500	0.985	±0.014	+0.030	-0.029
	0.1000	0.968	±0.015	+0.038	-0.038
	0.1500	0.933	±0.018	+0.029	-0.029
	0.2000	0.895	±0.020	+0.027	-0.027
	0.2500	0.934	±0.024	+0.029	-0.029
	0.3000	0.880	±0.027	+0.035	-0.035

TABLE 3.10: The numerical values of π^+/π^- ratios in Ar+Sc collisions at 40A GeV/c together with their statistical and systematic errors. The results are shown for the centrality sample C_{2+3}, which corresponds to the range $840 < E_F < 1090$ GeV.

p_T [MeV/c]	x_F	π^+/π^-	±stat	+sys	-sys
25	0.0625	0.786	±0.019	+0.129	-0.048
	0.1000	0.724	±0.017	+0.099	-0.042
	0.1500	0.450	±0.016	+0.045	-0.042
	0.2000	0.520	±0.026	+0.055	-0.055
	0.2500	0.623	±0.037	+0.055	-0.055
	0.3000	0.691	±0.050	+0.065	-0.065
75	0.0625	0.845	±0.012	+0.104	-0.037
	0.1000	0.786	±0.011	+0.072	-0.035
	0.1500	0.712	±0.014	+0.048	-0.035
	0.2000	0.734	±0.019	+0.046	-0.046
	0.2500	0.808	±0.026	+0.043	-0.043
	0.3000	0.724	±0.030	+0.047	-0.047
125	0.0625	0.872	±0.011	+0.069	-0.038
	0.1000	0.867	±0.010	+0.051	-0.034
	0.1500	0.827	±0.013	+0.039	-0.034
	0.2000	0.806	±0.016	+0.041	-0.041
	0.2500	0.829	±0.022	+0.044	-0.044
	0.3000	0.844	±0.028	+0.048	-0.048
175	0.0625	0.908	±0.012	+0.048	-0.038
	0.1000	0.898	±0.010	+0.040	-0.034
	0.1500	0.885	±0.013	+0.037	-0.034
	0.2000	0.859	±0.017	+0.040	-0.040
	0.2500	0.838	±0.021	+0.042	-0.042
	0.3000	0.848	±0.028	+0.046	-0.046
225	0.0625	0.944	±0.014	+0.048	-0.044
	0.1000	0.919	±0.011	+0.035	-0.034
	0.1500	0.893	±0.014	+0.034	-0.034
	0.2000	0.916	±0.019	+0.040	-0.040
	0.2500	0.860	±0.022	+0.042	-0.042
	0.3000	0.950	±0.032	+0.046	-0.046
500	0.0500	0.964	±0.014	+0.036	-0.036
	0.1000	0.953	±0.015	+0.044	-0.044
	0.1500	0.952	±0.018	+0.036	-0.036
	0.2000	0.902	±0.020	+0.041	-0.041
	0.2500	0.920	±0.024	+0.043	-0.043
	0.3000	0.942	±0.028	+0.047	-0.047

TABLE 3.11: The numerical values of π^+/π^- ratios in Ar+Sc collisions at 40A GeV/c together with their statistical and systematic errors. The results are shown for the centrality sample C_{4+5}, which corresponds to the range 1090 < E_F < 1400 GeV.

Chapter 4

Results and Discussion

This chapter presents the results of this analysis. It puts the main emphasis on the main characteristics of the spectator-induced EM effect on the charged pion (π^+/π^-) ratio, namely:

- its distribution over phase space, that is, as a function of x_F and p_T;
- its centrality dependence, connected to the magnitude of spectator charge;
- the interplay between the EM effect and other effects present in the collision (most of all on isospin effects on fast pion production as discussed in section 4.1 below).

The discussion of results on Ar+Sc reactions obtained in this thesis will be followed by a comparison with earlier results on peripheral Pb+Pb collisions at 158A GeV/c beam momentum, obtained by the NA49 collaboration [30].

Subsequently, a comparison between the results obtained in this analysis and a Monte Carlo model simulation applied by the author based on the earlier works of A. Szczurek and A. Rybicki [22, 71] will be presented. The Monte Carlo approach used in this part of this study is similar to the one applied in the phenomenological works on Pb+Pb collisions cited above.

Finally, an attempt will be made to draw conclusions on the space-time evolution of the process of pion production in the Ar+Sc collision. This will be put in the more general context of similar studies on heavy ion reactions.

Data presentation

In all the figures presented in this Chapter, error bars on the experimental data points will be only statistical (systematic errors have been presented in Tables 3.3 - 3.11 in the previous Chapter 3). Unless explicitly specified, the curves drawn through the data points will serve only to guide the eye.

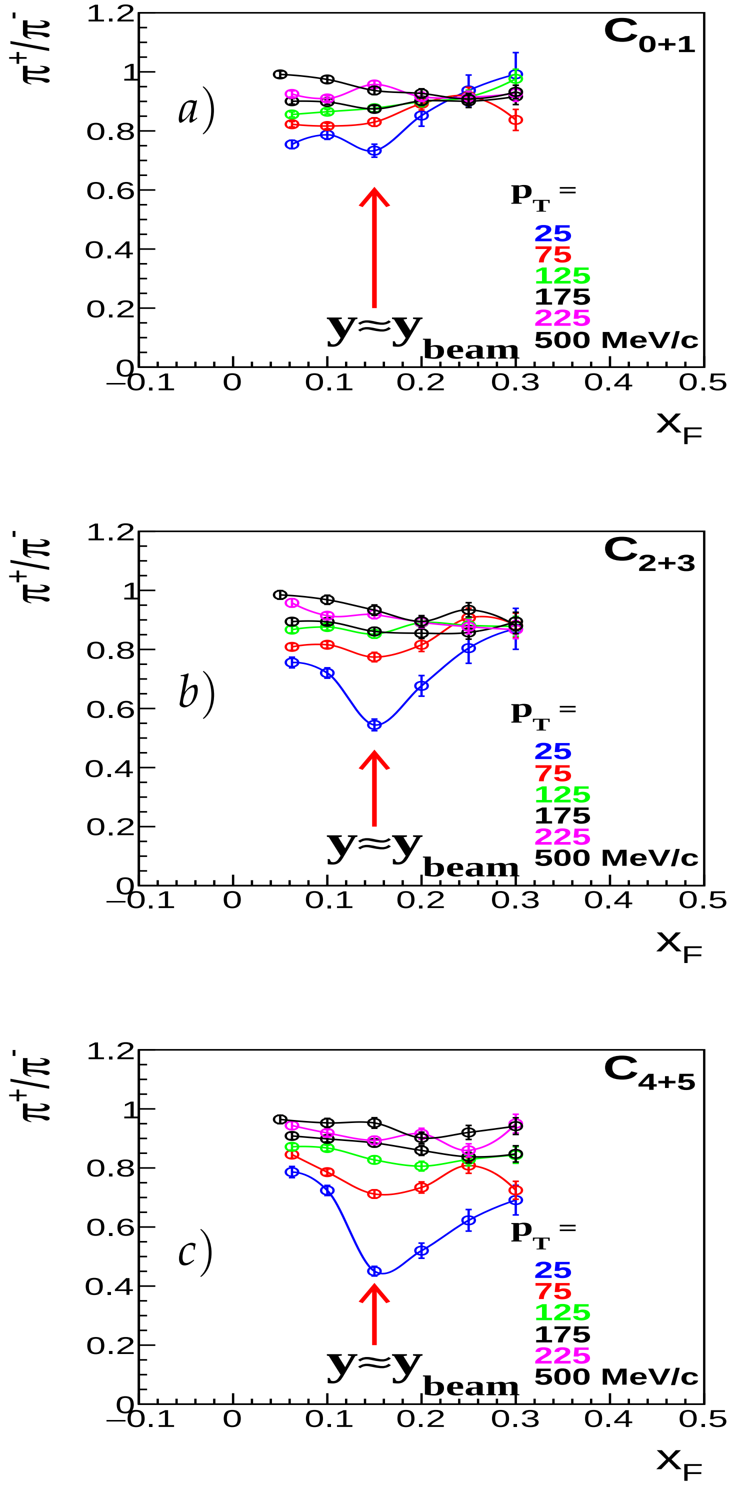

FIGURE 4.1: The π^+/π^- ratio in three different centrality selected samples of Ar+Sc collisions: central (C_{0+1}), intermediate (C_{2+3}), and peripheral (C_{4+5}). The red arrow gives the value of pion x_F which, at low transverse momentum, corresponds to beam rapidity.

4.1 π^+/π^- ratios in Ar+Sc reactions as a function of centrality

Fig. 4.1 shows the π^+/π^- ratio plotted as a function of x_F for six different values of pion transverse momentum p_T, both variables x_F and p_T being given in the collision c.m. system. The three panels of the figure correspond to three *wide* selections of Ar+Sc centrality: central (C_{0+1}), intermediate (C_{2+3}), and peripheral (C_{4+5}).

A suppression of the π^+/π^- ratio is clearly visible at low transverse momentum (p_T = 25 MeV/c) of the pion. For each of the three considered data samples, this ratio appears to reach a minimum at $x_F = 0.15$. The centrality dependence of this suppression is further visualized in Fig. 4.2. Evidently, the depletion of π^+/π^- ratios becomes increasingly important when going from central to peripheral Ar+Sc reactions.

It should be noted that at low p_T, the value $x_F = 0.15 = m_\pi/m_p$ corresponds to pions moving longitudinally at the same velocity (rapidity) as the beam nucleus. This is indicated by the vertical red arrows in the plots of Fig. 4.1. Thus, the largest depletion of the charged pion ratio is seen for pions moving at *velocities similar to that of the spectator system*.

4.1.1 The origin of the effect

The suppression of the π^+/π^- ratio presented in the previous section is a result of the electromagnetic (EM) interaction between the spectator system and the charged pions produced in the collision. In the spectator reference frame, this effect can be understood as the electrostatic attraction of negative pions and electrostatic repulsion of positive pions, which results in the decrease of the π^+/π^- ratio in the region of phase space close to the spectator system [22]. The increase of this effect (decrease of the ratio) from central to peripheral collisions is the result of the corresponding increase of spectator charge.

The results presented in Figs. 4.1 and 4.2 are not only the first observation of the spectator-induced EM effect in Ar+Sc reactions at 40A GeV/c, but they are also the first ever observation of this effect in peripheral collisions of small nuclear systems at the CERN SPS.

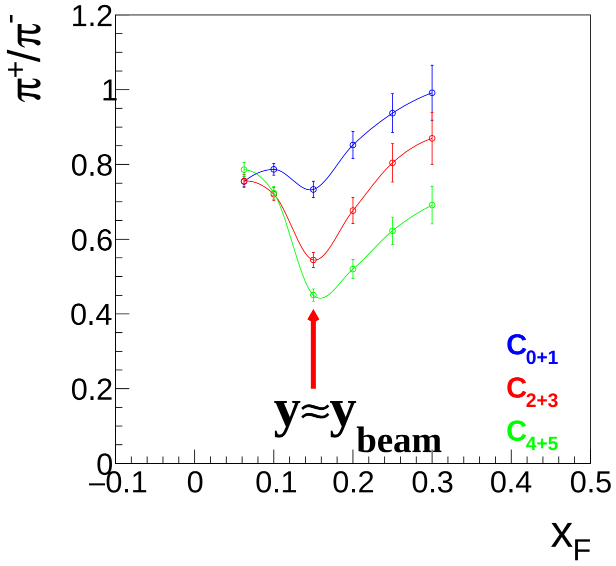

FIGURE 4.2: The π^+/π^- ratio for $p_T = 25$ MeV/c in three different centrality selected samples (the corresponding data points and curves are the same as shown in Fig. 4.1).

4.1.2 Discussion

In the context of the depletion of π^+/π^- ratios discussed above, it is interesting to consider the possible magnitude of these ratios in case they would be induced by the pure strong interaction, with no electromagnetic effect. Here a comment should be made about "isospin effects" (following the specific nomenclature used in Refs. [72, 29]), which will be important for the discussion made in various sections of the present chapter. This subject was discussed at length in the cited references; only some basic aspects will be reminded here.

An important feature of the strong interaction at high energies is that generally, it preserves isospin symmetry. As a consequence, at higher values of Feynman-x ($x_F > 0.1$) where the properties of particle production are dominated by the projectile [73], the final state yields of π^+ and π^- should "switch" when changing the projectile from a proton to a neutron. Such behaviour has indeed been confirmed experimentally for p+p and n+p collisions, and corresponding predictions for central Pb+Pb reactions have also been confirmed by experimental data [72, 29]. As a consequence, it can be argued that in the absence of electromagnetic interactions, the π^+/π^- ratio for fast ($x_F > 0.1$) pions produced in Ar+Sc collisions should not be lower than the ratio of wounded protons over wounded neutrons from the projectile nucleus.

In the case of the Ar+Sc reaction considered in this thesis, the argon projectile contains 18 protons and 22 neutrons, thus the corresponding lower limit is about 0.82. The values of the π^+/π^- ratio shown in Fig. 4.2 are significantly below this value, which confirms the electromagnetic origin of the observed effect.

4.1.3 The experimental results in six samples of centrality

It is interesting to note that a "trace" of spectator-induced EM effects is suggested by the experimental data on central Ar+Sc collisions (the C_{0+1} sample), where the spectator charge is small as it was estimated in Chapter 3, Table 3.2. This is apparent in the tiny minimum in the π^+/π^- ratio at $x_F = 0.15$ at low pion transverse momentum, see Fig. 4.1 (a) and Fig. 4.2. The corresponding depletion of positive over negative pion ratio is in fact comparable to systematic errors (section 3.5). Notwithstanding, the need appeared for a further experimental analysis which would allow for:

- a consistency check of the present results (ultimately, the spectator-induced EM effect is expected to disappear for very central collisions);
- a more "granular" study of the centrality dependence of EM effects.

For these reasons, the new analysis was performed in six centrality bins instead of three. Thus, all the centrality samples have been divided into two. This gave the *thin* selection discussed in detail in Chapter 3. The results are presented in Fig. 4.3. In spite of higher statistical fluctuations, a clear picture of the centrality dependence of the EM effect becomes available. No depletion of the π^+/π^- ratio at beam rapidity is seen for the most central collision sample (C_0 corresponding to 0-9.5% of the total cross-section), but the EM effect is apparent already in semi-central Ar+Sc collisions (C_1 corresponding to 9.5-19% of the total cross-section).

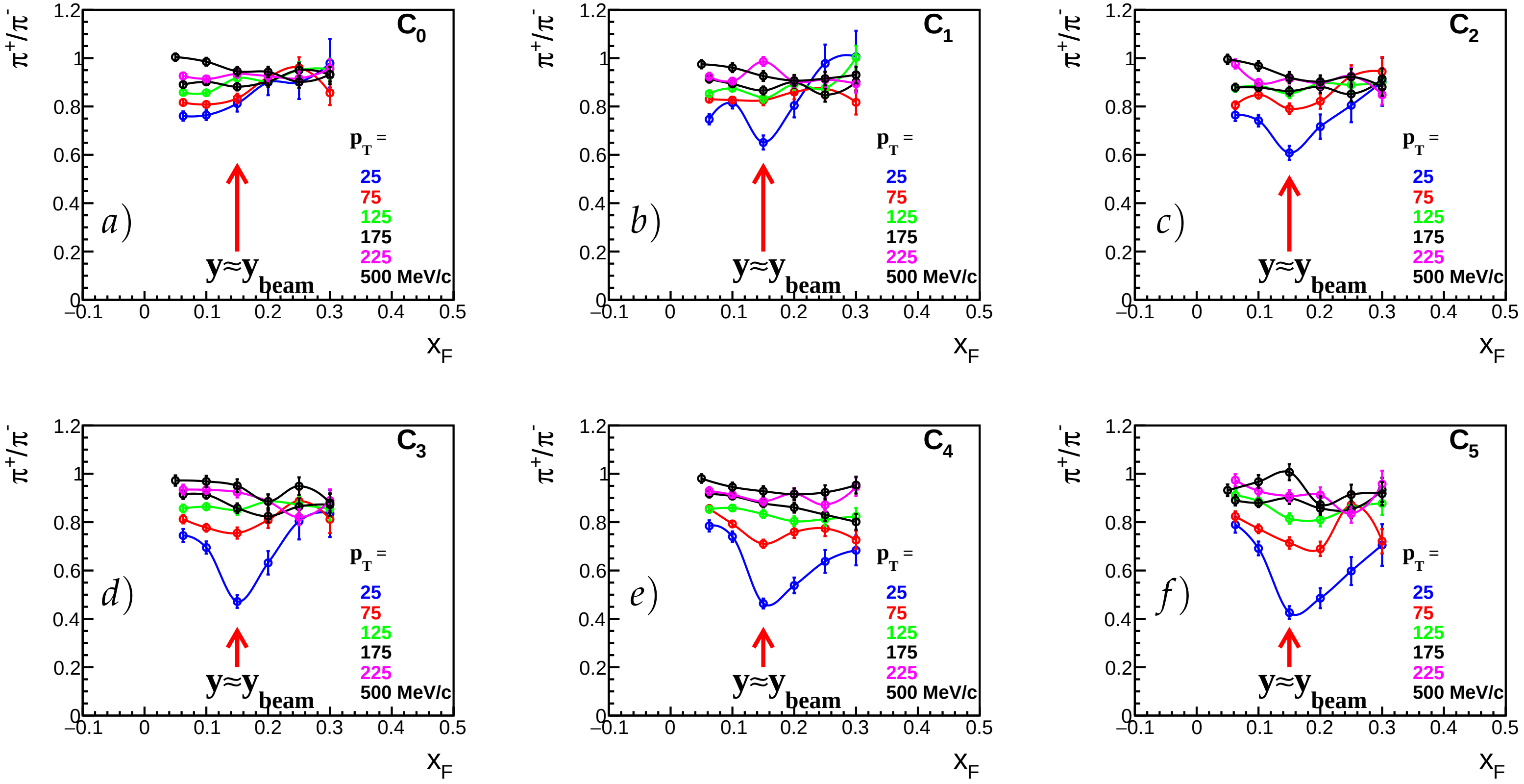

FIGURE 4.3: The π^+/π^- ratio in six different centrality selected samples of Ar+Sc collisions at $40A$ GeV/c, ranging from central (C_0) to peripheral (C_5). The red arrow gives the value of pion x_F which, at low transverse momentum, corresponds to beam rapidity.

4.2 Comparison between Ar+Sc and Pb+Pb reactions

In Fig. 4.4, the information brought by the new results on Ar+Sc collisions obtained in this thesis is compared with the existing data on Pb+Pb reactions. These data come from the Ref. [29] and have been obtained by the NA49 experiment at 158A GeV/c. The data sample corresponds to an average number of about 54 wounded nucleons and a mean impact parameter (b) of 10.9 fm. There is a qualitative similarity in the EM distortion of the π^+/π^- ratio as a function of x_F and p_T in peripheral Ar+Sc and in peripheral Pb+Pb reactions.

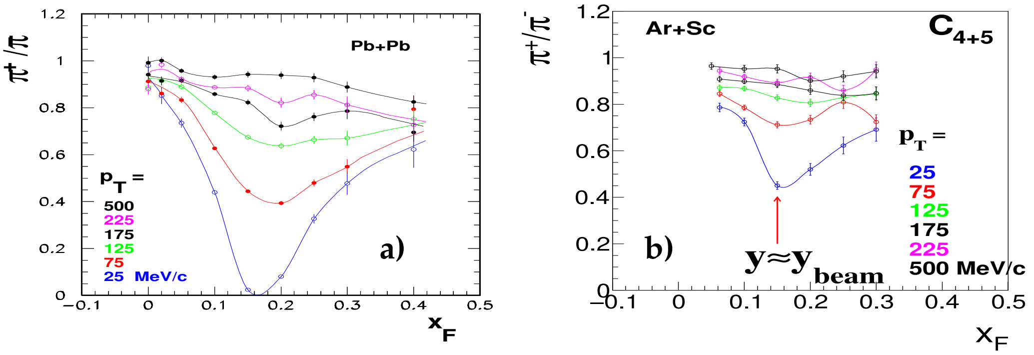

FIGURE 4.4: The π^+/π^- ratio as a function of x_F, for different values of p_T in (a) peripheral sample of Pb+Pb collisions at 158A GeV/c and (b) peripheral sample of Ar+Sc collisions at 40A GeV/c. Please note that panel (c) of Fig. 4.1 has been redrawn here in order to facilitate the comparison addressed in the text.

In peripheral Pb+Pb collisions, due to the EM effects the π^+/π^- ratio is suppressed close to zero, as shown in Fig. 4.4 (a). This effect we still observe in a much smaller system, with a much smaller spectator charge (Table 3.2), in case of Ar+Sc collisions as shown in Fig. 4.4 (b). In peripheral Ar+Sc collisions, the effect is half of the effect seen in peripheral Pb+Pb collisions.

The following observations can be made here on the basis of Fig. 4.4 :

1. The experimental data on peripheral Pb+Pb reactions have been discussed in detail in Refs. [29, 30, 27], in particular, in the context of spectator-induced EM, isospin effects and the interplay between them. Following two observations can be made from Fig. 4.4 (a):

  - isospin effects are visible in the values of the π^+/π^- ratio at higher values of p_T. At these higher values of p_T, the π^+/π^- ratio should not be much affected by the EM effects (see section 4.3 for comparison). Also from the Ref. [72], it has been shown that for isospin asymmetric nuclei (with an excess of neutrons over protons) the π^+/π^- ratio should decrease as a function of x_F. This is indeed the case, as apparent in Fig. 4.4 (a).
  - as soon as one goes down to lower values of p_T, the EM effect starts to dominate over the isospin effect inducing a very large decrease of the π^+/π^- ratio.

  Consequently, it is to be expected that also in Ar+Sc collisions, a qualitatively similar interplay of spectator-induced EM effects and isospin effects will take place.

2. In Ar+Sc reactions, the situation is more complicated than it was for peripheral Pb+Pb collisions. Following two observations can be made from Fig. 4.4 (b):

  - for higher values of p_T, one can recognize an overall similar behaviour as seen in the Pb+Pb collisions but the quantitative decrease of the π^+/π^- ratio as a function of x_F is smaller. This can be understood by the much smaller relative excess of neutrons over protons in the Ar nucleus [1].
  - for lower values of p_T ($\leq$125 MeV/c), there is no such clear "dominance" of EM effect, but rather it is a "concurrence" with respect to isospin and possibly other effects on π^+/π^- ratios. Thus, for instance, the inclusion of isospin effects will be necessary for modelling of the spectator-induced EM effect on the π^+/π^- ratios in Ar+Sc collisions. This issue will be discussed in more detail in the next section.

In the case of Ar+Sc collisions, the spectator charge varies from four to about 17 elementary units, whereas in peripheral Pb+Pb collisions, the spectator charge is much larger (of the order of 70 units). We will now put together our detailed inspection of Ar+Sc and Pb+Pb collisions in the context

---

[1] The $^{208}_{82}$Pb nucleus contains 60% neutrons over 40% protons while the $^{40}_{18}$Ar nucleus contains 55% neutrons over 45% protons.

of the evolution of the spectator-induced EM effect as a function of centrality and system size: a) in both reactions, the qualitative evolution of the EM effect is similar as a function of x_F and p_T, b) as the spectator charge increases in small systems shown in Fig. 4.3 we observe a gradual increase of the EM effect, c) for the larger heavy-ion system, a further quantitative increase of the EM effect is visible, by about a factor of two.

It is interesting to comment on the relatively slow dependence of the observed EM effect on the total magnitude of spectator charge. It will be addressed in the section 4.3, the quantitative relation between the latter charge and the EM distortion of π^+/π^- ratios is sensitive to the space-time evolution of the system, see also Ref. [27]. However, one should also point at the relatively simple issue of the pure geometry of the collision, namely the fact that the smaller system of Ar+Sc collisions corresponds also to smaller transverse distances as compared to the Pb+Pb reactions. Similarly, the higher centrality of Ar+Sc collisions corresponds to even smaller transverse distances in the system. Account taken of the simple electrostatic rule ($V \sim \frac{q}{r}$, where V is the electrostatic potential induced by the charge q at distance r), this decrease in the geometrical transverse dimensions of the system would partially counteract the decrease of the spectator charge.

What has been presented in sections 4.1 and 4.2 proves the presence of spectator-induced EM effects in Ar+Sc collisions, the persistence of these effects with decreasing spectator charge, and their overall qualitative similarity between Ar+Sc and Pb+Pb reactions.

As a final comment to this section we note that for most central Ar+Sc collisions shown in Fig. 4.3, there is no trace of spectator-induced EM effects but some asymmetry for positive over negative pions is apparent closer to mid-rapidity ($x_F = 0.0625$). Account taken of the large systematic errors in this region of phase-space, one should keep caution in the interpretation of this observation. However, we note that in this region one expects an influence of participant charge. A measurement of such an effect exists from the NA44 experiment [74]. This effect could be quite persistent over centrality as it has been pointed out that it may affect low x_F π^+/π^- ratios even in peripheral Pb+Pb reactions [27].

4.3 Comparison between experimental data and model simulations

The aim of the study presented in this section was to obtain a description of the spectator-induced electromagnetic effect using a Monte Carlo model simulation. Its two specific aims were:

- To investigate whether the relatively simple approach used earlier in Refs. [22, 71] and somewhat extended for the present analysis is sufficient to provide a reasonable description of experimental data;
- If possible, draw conclusions on the space-time evolution of the pion production process as a function of centrality.

The simulation was performed on the basis of a model which was published by A. Szczurek and A. Rybicki (for more information see Refs. [22, 71]). This model was meant to be used as a tool to understand the basic characteristics and implications of spectator-induced electromagnetic effects. In a way, the model used in this thesis is an upgraded version of the work by A. Szczurek and A. Rybicki. The only (and necessary) addition done for this work is that the expansion of the spectator charge is considered. In the two cited papers the spectator system was assumed to be stable, which is known not to be true in view of the nuclear fragmentation process. The need to include the latter expansion in studies of EM effects has been demonstrated in the analysis by Ozvenchuk et al. in Ref. [27].

4.3.1 The model

The model used in the present work is based on the following simple picture [2]. A non-central collision is assumed with a given impact parameter b as shown in the left plot of Fig. 4.5. The participant system evolves until it gives birth to final state pions. Spectator charges follow their initial trajectories with essentially unmodified velocities. The pion (π^+ and π^-) trajectories are modified by the EM interaction with the charged spectator systems. This picture is modelled in the following simplified way:

---

[2] The description made in this section is largely based on Ref. [22].

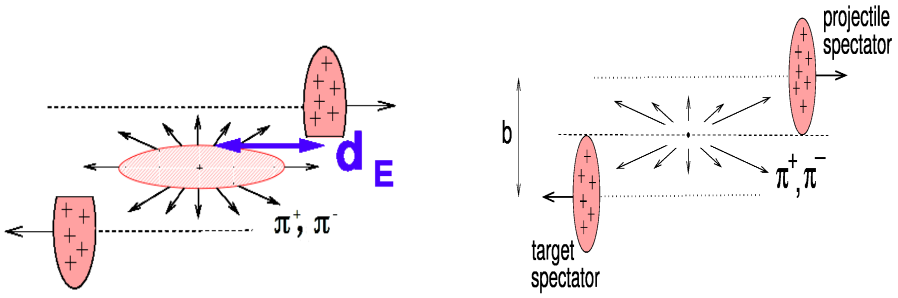

FIGURE 4.5: Left: Simplified picture of the non-central Ar+Sc collision at $40A$ GeV/c. d_E marks the longitudinal distance between the emission point of a given pion and the center of the spectator system. Right: Schematic view of the model used in this thesis. Both plots are adapted respectively from Ref. [26] and Ref. [29].

1. Initially, two Lorentz-contracted spheres with standard nuclear density $\rho = 0.17/\mathrm{fm}^3$ are assumed to collide. The initial geometry of this collision is obtained in the following way, firstly, the value of the impact parameter and spectator charge that corresponds to the experimental centrality selection (Table 3.2) is taken. Secondly, an additional displacement of the spheres in order to match the centers of gravity of the two spectator systems is also calculated on the basis of a simple Glauber simulation [3]. Thus the two spheres collide at a "technical" impact parameter which is obtained from the equation $b' = b + \Delta b_{projectile} + \Delta b_{target}$, and which best describes the transverse distance between the two spectator systems (see also the Ref. [22]).

2. The final state pion emission takes place from the hypothetical interaction point after a given emission time, t_{delay}. As such, the pion emission region is reduced to a single point in space, similarly to what was done in Ref. [22] and Ref. [71]. One emission time is assumed for a given centrality class; t_{delay} is a free parameter in this model. It is to be noted that t_{delay} in this particular model corresponds to the longitudinal distance d_E between the pion formation zone and the spectator system, see description made in section 1.6. In the present model, the two quantities are bound by the relation $t_{delay} = \beta_{spectator} \cdot d_E$ (all three quantities are

---

[3] Same simulation as described in section 3.2.

defined in collision c.m.s.) [4].

3. The initial (before the action of the EM field) two-dimensional (x_F, p_T) distribution of the emitted pions is assumed similar to that in nucleon-nucleon collisions. It is constructed as a two-dimensional analytical parametrization obtained on the basis of NA61/SHINE experimental p+p data at $40A$ GeV/c [75], account taken of isospin symmetry and of the proton/neutron content of the nucleus [5].

4. The spectator spheres expand radially with surface velocity β. This velocity, defined in spectator c.m.s. is also a free parameter of the model.

5. After the emission following their initial spectra, the charged pions are numerically traced in the EM field of the spectator systems. The additional influence of participant charge, as well as the strong final state interactions, are ignored.

4.3.2 Sensitivity to initial conditions

This section will discuss the sensitivity of the π^+/π^- ratios predicted by the model to the *initial conditions* that the model assumes for the pions emission. Following the naming used in the paper Ref. [22] by A. Szczurek and A. Rybicki, these "initial conditions" should be understood as all the conditions (free parameters) set up in the model, before the action of the EM field. In the practical case discussed here, this implies sensitivity to the two free parameters: the expansion surface velocity β assumed for the spectator sphere, and the pion emission time t_{delay}.

Fig. 4.6 (a) shows the result of the simulation for two different values of β. One can see the sensitivity of the π^+/π^- ratio in the final state to the actual value of β is highest at low p_T in the vicinity of x_F = 0.15-0.25. Account taken that the plot shows the effect of a rather small change in β (0.05), one can conclude that there is a reasonably high sensitivity of the modelled EM effect to the expansion of the spectator system. It is also evident from Fig. 4.6 (b), that the relatively small change in t_{delay} by less than 1 fm/c (or equivalently in the distance between the pion formation zone and the spectator system

---

[4] It is to be remarked that account taken that the spectator velocity is very close to the speed of light, the numerical value of d_E in fm is nearly identical to the numerical value of t_{delay} in fm/c.

[5] Parametrization obtained by Ł. Rozpłochowski, see Ref. [76] for more details.

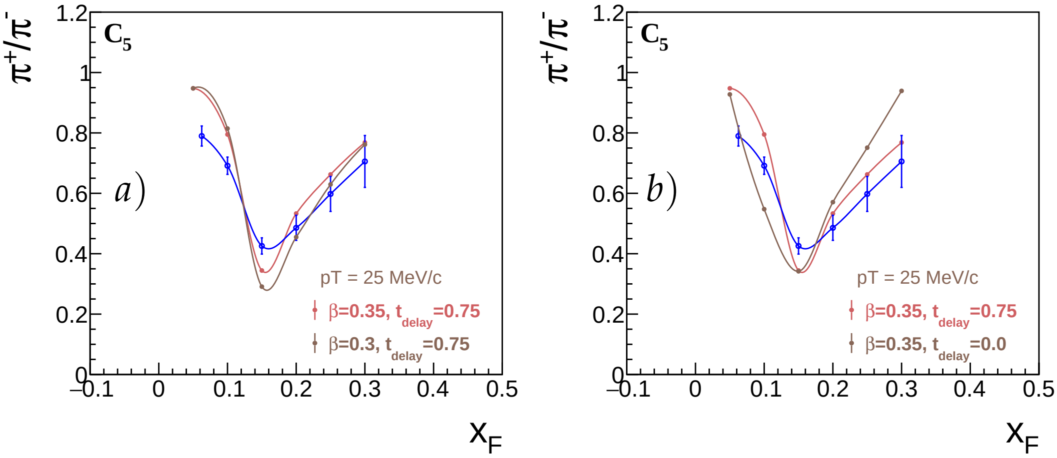

FIGURE 4.6: The Monte Carlo simulation results for the π^+/π^- ratio as a function of x_F for the most peripheral sample C_5. The selected initial conditions are indicated in the right bottom corners of each panel. t_{delay} is given in fm/c. The black dots mark the experimental data.

by less than 1 fm) already significantly changes the overall shape of the EM distortion of charged pion ratios in the final state of the Ar+Sc reaction.

The results presented in Fig. 4.6 are another illustration of the sensitivity of the spectator-induced EM distortion of the π^+/π^- ratios to the space-time evolution of the particle production process and that of the spectator system. These important features of the spectator-induced EM effect have been established before, for the case of heavy ion (Pb+Pb) reactions respectively in 2007 [22] and in 2020 [27]. In that respect, the study presented here was a repetition, for the Ar+Sc reaction case, of what has been shown earlier for Pb+Pb collisions.

In practice, quite similar to studies made in Refs. [29, 26] the phenomenological work made in this chapter will require finding the optimal values of t_{delay} and β, in order to best describe the experimental data at a given sample of centrality.

4.3.3 Results of comparative study

This section contains the comparison between the Ar+Sc experimental data and the model simulation described in sections 4.3.1 and 4.3.2 above. The work performed followed essentially the approach taken in Ref. [26] which consisted in isolating the sets of initial conditions for pion production which provided the most satisfactory description of experimental Pb+Pb data. However, the present study will in principle be much more detailed, as it will follow the entire centrality dependence of Ar+Sc collisions. Notwithstanding, the quantitative results of this analysis are to be regarded with caution, in particular, due to the overall simplicity of the original approach described in section 4.3.1. This issue will be further elaborated upon in section 4.3.4.

The Figs. 4.7 - 4.12 show the results of the simulations with the values of β and t_{delay} adjusted in the way to provide the best possible description of experimental results. When centrality shifts from central to peripheral the adjusted values of β decrease from 0.6 to 0.35 and at the same time the pion emission time t_{delay} increases from 0 to 0.75 fm$/c$.

In the first place, it can be said that the model used in this study reproduces the main characteristics of the experimental data. This specifically concerns:

1. the basic dependence of π^+/π^- ratios as a function of x_F and p_T,
2. the overall increase of the EM distortion (lowering of π^+/π^- ratios at lower transverse momenta) as a function of increasing peripherality of the collision, which corresponds to increasing the total electric charge of the spectator system,
3. the position in (x_F, p_T) of the minimum in the π^+/π^- ratio.

However, on top of this reasonable general description of the experimental data by the model, some deficiencies are also visible. These are the following.

- Even account taken the data has large systematic uncertainties in this region of phase space, the model remains systematically above the data at low p_T ($<$ 150MeV$/c$) and low x_F (≈ 0.0625).
- There is also some discrepancy between data and model at higher values of p_T ($>$ 150 MeV$/c$): the π^+/π^- ratios in the data seem lower than in the model. This discrepancy seems to become more apparent with the increasing peripherality of the collision.

Both issues will be addressed in detail in section 4.3.4 below.

As it was mentioned above, this study consisted in adjusting values of d_E and β in such a way as to get an optimal description of the experimental data.

Centrality class	Centrality percentiles (%)	d_E [fm]	β
C_0	0-9.5	0.0	0.6
C_1	9.5-19	0.25	0.55
C_2	19-28.5	0.25	0.5
C_3	28.5-39	0.5	0.4
C_4	39-67	0.75	0.4
C_5	67-93.5	0.75	0.35

TABLE 4.1: The summary of parameters for the simulation adjusted in order to provide an optimal description of the data as described in the text. The centrality percentiles are taken from Table 3.1.

As mentioned in section 4.3.1, the value of t_{delay} is equivalent to the value of the distance between the pion formation zone and the spectator system, d_E. As a result, a summary of the obtained values of d_E and β is given in Table 4.1. The slow trend of decrease in d_E as one moves from peripheral to central collisions, and of the corresponding increase in the value of β is clearly apparent in the table.

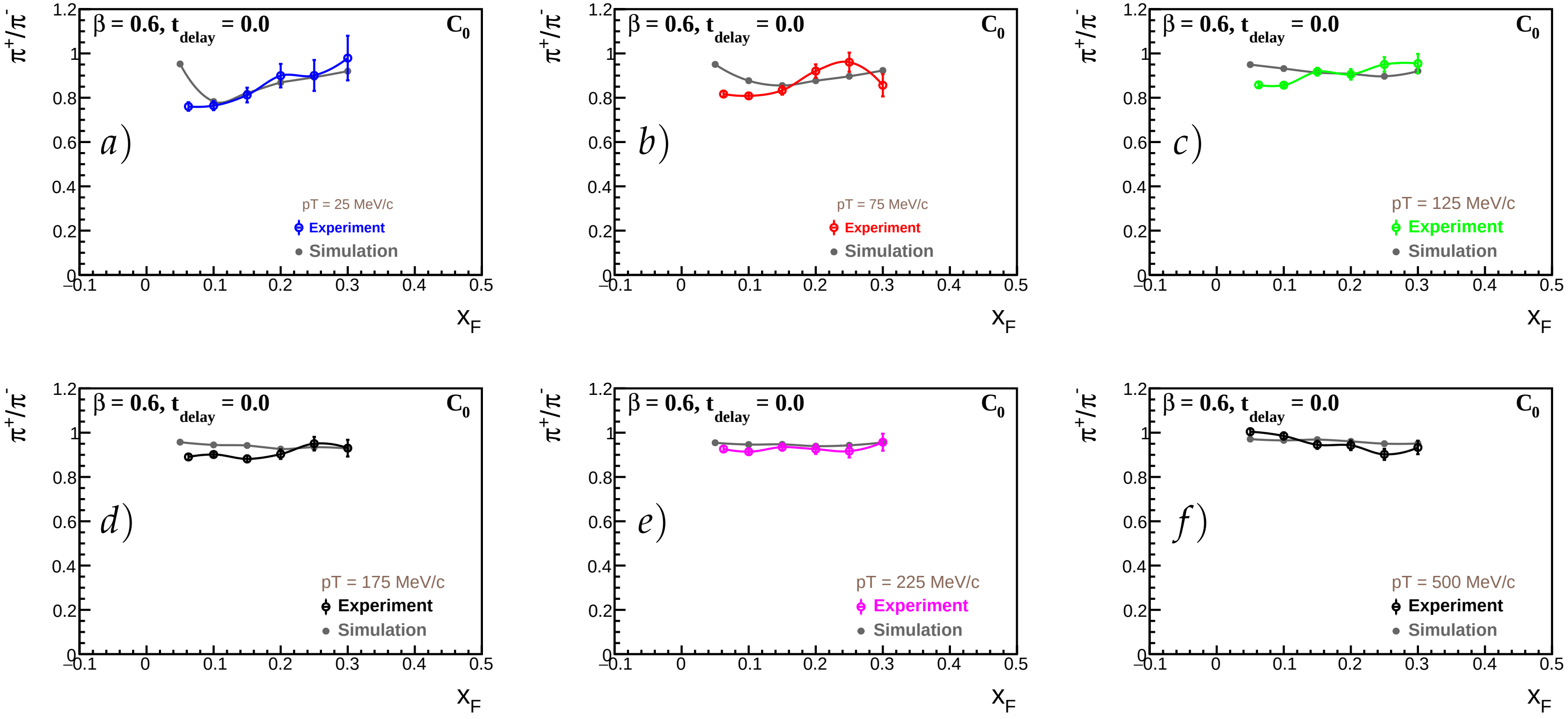

FIGURE 4.7: The Monte Carlo simulation results in π^+/π^- ratio as a function of x_F for the centrality sample C_0. The selected free parameters of the model are indicated in the left upper corner of each panel.

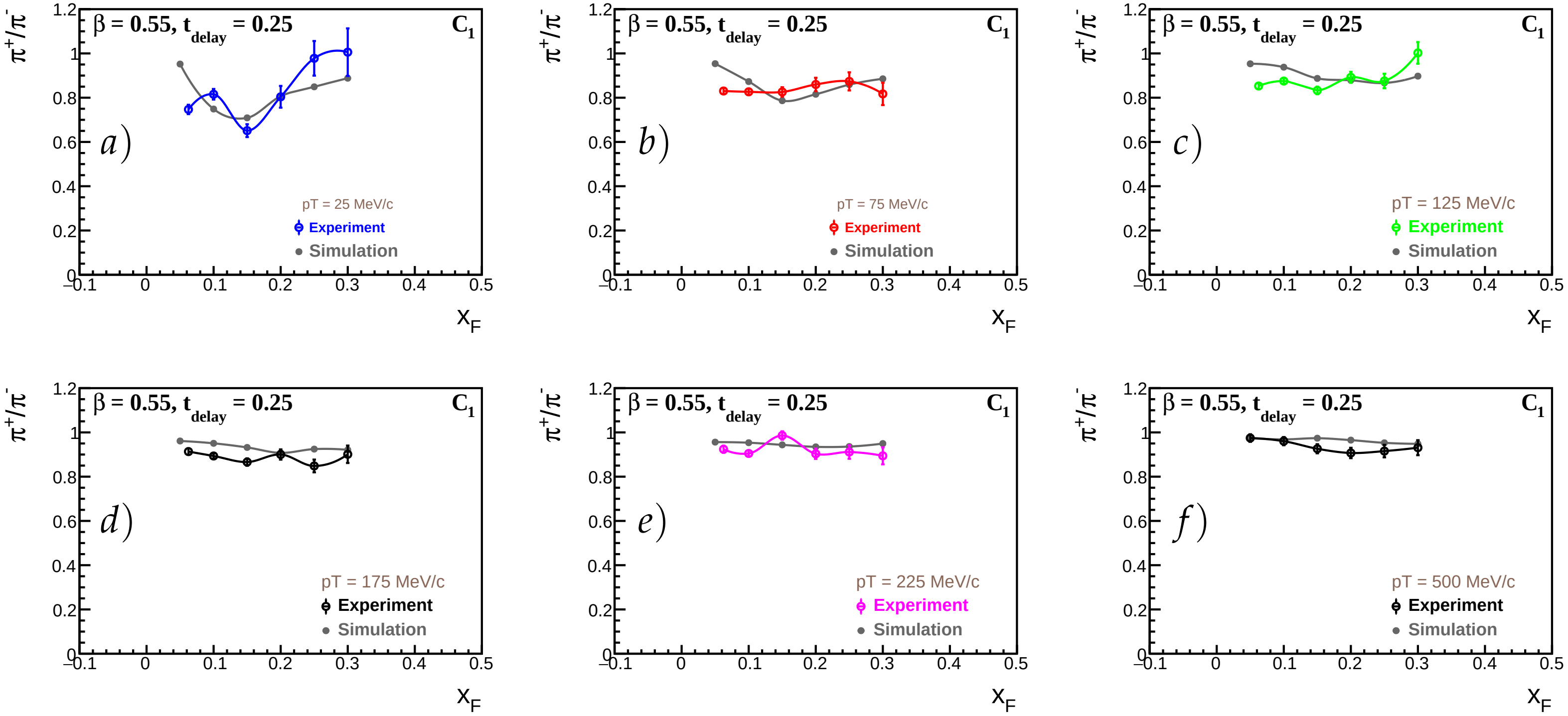

FIGURE 4.8: The Monte Carlo simulation results in π^+/π^- ratio as a function of x_F for the centrality sample C_1. The selected free parameters of the model are indicated in the left upper corner of each panel.

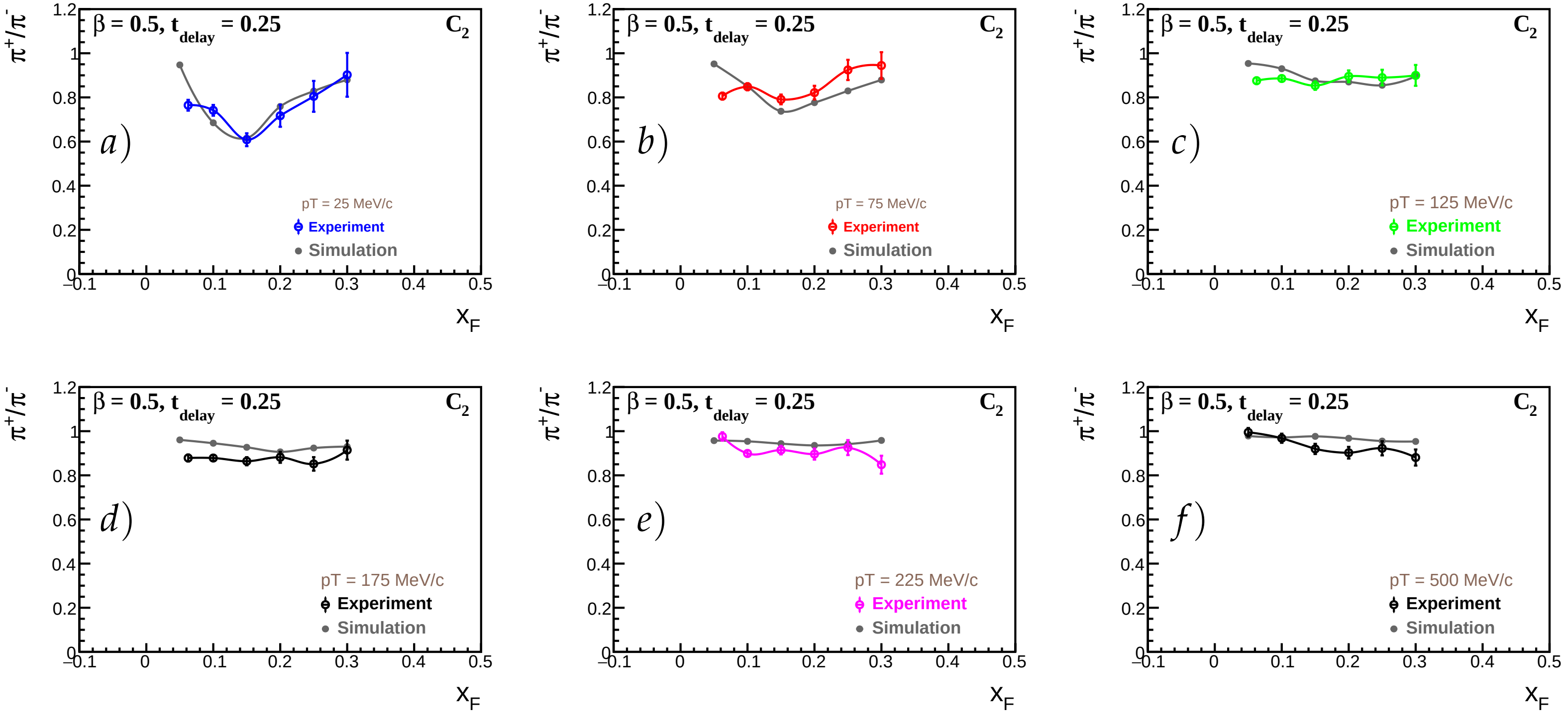

FIGURE 4.9: The Monte Carlo simulation results in π^+/π^- ratio as a function of x_F for the centrality sample C_2. The selected free parameters of the model are indicated in the left upper corner of each panel.

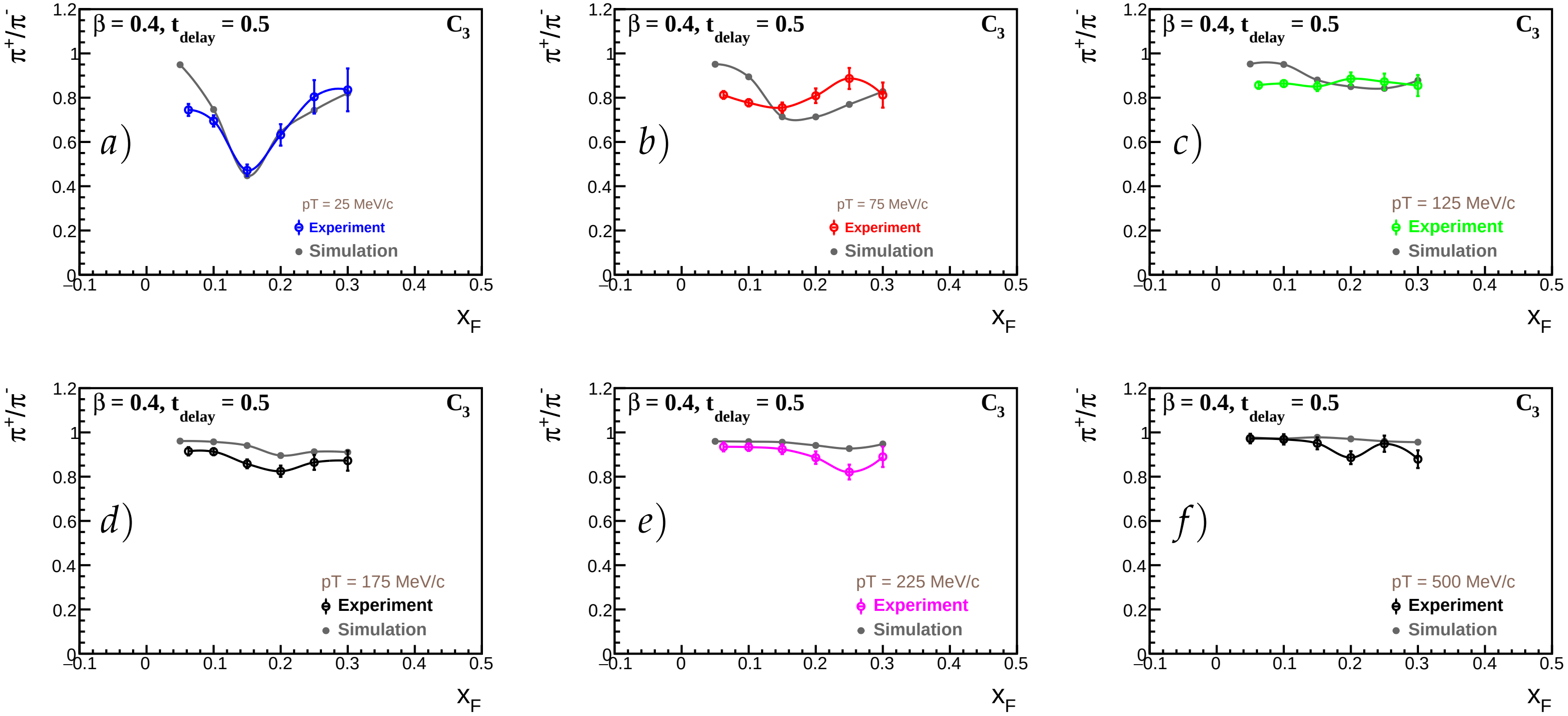

FIGURE 4.10: The Monte Carlo simulation results in π^+/π^- ratio as a function of x_F for the centrality sample C_3. The selected free parameters of the model are indicated in the left upper corner of each panel.

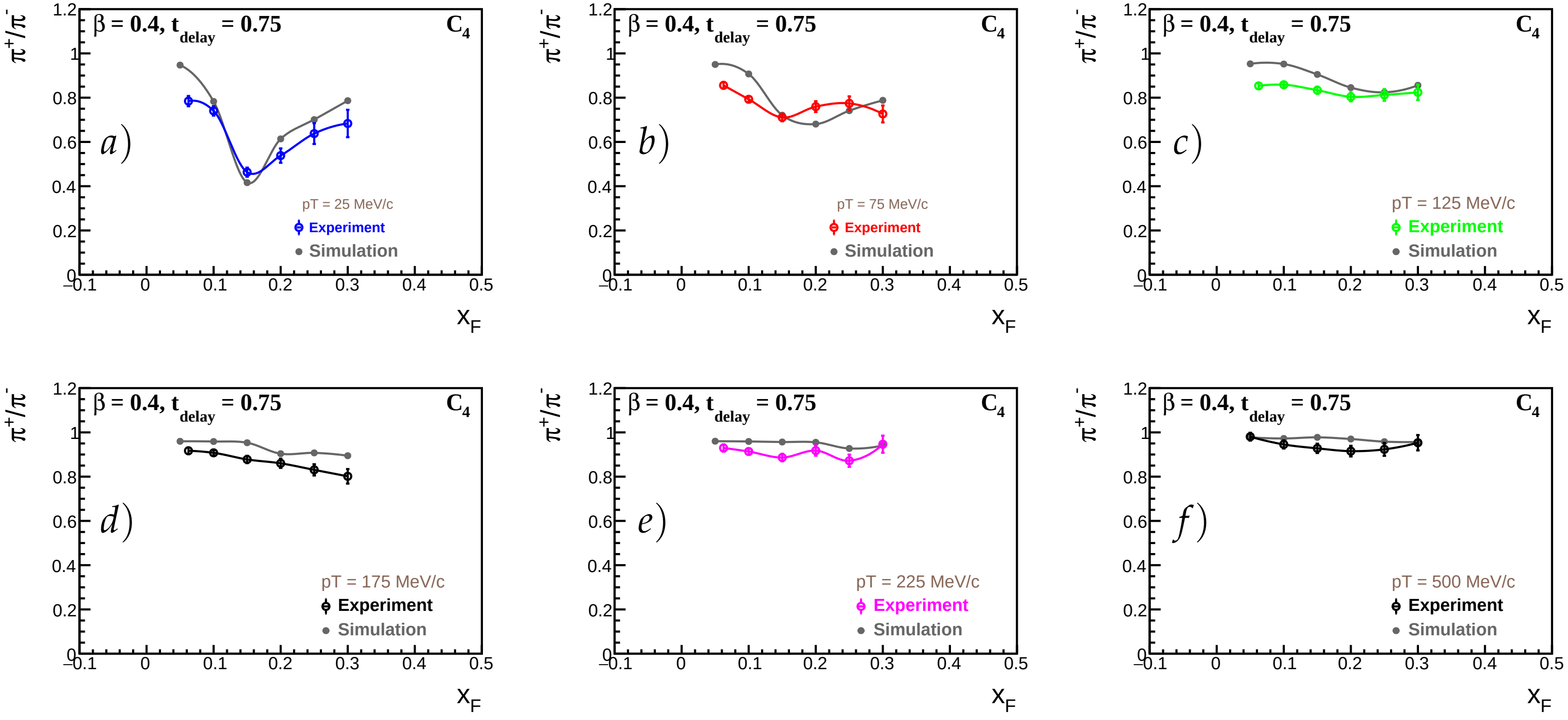

FIGURE 4.11: The Monte Carlo simulation results in π^+/π^- ratio as a function of x_F for the centrality sample C_4. The selected free parameters of the model are indicated in the left upper corner of each panel.

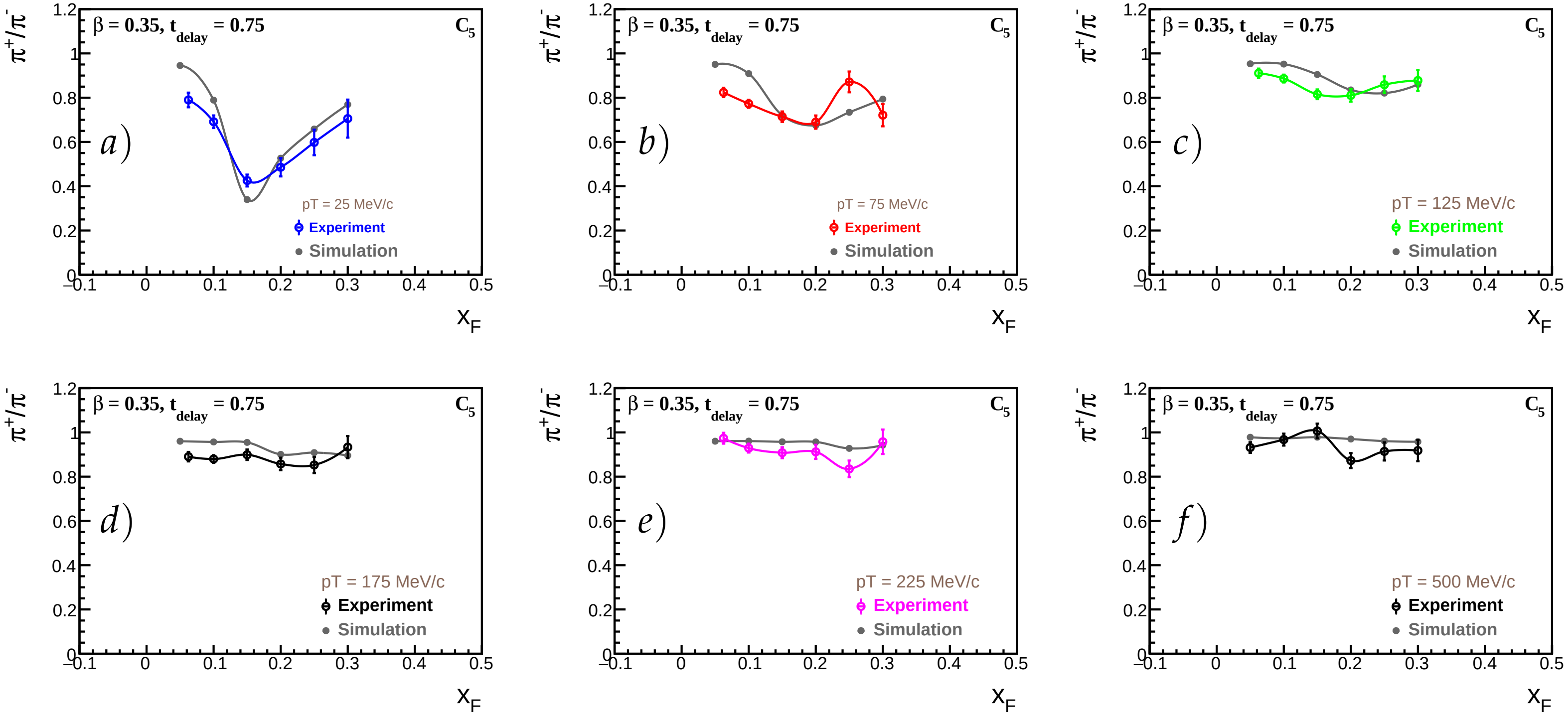

FIGURE 4.12: The Monte Carlo simulation results in π^+/π^- ratio as a function of x_F for the centrality sample C_5. The selected free parameters of the model are indicated in the left upper corner of each panel.

4.3.4 Discussion

Below an additional discussion of the results of the comparison between the experimental data and model simulation made in the previous section is presented.

1. It has been seen that the π^+/π^- ratio in the experimental data at low x_F and p_T is below the π^+/π^- ratio predicted by the model. As already pointed in section 4.2, in this region the experimental data have large errors which suggest caution in formulating conclusions. Still, some role can be attributed to participant charge (the net positive charge of the expanding fireball). This effect was neglected in the original model approach published by A. Rybicki and A. Szczurek [22], while in fact it is known that participant charge affects the p_T-dependence of π^+/π^- ratios in Pb+Pb collisions [74]. This clearly points to the importance of the inclusion of effects induced by participant charge in future phenomenological studies, in particular for the centrality dependence of EM effects at mid-rapidity. However, this phenomenological issue remains beyond the scope of the present work.

2. The discrepancy which is apparent between experimental data and model at higher p_T could be informative on another potentially important aspect of fast pion production, namely isospin effects. Unlike in peripheral heavy ion collisions studied earlier, for final state π^+/π^- ratios in smaller systems, we don't have a clear dominance of the effect induced by the EM interaction between the spectator system and emitted charged pions but rather its concurrence with respect to all other effects. This is in particular valid for isospin effects i.e. the way the isospin (proton/neutron) content of the Ar nucleus reflects in the π^+/π^- ratios, see discussion made in section 4.2. The present conclusion is that the description of isospin effects taken in the model, parameterized on the basis of p+p data and of the wounded nucleon model [5] with the inclusion of isospin ("wounded protons", "wounded neutrons") as it was described in Ref. [76], may be oversimplified with respect to physical reality.

3. The adjusted values of β are large. While the breakup (fragmentation) of the spectator system will definitely result in the expansion of the

corresponding "charge cloud", at the present moment it is not to be excluded that these large values would also in some way be connected to the expansion of the participant system (fireball).

4. Notwithstanding all the weaknesses of the present description of π^+/π^- ratios obtained in this thesis by the model described above, a tentative comparison between the values of d_E estimated for the intermediate and peripheral heavy ion collisions [26] and in the Ar+Sc system has been performed by the author and it is shown in Fig. 4.13. It seems apparent that in spite of all the cited sources of conceptual and experimental uncertainty, a common trend emerges from the comparison, with values of distance d_E decreasing with increasing pion rapidity and being comparable in Ar+Sc and Au+Au or Pb+Pb collisions. This naturally suggests a reasonably similar space-time evolution of pion production in the three reaction types.

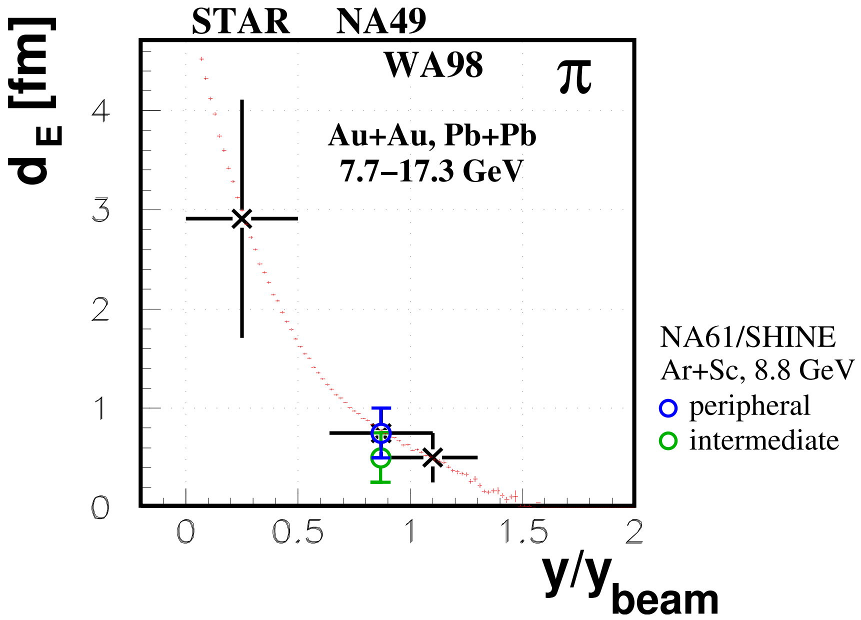

FIGURE 4.13: Distribution of the distance d_E between the pion formation zone and the spectator system as a function of pion rapidity. Figure adapted from Ref. [26]. The black "x" symbols correspond to values estimated on the basis of pion data from STAR [77], NA49 [30] and WA98 [78]. The small red crosses correspond to a Monte Carlo model simulation of pion production by resonances emitted from an intermediate system [26].

4.3.5 Additional remarks

The basic picture which emerges from the comparative study presented in this chapter is that the bulk of the centrality dependence of the spectator-induced EM effect in Ar+Sc reactions is described reasonably well by the simple approach used by the author. The limitations of this approach and the areas of phase space where it does not provide a satisfactory description of the data have been enumerated in the precedent section. The question remains whether a more sophisticated approach like the one published by Ozvenchuk et al. [27] could be used to provide a fully realistic, quantitative description of the Ar+Sc data.

The discussions in the IFJ PAN NA61/SHINE group suggest that the interplay between the different effects present in small systems: the reasonably weak EM effect, isospin effects, and other effects like flow are very difficult to disentangle by a simplified phenomenological apparatus. There is also a conviction that the more sophisticated approach by Ozvenchuk et al. [27] will not be reliably applied to the experimental data in a situation with many concurrent effects like in Ar+Sc collisions. Here the important disadvantage with respect to peripheral Pb+Pb collisions is that in the Ar+Sc reactions, none of these enumerated effects is so clearly dominant. A possible solution is the experimental analysis of another system, with an intermediate position between Ar+Sc and Pb+Pb collisions. The idea is to provide further experimental information to better quantify the evolution of π^+/π^- ratios with decreasing system and spectator size to allow for a data-based development of a more extended phenomenological apparatus on the basis of what is available in Ref. [27]. The plans are made for Xe+La data which is already available from the NA61/SHINE collaboration.

The conclusions from this work will be presented in the next Chapter.

Chapter 5

Summary, conclusions and outlook

This work was an experimental analysis of Ar+Sc collisions at $40A$ GeV/c presented as a function of centrality. Analyses have been performed on two sets of centrality samples (three and six samples, respectively). The measurements were carried out within the NA61/SHINE collaboration, using a high-acceptance hadron spectrometer operating at the CERN SPS.

As it was demonstrated in earlier works, the spectator-induced EM effects are sensitive to the space-time evolution of the non-perturbative process of particle production. Therefore they can be used to study the space-time evolution of the system. For Ar+Sc collisions in the (nearly) full range of centrality, the first attempt at such a study has been made by the author in this thesis. Below a summary, conclusion, and outlook for the present work can be found.

5.1 Summary

The present thesis described experimental results on charged ratios of π^+ and π^- mesons produced in Ar+Sc collisions at $40A$ GeV/c which corresponds to $\sqrt{s_{NN}}$ = 8.76 GeV. For each considered sample of collision centrality the π^+/π^- ratio has been investigated as a function of the Feynman variable x_F and transverse momentum p_T. This is the first-ever analysis of a "small" colliding nucleus-nucleus system in full centrality coverage made in NA61/SHINE. As a summary of this work, the following points can be made:

1. The experimental analysis done in this thesis showed that the spectator-induced EM effects are present in small colliding systems, in spite of the relatively low values of the corresponding spectator charge. A clear

suppression of π^+/π^- ratio close to $x_F = 0.15$ and low p_T (25 MeV/c) is seen.

2. A "trace" of this spectator-induced EM effect was espied even in the central collision (0-19% of the total cross-section). Consequently, a more "granular" analysis was performed in order to get a more precise picture of its centrality dependence. This was performed by dividing each centrality sample into two.

3. The new experimental results on Ar+Sc collisions at $\sqrt{s_{NN}} = 8.76$ GeV have been compared with the existing data on the peripheral Pb+Pb reactions at $\sqrt{s_{NN}} = 17.3$ GeV.

4. To understand the basic characteristics of the obtained results on spectator-induced EM effects, a simulation based on a simple theoretical model was performed. This model was originally developed to understand the EM effect in Pb+Pb reactions. However, the model has been extended with the expansion (fragmentation) of the spectator charge, which in fact appeared necessary for the description of Ar+Sc collisions as a function of centrality.

5.2 Conclusions

Below are the conclusions that can be drawn from this study, in direct correspondence to points 1-4 from section 5.1.

1. The spectator-induced EM effect develops gradually from central to peripheral collisions, following the corresponding increase of spectator charge. The π^+/π^- ratio goes down to about 0.4 which is far below the lower limit estimated if the effect would be induced by the pure strong interaction, with conservation of isospin symmetry as discussed in the section 4.1.

2. Spectator-induced EM effects remain visible for all centrality samples studied, except for the most central collisions. No spectator-induced EM effect was seen in the most central collision sample (0-9.5% of the total Ar+Sc cross-section).

3. From the comparison between Ar+Sc and Pb+Pb collisions, it can be concluded that there is a qualitative similarity in the x_F and p_T dependence of the EM effect. In most peripheral Ar+Sc collisions, the depletion of the π^+/π^- ratio is about half of the effect observed in Pb+Pb collisions.

4. The comparison between experimental data and the theoretical model for the EM effect brings the following conclusions:

    (a) The most basic characteristics of the spectator-induced EM effect including in particular the x_F, p_T, and the centrality dependence are properly described by the model.

    (b) A quantitative discrepancy between model predictions and experimental data at higher p_T suggests that the isospin effects implemented in the model based on p+p collision data could be oversimplified with respect to physical reality.

    (c) The values of radial velocity characterising the fragmentation of the projectile spectator system adjusted to the experimental data are quite large. It is not excluded that such large values of β are in some way connected to the expansion of the participant system.

    (d) Comparison between the model and the experimental data resulted in a set of adjusted values of d_E, which gave an optimal description of experimental results. These values of the distance d_E between the pion formation zone and the spectator system seem to agree with the overall trend obtained for heavy ion collisions on the basis of STAR, WA98 and NA49 data (see Fig. 4.13). This trend corresponds to d_E decreasing with increasing pion rapidity, explained in section 4.3.4.

5.3 Outlook

The scrutiny of the results of the comparison between data and model, performed in this thesis, has brought a relatively complex picture of the detailed characteristics of the spectator-induced EM effect in Ar+Sc collisions. It has been argued that in Pb+Pb collisions, the pure "EM part" of the effect plays a dominant role in the observed distortion (lowering) of the π^+/π^- ratio.

In Ar+Sc collisions, with smaller values of spectator charge, it is expected that one will deal with the concurrence of other effects. A good example of such a concurrent effect would be the influence of isospin proton/neutron content of the colliding nuclei on the π^+/π^- ratio. As such, more in-depth theoretical studies are required.

For a new direction in experimental research, one should also look into the analysis of another system with an intermediate position between Ar+Sc and Pb+Pb collisions. In this context, the Xe+La data collected by NA61-/SHINE which are available for analysis. Therefore interesting results are expected in the near future. The Xe+La collision will be an optimal "bridge" between Ar+Sc and Pb+Pb collisions. We expect that these new experimental data will boost the future phenomenological studies of the space-time evolution of the system as a function of its size, in the presence of EM effects. The next step would be the experimental analysis of very high statistics Pb+Pb data at $\sqrt{s_{NN}}$ = 16.8 GeV, collected by the upgraded NA61/SHINE detector.

As a final comment, the role of the analysis made in this thesis, as well as of future studies of spectator-induced EM effects in the more general context of studies of particle production phenomena should be addressed. Being focused on the ratios of charged pions and their evolution over the available phase space, the present analysis is partially complementary to the analysis of particle spectra in Ar+Sc collisions [6, 7, 44]. The possibility of comparison of the latter pion ratios between Ar+Sc and Pb+Pb collisions can be regarded as another aspect of the study of system-size dependence of particle production, which is one of the main scientific programs of the NA61/SHINE collaboration [79]. On the other hand, it is expected that the present first analysis of Ar+Sc reactions in nearly full centrality range in NA61/SHINE will provide useful experimental insight for future analyses of this type.

However, what the author finds most interesting is the potential complementarity of studies of EM effects with HBT interferometry (femtoscopy). The analysis of spectator-induced EM effects provides information about the spatial and temporal evolution of the process of particle production. On the other hand, HBT interferometry provides insight into the size and lifetime of the system created in the collision. In this way, the two methods of analysis provide complementary information. As both methods are sensitive to somewhat different space-time aspects of the same system, the author expects that combining the insights from both can lead to a more comprehensive space-time picture of the complex processes taking place in the nucleus-nucleus reaction.

Bibliography

[1] S. Weinberg. “The making of the Standard Model”. In: *The European Physical Journal C* 34 (2004), pp. 5–13. DOI: `10.1140/epjc/s2004-01761-1`.

[2] M. Kuich. “Kaon production in mid-rapidity in Be+Be collisions at the CERN SPS.” PhD thesis, Warsaw University, 2019. URL: `https://cds.cern.ch/record/2674258`.

[3] S. Chatrchyan et al. “Observation of a New Boson at a Mass of 125 GeV with the CMS Experiment at the LHC”. In: *Phys. Lett. B* 716 (2012), pp. 30–61. arXiv: `1207.7235 [hep-ex]`.

[4] G. Aad et al. “Observation of a new particle in the search for the Standard Model Higgs boson with the ATLAS detector at the LHC”. In: *Physics Letters B* 716 (2012), pp. 1–29. DOI: `https://doi.org/10.1016/j.physletb.2012.08.020`.

[5] A. Białas, M. Bleszyński, and W. Czyż. “Multiplicity Distributions in Nucleus-Nucleus Collisions at High-Energies”. In: *Nucl. Phys. B* 111 (1976), pp. 461–476. DOI: `10.1016/0550-3213(76)90329-1`.

[6] M. Lewicki. “Charged hadron production in central Ar+Sc collisions at the CERN SPS.” PhD thesis, Wrocław University, 2022. URL: `https://cds.cern.ch/record/2772291`.

[7] P. Podlaski. “Study of charged hadron production with tof-dE/dx identification method in central Ar+Sc collisions in NA61/SHINE experiment at CERN.” PhD thesis, Warsaw University, 2022. URL: `https://cds.cern.ch/record/2799198`.

[8] Mattia. *Particles and friends*. WordPress, 2016. URL: `https://particles%5C-andfriends.wordpress.com/2016/10/14/evolution-of-collisions-and-qgp`.

[9] E. Andronov, M. Kuich, and M. Gaździcki. “Diagram of High-Energy Nuclear Collisions”. In: *Universe* 9 (2023), p. 106. arXiv: `2205.06726 [hep-ph]`.

[10] S. V. Afanasiev et al. “Energy dependence of pion and kaon production in central Pb+Pb collisions”. In: *Phys. Rev. C* 66 (2002), p. 054902.

[11] M. Gazdzicki and A. Rybicki for the NA61/SHINE Collaboration. “Overview of Results from NA61/ SHINE : Uncovering Critical Structures”. In: *Acta Phys. Polon. B* 50 (2019), pp. 1057–1070. DOI: `10.5506/APhysPolB.50.1057`.

[12] M. Gazdzicki and M. I. Gorenstein. “On the Early Stage of Nucleus–Nucleus Collisions”. In: *Acta Phys. Polon. B* 30 (1998), p. 2705. arXiv: `hep-ph/9803462 [hep-ph]`.

[13] H. Satz. “Deconfinement and percolation”. In: *Nuclear Physics A* 642 (1998), pp. c130–c142. DOI: `https://doi.org/10.1016/S0375-9474(98)00508-9`.

[14] J. E. Ramırez and C. Pajares. “Area covered by disks in small-bounded continuum percolating systems: An application to the string percolation model”. In: *Phys. Rev. E* 100 (2019), p. 022123. DOI: `10.1103/PhysRevE.100.022123`.

[15] M. Gazdzicki and P. Seyboth. “Search for Critical Behaviour of Strongly Interacting Matter at the CERN Super Proton Synchrotron”. In: *Acta Physica Polonica B* 47 (2016), p. 1201. DOI: `10.5506/aphyspolb.47.1201`.

[16] N. Davis for the NA61/SHINE Collaboration. “Searching for the Critical Point of Strongly Interacting Matter in Nucleus–Nucleus Collisions at CERN SPS”. In: *Acta Phys. Polon. Supp.* 13 (2020), pp. 637–643. arXiv: `2002.06636 [nucl-ex]`.

[17] H. Adhikary et al. “Search for the critical point of strongly-interacting matter in ^{40}Ar + ^{45}Sc collisions at 150A GeV/c using scaled factorial moments of protons”. In: *submitted for publication by the NA61/SHINE Collaboration* (2023). arXiv: `2305.07557 [nucl-ex]`.

[18] N. Davis. “Intermittency analysis in heavy ion collisions: a review of the current status and challenges.” In: *PoS* CORFU2021 (2022), p. 005. DOI: `10.22323/1.406.0005`.

[19] M. Gazdzicki, M. Gorenstein, and P. Seyboth. "Onset of Deconfinement in Nucleus–Nucleus Collisions: Review for Pedestrians and Experts". In: *Acta Physica Polonica B* 42 (2011), p. 307. DOI: `10.5506/aphyspolb.42.307`.

[20] N. Abgrall et al. *NA61/SHINE plans beyond the approved program*. Tech. rep. CERN, 2012. URL: `https://cds.cern.ch/record/1463552`.

[21] A. Rybicki, A. Szczurek, and E. Kozik. "The spectator-induced electromagnetic effect on kaon production in heavy ion collisions". In: *Acta Phys. Polon. Supp.* 5 (2012), pp. 369–374. DOI: `10.5506/APhysPolBSupp.5.369`.

[22] A. Rybicki and A. Szczurek. "The Spectator Electromagnetic Effect on Charged Pion Spectra in Peripheral Ultrarelativistic Heavy-Ion Collisions". In: *Phys. Rev. C* 75 (2007), p. 054903. DOI: `10.1103/PhysRevC.75.054903`. arXiv: `nucl-th/0610036`.

[23] M. Kiełbowicz for the NA61/SHINE collaboration. "Electromagnetic effect on charged pion spectra at SPS energies". In: *Acta Phys. Polon. Supp.* 12 (2019), p. 353. DOI: `10.5506/APhysPolBSupp.12.353`.

[24] A. Marcinek for the NA61/SHINE collaboration. "Highlights from the NA61/SHINE Experiment". In: *Acta Phys. Polon. Supp.* 16 (2023), p. 8. arXiv: `2208.13823 [nucl-ex]`.

[25] S. Bhosale for the NA61/SHINE collaboration. "Spectator induced electromagnetic effects on charged meson production in nucleus-nucleus collisions from NA61/SHINE at CERN SPS". In: *PoS* EPS-HEP2021 (2022), p. 309. DOI: `10.22323/1.398.0309`.

[26] A. Rybicki et al. "Can we obtain a "new femtoscopy" on the basis of electromagnetic effects?" In: *Acta Phys. Polon. Supp.* 9 (2016), p. 303. arXiv: `1603.07558 [nucl-th]`.

[27] V. Ozvenchuk et al. "Spectator induced electromagnetic effects in heavy-ion collisions and space-time-momentum conditions for pion emission". In: *Phys. Rev. C* 102 (2020), p. 014901. arXiv: `1910.04544 [nucl-th]`.

[28] V. Ozvenchuk, A. Szczurek, and A. Rybicki. "Fire streaks, electromagnetic effects, directed flow and lifetime of the plasma at SPS energies". In: *PoS* ICHEP2020 (2021), p. 558. arXiv: `2012.06243 [nucl-th]`.

[29] A. Rybicki. "Strong and Electromagnetic Effects in Peripheral Nucleus-nucleus Collisions at SPS Energies". Habilitation thesis, IFJ PAN Report no. 2040/PH. Kraków, 2010. URL: `https://www.ifj.edu.pl/badania/publikacje/raporty/2010/2040.pdf`.

[30] A. Rybicki. "Strong and electromagnetic interactions at SPS energies". In: *PoS* EPS-HEP2009 (2009), p. 031. DOI: `10.22323/1.084.0031`.

[31] A. Szczurek, M. Kiełbowicz, and A. Rybicki. "Implications of energy and momentum conservation for particle emission in A+A collisions at energies available at the CERN Super Proton Synchrotron". In: *Phys. Rev.* C95 (2017), p. 024908. arXiv: `1612.06694 [nucl-th]`.

[32] A. Rybicki et al. "Rapidity distributions of pions in p+p and Pb+Pb collisions at energies available at the CERN Super Proton Synchrotron". In: *Phys. Rev. C* 99 (2019), p. 024908. arXiv: `1805.02552 [nucl-th]`.

[33] R. Hagedorn. *Thermodynamics of strong interactions*. CERN Academic Training Lecture. CERN, 1971. DOI: `10.5170/CERN-1971-012`.

[34] W. D. Myers. "A model for high-energy heavy-ion collisions". In: *Nuclear Physics A* 296 (1978), pp. 177–188. DOI: `https://doi.org/10.1016/0375-9474(78)90420-7`.

[35] J. Gosset, J. I. Kapusta, and G. D. Westfall. "Calculations with the nuclear firestreak model". In: *Phys. Rev. C* 18 (1978), pp. 844–855. DOI: `10.1103/PhysRevC.18.844`.

[36] V. K. Magas, L. P. Csernai, and D. D. Strottman. "Initial state of ultra-relativistic heavy ion collisions". In: *Phys. Rev. C* 64 (2001), p. 014901. DOI: `10.1103/PhysRevC.64.014901`.

[37] V. K. Magas, L. P. Csernai, and D. Strottman. "Effective string rope model for the initial stages of ultra-relativistic heavy ion collisions". In: *Nuclear Physics A* 712 (2002), pp. 167–204. DOI: `https://doi.org/10.1016/S0375-9474(02)01073-4`.

[38] I. N. Mishustin and J. I. Kapusta. "Collective Deceleration of Ultrarelativistic Nuclei and Creation of Quark-Gluon Plasma". In: *Phys. Rev. Lett.* 88 (2002), p. 112501. DOI: `10.1103/PhysRevLett.88.112501`.

[39] A. Marcinek for the NA61/SHINE Collaboration. "Strong and Electromagnetic Collective Effects from NA61/SHINE". In: *Acta Phys. Polon. B* 50 (2019), pp. 1127–1137.

[40] A. Szczurek, A. Rybicki, and A. Z. Gorski. “The Effect of the spectator charge on the charged pion spectra in peripheral ultrarelativistic heavy-ion collisions”. In: *J. Phys. G* 34 (2007), S827–830. arXiv: `nucl-th/0701056`.

[41] A. Rybicki. “What Is the role of nuclear effects in ultrarelativistic reactions at 158-GeV/nucleon?” In: *Acta Phys. Polon. B* 42 (2011), pp. 867–876. DOI: `10.5506/APhysPolB.42.867`.

[42] N. Abgrall et al. “NA61/SHINE facility at the CERN SPS: beams and detector system”. In: *JINST* 9 (2014), P06005. arXiv: `1401.4699 [physics.ins-det]`.

[43] A. Aduszkiewicz. “Energy dependence of negatively charged pion production in proton-proton interactions at the CERN SPS”. PhD thesis, Warsaw University, 2016. URL: `https://cds.cern.ch/record/2135329`.

[44] A. Acharya et al. “Spectra and mean multiplicities of π^- in central ^{40}Ar+^{45}Sc collisions at 13A, 19A, 30A, 40A, 75A and 150A GeV/c beam momenta measured by the NA61/SHINE spectrometer at the CERN SPS”. In: *Eur. Phys. J. C* 81 (2021), p. 397. arXiv: `2101.08494 [hep-ex]`.

[45] A. Rybicki and A. D. Marino for the NA61/SHINE Collaboration. *Report from the NA61/SHINE experiment at the CERN SPS*. Tech. rep. CERN-SPSC-2022-034, SPSC-SR-319. CERN, 2022. URL: `https://cds.cern.ch/record/2839856`.

[46] R. Scrivens et al. *Overview of the status and developments on primary ion sources at CERN*. Tech. rep. CERN-ATS-2011-172. 2011. URL: `https://cds.cern.ch/record/1382102`.

[47] M. Weiss. “The RFQ2 complex: The future injector to CERN Linac 2”. In: *Conf. Proc. C* 920324 (1992), pp. 539–541.

[48] D. Banas et al. *Influence of target material impurities on physical results in relativistic heavy-ion collisions*. 2018. DOI: `10.48550/ARXIV.1808.10377`.

[49] G. Charpak and F. Sauli. “Multiwire proportional chambers and drift chambers”. In: *Nuclear Instruments and Methods* 162 (1979), pp. 405–428. DOI: `https://doi.org/10.1016/0029-554X(79)90726-2`.

[50] P. A. Zyla et al. (Particle Data Group). In: *Prog. Theor. Exp. Phys.* 2020, 083C01 (2020). DOI: `10.1093/ptep/ptaa104`.

[51] B. Baatar et al. “Inclusive production of protons, anti-protons, neutrons, deuterons and tritons in p+C collisions at 158 GeV/c beam momentum”. In: *Eur. Phys. J. C* 73 (2013), p. 2364. arXiv: `1207.6520 [hep-ex]`.

[52] T. Anticic et al. “Inclusive production of charged kaons in p+p collisions at 158 GeV/c beam momentum and a new evaluation of the energy dependence of kaon production up to collider energies”. In: *Eur. Phys. J. C* 68 (2010), pp. 1–73. arXiv: `1004.1889 [hep-ex]`.

[53] C. Alt et al. “Inclusive production of charged pions in p+C collisions at 158-GeV/c beam momentum”. In: *Eur. Phys. J. C* 49 (2007), pp. 897–917. arXiv: `hep-ex/0606028`.

[54] C. Alt et al. “Inclusive production of charged pions in p+p collisions at 158-GeV/c beam momentum”. In: *Eur. Phys. J. C* 45 (2006), pp. 343–381. arXiv: `hep-ex/0510009`.

[55] A. Rybicki. “Charged hadron production in elementary and nuclear collisions at 158-GeV/c”. PhD thesis. Inst. of Nucl. Phys., Kraków, 2002. CERN-THESIS-2003-005.

[56] K. Grebieszkow. “Lecture on introduction to heavy ion collisions”. 2019/2020. URL: `http://www.if.pw.edu.pl/~kperl/HIP/hip.html`.

[57] A. Seryakov for the NA61/SHINE collaboration. “Rapid change of multiplicity fluctuations in system size dependence at SPS energies”. Talk at Zimanyi-COST workshop, 2017. URL: `https://indico.cern.ch/event/684046/contributions/2809622`.

[58] M. Maćkowiak-Pawłowska. Private communication.

[59] O. Chvala for the NA49 collaboration. “Pion production in Pb Pb collisions at the SPS”. In: *Nucl. Phys. A* 749 (2005), pp. 304–308. DOI: `10.1016/j.nuclphysa.2004.12.057`.

[60] A. Rybicki et al. “Electromagnetic effects on meson production: a new tool for studying the space-time evolution of heavy ion collisions”. In: *EPJ Web Conf.* 130 (2016), p. 05016. arXiv: `1607.00413 [nucl-th]`.

[61] T. Anticic et al. “System-size and centrality dependence of charged kaon and pion production in nucleus-nucleus collisions at 40A GeV and 158A GeV beam energy”. In: *Physical Review C* 86 (2012). DOI: `10.1103/physrevc.86.054903`.

[62] A. Marcinek. Private communication.

[63] K. Werner, F. M. Liu, and T. Pierog. "Parton ladder splitting and the rapidity dependence of transverse momentum spectra in deuteron-gold collisions at RHIC". In: *Phys. Rev. C* 74 (2006), p. 044902. arXiv: `hep-ph/0506232`.

[64] T. Pierog and K. Werner. "EPOS Model and Ultra High Energy Cosmic Rays". In: *Nucl. Phys. B Proc. Suppl.* 196 (2009), pp. 102–105. arXiv: `0905.1198 [hep-ph]`.

[65] T. Pierog. Private communication, 2018.

[66] S. Agostinelli et al. "Geant4-a simulation toolkit". In: *Nuclear Instruments and Methods in Physics Research Section A: Accelerators, Spectrometers, Detectors and Associated Equipment* 506 (2003), pp. 250–303. DOI: `https://doi.org/10.1016/S0168-9002(03)01368-8`.

[67] M. Naskręt. "Energy dependence of negatively charged pion production in nucleus-nucleus collisions". PhD thesis, Wrocław University, July 2021. URL: `https://cds.cern.ch/record/2840685`.

[68] M. Kiełbowicz. "Electromagnetic effects in Ar+Sc". NA61/SHINE collaboration meeting, Feb 2018. URL: `https://indico.cern.ch/event/674625/contributions/2989335`.

[69] R. Brun et al. *GEANT 3: user's guide Geant 3.10, Geant 3.11; rev. version*. CERN, 1987. URL: `https://cds.cern.ch/record/1119728`.

[70] W. Brylinski for the NA61/SHINE Collaboration. "Strangeness production in NA61/SHINE". The 38th edition of the Winter Workshop on Nuclear Dynamics, Mexico. Feb, 2023. URL: `https://indico.cern.ch/event/1196342/contributions/5228282`.

[71] A. Rybicki and A. Szczurek. "Spectator induced electromagnetic effect on directed flow in heavy ion collisions". In: *Phys. Rev. C* 87 (2013), p. 054909. arXiv: `1303.7354 [nucl-th]`.

[72] O. Chvala for the NA49 collaboration. "On the Importance of Isospin Effects for the Interpretation of Nuclear Collisions". In: *Eur. Phys. J. C* 33 (2004), s615–s617. URL: `https://cds.cern.ch/record/735881`.

[73] G. Barr et al. "Charged Pion Production in p+C Collisions at 158-GeV/c Beam Momentum: Discussion". In: *Eur. Phys. J. C* 49 (2007), pp. 919–945. arXiv: `hep-ex/0606029`.

[74] Nu Xu for the NA44 Collaboration. “Hadron distributions — Recent results from the CERN experiment NA44”. In: *Nuclear Physics A* 610 (1996), pp. 175–187. DOI: `https://doi.org/10.1016/S0375-9474(96)00353-3`.

[75] S. Puławski for the NA61/SHINE Collaboration. “Recent results from the strong interactions program of NA61/SHINE”. In: *EPJ Web Conf.* 164 (2017), p. 07033. arXiv: `1705.02462 [nucl-ex]`.

[76] Ł. Rozpłochowski. “Simulating the double differential density distribution for Pb+Pb reaction at $\sqrt{s_{NN}}$ = 8.8 GeV and 17.3 GeV”. IFJ PAN NZ23 seminar, Jun 25, 2021. URL: `https://indico.ifj.edu.pl/event/1099`.

[77] L. Adamczyk et al. “Beam-Energy Dependence of the Directed Flow of Protons, Antiprotons, and Pions in Au+Au Collisions”. In: *Phys. Rev. Lett.* 112 (2014), p. 162301. arXiv: `1401.3043 [nucl-ex]`.

[78] H. Schlagheck. “Thermalization and flow in 158-GeV/A Pb + Pb collisions”. In: *Nucl. Phys. A* 663 (2000), pp. 725–728. arXiv: `nucl-ex/9909005`.

[79] M. Maćkowiak-Pawłowska for the NA61/SHINE Collaboration. “Recent results from NA61/SHINE”. In: *Acta Phys. Polon. Supp.* 10 (2017), pp. 1183–1189. arXiv: `1707.04735 [nucl-ex]`.